DISSERTATIONES
SCIENTIAE
MATERIALIS
UNIVERSITATIS
TARTUENSIS
27

JEKATERINA KOZLOVA

Complex characterization of graphene structures on nanometer level

DISSERTATIONES SCIENTIAE MATERIALIS UNIVERSITATIS TARTUENSIS
27

DISSERTATIONES SCIENTIAE MATERIALIS UNIVERSITATIS TARTUENSIS
27

JEKATERINA KOZLOVA

Complex characterization of graphene structures on nanometer level

UNIVERSITY OF TARTU
Press

The study was carried out in Department of Material Science, Institute of Physics, Faculty of Science and Technology, University of Tartu, Estonia

The Dissertation was admitted on November 04, 2019 in partial fulfillment of the requirements for the degree of Doctor of Philosophy in Material Science and allowed for defense by Scientific Council on Material Science of the Faculty of Science and Technology, University of Tartu.

Supervisors: Prof. Väino Sammelselg, Institute of Physics, Institute of Chemistry, University of Tartu, Tartu, Estonia

Dr. Harry Alles, Institute of Physics, University of Tartu, Tartu, Estonia

Opponent: Prof. Alexander N. Obraztsov, Department of Physics, M.V. Lomonosov Moscow State University, Moscow, Russia and Department of Physics and Mathematics, University of Eastern Finland, Joensuu, Finland

Commencement: December 13, 2019 at the University of Tartu, Tartu, Estonia

This thesis was supported by the Graduate School of Doctorial Studies in Estonia: "Functional materials and technologies" (project 1.2.0401.09-0079), by the European Union through the European Social Fund (Grant MTT1) and FP7 program under Grant Agreement No. 604391 Graphene Flagship and by the Estonian Ministry of Education and Research (Projects IUT2-24, TK117 and TK141).

ISSN 2228-0928
ISBN 978-9949-03-226-6 (Hard copy)
ISBN 978-9949-03-227-3 (PDF)

University of Tartu Press
www.tyk.ee

TABLE OF CONTENTS

LIST OF ORIGINAL PUBLICATIONS

The thesis is based on the following papers:

I. **J. Kozlova**, A. Niilisk, H. Alles, V. Sammelselg, Discontinuity and misorientation of graphene grown on nickel foil: Effect of the substrate crystallographic orientation. *Carbon* 94 (2015) 160–173.

II. A. Niilisk, **J. Kozlova**, H. Alles, J. Aarik, V. Sammelselg, Raman characterization of stacking in multi-layer graphene grown on Ni. *Carbon* 98 (2016) 658–665.

III. E. Kibena, M. Mooste, **J. Kozlova**, M. Marandi, V. Sammelselg, K. Tammeveski, Surface and electrochemical characterization of CVD grown graphene sheets. *Electrochemistry Communications* 35 (2013) 26–29.

IV. M. Mooste, E. Kibena, **J. Kozlova**, M. Marandi, L. Matisen, A. Niilisk, V. Sammelselg, K. Tammeveski, Electrografting and morphological studies of chemical vapour deposition grown graphene sheets modified by electroreduction of aryldiazonium salts. *Electrochimica Acta* 161 (2015) 195–204.

V. H. Alles, J. Aarik, A. Aidla, A. Fay, **J. Kozlova**, A. Niilisk, M. Pärs, M. Rähn, M. Wiesner, P. Hakonen, V. Sammelselg, Atomic layer deposition of HfO_2 on graphene from $HfCl_4$ and H_2O. *Central European Journal of Physics* 9(2) (2011) 319–324.

VI. A. Tamm, **J. Kozlova**, L. Aarik, A. Aidla, J. Lu, A.A. Kiisler, A. Kasikov, P. Ritslaid, H. Mändar, L. Hultman, V. Sammelselg, K. Kukli, J. Aarik, Atomic layer deposition of ZrO_2 for graphene-based multilayer structures: In situ and ex situ characterization of growth process. *Physica Status Solidi A*, 211 (2014) 397–402.

AUTHOR'S CONTRIBUTION

The author's contribution to each paper is given below.

I. The author was responsible for the synthesis of graphene samples by CVD method. The author conducted SEM, EDX, EBSD, Raman (together with Ahti Niilisk) and AFM measurements. The author prepared samples for EBSD measurements using SEM-FIB and performed the graphene transfer. The author has also done the treatment of the graphene samples with argon plasma. The author was responsible for the analysis of the results and writing the paper.

II. The author was responsible for the synthesis of graphene samples by CVD method. The author participated in Raman measurements and analysis of the results.

III. The author was responsible for graphene synthesis. The author conducted Raman (with Ahti Niilisk) and SEM measurements. The author participated in analysis of the results and writing the paper.

IV. The author was responsible for graphene synthesis. The author conducted Raman measurements (with Ahti Niilisk). The author participated in XPS measurements, analysis of the results and writing the paper.

V. The author was responsible for AFM measurements. The author participated in the preparation of the samples by micromechanical exfoliation, Raman measurements, in the analysis of the results and writing the paper.

VI. The author was responsible for graphene synthesis, graphene transfers on mass sensor and SEM measurements and participated in the analysis of the results and writing the paper.

AUTHOR'S OTHER PUBLICATIONS RELATED TO THE TOPIC

A. H. Alles, J. Aarik, J. Kozlova, A. Niilisk, R. Rammula, V. Sammelselg, Atomic layer deposition of high-k oxides on graphene. In: Graphene – Synthesis, Characterization, Properties and Applications. Jian Ru Gong (Ed.). InTech Publishing: 2011. P. 99–114.

B. K-K. Türk, I. Kruusenberg, J. Mondal, P. Rauwel, J. Kozlova, L. Matisen, V. Sammelselg, K. Tammeveski, Oxygen electroreduction on MN_4 macrocycle modified graphene/multi-walled carbon nanotube composites, *J. Electroanal. Chem,* 756 (2015) 69–76; DOI: 10.1016/j.jelechem.2015.08.014).

LIST OF ABBREVIATIONS

2D	Two-dimensional
ADF	Annular dark field
AFM	Atomic force microscope/microscopy
ALD	Atomic layer deposition
AP	Atmospheric pressure
BF	Bright field
BSE	Backscattered electrons
BLG	Bilayer graphene
CB	Carbon black
CCD	Charge-coupled device
CNTs	Carbon nanotubes
CV	Cyclic Voltammetry
CVD	Chemical vapor deposition
DF	Dark field
DFAFC	Direct formic acid fuel cells
DMFCs	Direct methanol fuel cells
DNA	Deoxyribonucleic acid
EBSD	Electron backscatter diffraction
EDLCs	Electrochemical double-layer capacitors
EDX	Energy dispersive X-ray spectrometer/spectroscopy
EELS	Electron energy loss spectroscopy
EPMA	Electron probe microanalysis
FET	Field effect transistor
FFT	Fast Fourier transform
FIB-SEM	Focused ion beam – scanning electron microscopy/microscope
FLG	Few-layer graphene
FWHM	Full width at half maximum
GC	Glassy carbon
HAADF	High angle annular dark field
HR-SEM	High-resolution scanning electron microscopy/microscope
HRTEM	High-resolution transmission electron microscopy/microscope
HOPG	Highly oriented pyrolytic graphite
LBMs	Layer breathing modes
LIBs	Lithium-ion batteries
LP	Low pressure
LSV	Linear sweep voltammetry
MLG	Multilayer graphene
NC-AFM	Non-contact atomic force microscopy
ND	Normal direction
NIR	Near-infrared
ORR	Oxygen reduction reaction
PDMS	Polydimethylsiloxane

PEMFCs	Proton exchange membrane fuel cells
PMMA	Polymethylmethacrylate
QCM	Quartz crystal microbalance
rGO	Reduced graphene oxide
RMS	Root mean square
SAED	Selected area electron diffraction
SDS	Sodium dodecyl sulfate
SE	Secondary electrons
SEM	Scanning electron microscopy/microscope
SLG	Single-layer graphene
STEM	Scanning transmission electron microscopy/microscope
STM	Scanning tunneling microscopy/microscope
SWCNT	Single-walled carbon nanotubes
TEM	Transmission electron microscopy/microscope
TMA	Trimethylaluminium
UHP	Ultra-high purity
UHV	Ultra-high vacuum
UV	Ultraviolet
Vis	Visible
XPS	X-ray photoelectron spectroscopy

1. INTRODUCTION

The outstanding properties of graphene lead to exceptional interest in its implementation in a wide range of applications. For industrial use, however, a consistent method for large-scale synthesis of high-quality graphene is demanded. Chemical vapor deposition (CVD) on transition metal surfaces is a valuable method for the synthesis of large-area high-quality graphene. In terms of mass production, copper and nickel catalysts are of most interest because of their low cost, availability and relative ease of etching, which allows transferring graphene after synthesis to the arbitrary substrate. Copper is usually a catalyst of choice for single-layer graphene (SLG) synthesis, whereas, on nickel due to higher carbon solubility, few-layer graphene (FLG) or multilayer graphene (MLG) is usually obtained. Alongside the SLG, the FLG and MLG have also shown potential as transparent conductive electrodes [1–6], thermal interface material [7], friction- and wear-reducing coating [7,8] as well as in sensing applications [9–16], spintronics [17–19], etc. In addition, in contrast to SLG, graphene structures with more layers allow for the creation of hybrid intercalation materials with new appealing properties [20].

The FLG and MLG have received even larger interest after it has been shown that the electronic properties of bilayer graphene (BLG) where the layers are twisted with respect to each other to large angles were indistinguishable of the electronic properties of SLG [21]. It was also predicted, that this SLG-behavior will not be constrained to only misoriented bilayer graphene systems, but will be preserved for graphene samples with a larger number of layers in case of their turbostratic arrangement [22]. Indeed, the SLG-traits have been experimentally observed in epitaxial MLG on silicon carbide [23], showing a potential of implementation of thicker graphene samples in graphene-based electronics. In contrast to SLG, FLG and MLG could be less sensitive to external factors, such as adsorbates and substrate. However, in contrast to SLG, there are significantly fewer works discussing the synthesis of the FLG and MLG. In particular, the stacking order of graphene layers in the obtained samples has received little attention until very recently. It is not completely clear, when and to which extent the rotational disorder can be present in the samples and which factors contribute to its appearance. It is also essential to investigate the homogeneity of the obtained graphene sheets.

After graphene synthesis, the further modification of its surface is often necessary to broaden up the utility of graphene or to enhance the performance of graphene-based devices. Graphene, incl. FLG and MLG, functionalized with nanoparticles or organic functional groups, is a promising material for electrochemical applications in advanced energetics [24–26]. One of the strategies to attach organic groups to the surface of graphitic materials is the electrochemical reduction of the aryldiazonium salts. Despite certain progress in this area [27], more studies are required for better understanding and control over the functionalization process of graphene. It is important to conduct the modification procedure directly on

nickel, to exclude the impact of the transfer procedure on the functionalization outcome. Before functionalization, it was required to evaluate the electrochemical properties of as-synthesized MLG on nickel electrodes. In principle, graphene might show electrochemical behavior similar to HOPG. However, there are reports [28][29] showing that graphene electrodes present faster electron transfer kinetics compared to the basal plane of HOPG. However, the improved electrochemical performance can be due to the presence of carbonation debris [30] or the graphene suspension stabilizing surfactants [31] as well as iron contamination [32]. Furthermore, graphene prepared by different methods has highly varied densities of edge plane defects [33]. Considering that at least in case of graphite, the edge sites are the primary source of the electrochemical activity [34], it is apparent that the graphene preparation method influences its electrochemical behavior. Therefore, it is important to measure the electrochemical properties of the synthesized MLG sheets.

The exceptionally high charge carrier mobility of graphene makes the development of graphene-based electronics especially attractive. The graphene field-effect transistors require a top gate, which should be uniform, ultrathin and have high dielectric constant. Atomic layer deposition (ALD) is a method that allows controlling the thickness of the deposition of the film with atomic precision [35]. For the initiation of the oxide growth by ALD, the functionalization of the graphene surface is often employed [36–38]. However, functionalization can have an adverse effect on the transport properties of graphene. Therefore, it would be preferred to obtain a thin high-k dielectric film directly on pristine graphene. Since the deposition of the high-k oxides, such as hafnium dioxide and zirconium dioxide, has been well established in the Laboratory of Thin Film Technology of the University of Tartu, the feasibility of ALD for producing thin continuous high-k oxide films on pristine graphene has been explored.

On the other hand, due to atomic thickness, graphene's investigation is rather challenging, and the combination of different characterization methods is often needed to get a more profound understanding of the graphene growth process as well as the impact of further modification procedures on graphene properties.

In this Thesis, pristine and functionalized few- and multilayer graphene-based structures were prepared and characterized using various spectroscopy (EDX, EBSD, XPS, μRaman) and high-resolution microscopy (HR-SEM and FIB, HR-TEM, STM) methods. First, the FLG and MLG have been synthesized by CVD on Ni catalyst, and the properties of the prepared graphene sheets have been compared to the SLG obtained by CVD or micromechanical exfoliation of natural graphite [I–II, V–VI]. In addition, the electrochemical properties of the synthesized MLG sheets on nickel have been studied, and the possibility of their subsequent functionalization using electroreduction of various diazonium salts has been examined [III–IV]. Finally, the feasibility of the chloride-water ALD of gate dielectric on top of non-functionalized graphene has been explored [V–VI].

2. LITERATURE OVERVIEW

2.1. Structure and properties of graphene

Graphene is a monolayer of carbon atoms forming a two-dimensional (2D) hexagonal lattice. Graphene can be viewed as an individual atomic plane isolated from graphite [39]. It also can be described as a large number of interconnected benzene molecules, with the hydrogen removed and one electron per atom delocalized over the whole crystal [40]. Graphene is the basis of all graphitic materials (Figure 1). The fullerenes belong to point-like (0D) structures and might be viewed as a graphene sheet distorted to fit onto a spherical surface [40]. The carbon nanotubes belong to one-dimensional (1D) structures and are essentially rolled-up graphene, where the bending axis determines the chirality of the nanotube. Graphite is a three-dimensional (3D) material and is a stack of graphene layers in the z-axis with van der Waals bonds. Besides fullerenes, nanotubes, and graphene other recently discovered forms of other sp^2-bonded carbon, like carbon onions, can also be regarded as a modification of graphene with the introduction of curvature, structural defects and dangling bonds [41].

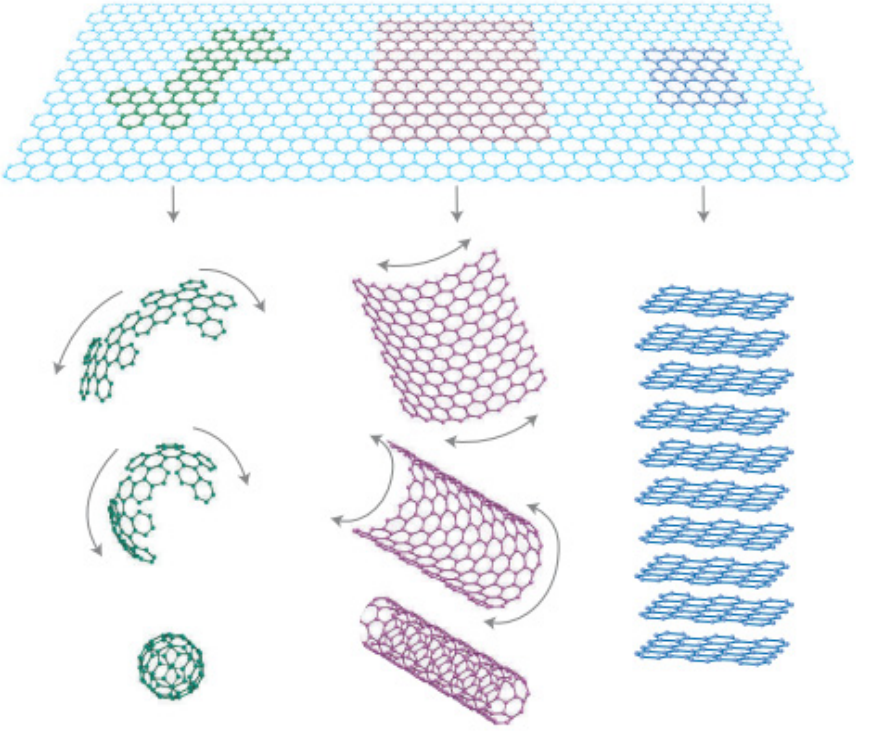

Figure 1. Graphene is a basic unit for all graphitic materials [42].

Each carbon atom in graphene is ~1.42 Å away from its three neighbors. A carbon atom has the following electron configuration: $1s^2 2s^2 2p^2$. In the excited state one of 2s electrons is promoted into a partly empty 2p-orbital, so the electron configuration becomes $1s^2 2s^1 2p^3$. Consequently, four electrons will be available for bonding in the excited state. Each carbon atom in graphene bonds to the three neighboring carbon atoms via in-plane σ-bonds formed from 2s, $2p_x$, $2p_y$ hybridized orbitals (sp^2 orbitals). The σ-bonds give graphene its structural rigidity; they are localized and do not contribute to the electrical conduction [43]. The remaining p_z-orbital is perpendicular to the graphene plane and overlaps with the neighboring p_z-orbitals forming a π-bond. The π-bonds contribute to electrical conduction of graphene.

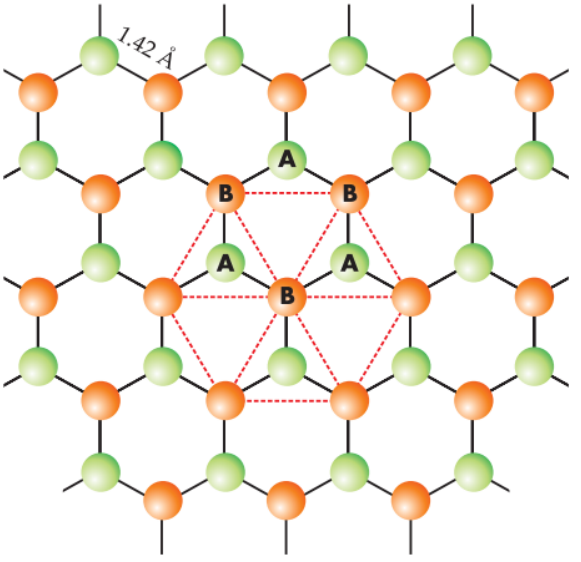

Figure 2. The lattice structure of graphene consisting of two interpenetrating triangular lattices A and B [44].

The two-dimensional hexagonal lattice of graphene is shown in Figure 2. The structure consists of two interpenetrating triangular sublattices in such a way that the atoms belonging to one sublattice are at the centers of triangles defined by the other. Thus, each graphene unit cell contains two carbon atoms A and B [44]. Two π-orbitals of graphene unit cell disperse to form bonding orbital (valence band) and anti-bonding orbital (conduction band) [45]. The conduction band and valence band form conical valleys that touch at the corners of the graphene Brillouin zone. This makes graphene a gapless semiconductor. Among the six corners, there are two kinds of corners (designated as K and K' points). These two kinds of corners are inequivalent with each other. In contrast to conventional semiconductors in graphene near K and K' there is a linear relation between the band's energy and momentum (Figure 3)[44]. This is a consequence of the quantum-mechanical hopping between the two graphene sublattices [46]. The

linear dispersion relation in graphene can be described by the Dirac equation for relativistic massless fermions rather than by the Schrödinger equation [44]. Therefore, K and K' points are also named Dirac points. Because of the linear spectrum, graphene charge carriers act like relativistic particles with zero rest mass leading to ultrahigh carrier mobility. If all extrinsic scatterings are eliminated, graphene intrinsic mobility of 2×10^5 cm^2 V^{-1} s^{-1} can be achieved at room temperature [47]. Moreover, even for high charge carrier concentration, mobility in graphene remains still high [42]. Another remarkable feature is that in contrast to conventional semiconductors in graphene charge carriers can be modulated continuously between electrons and holes [42].

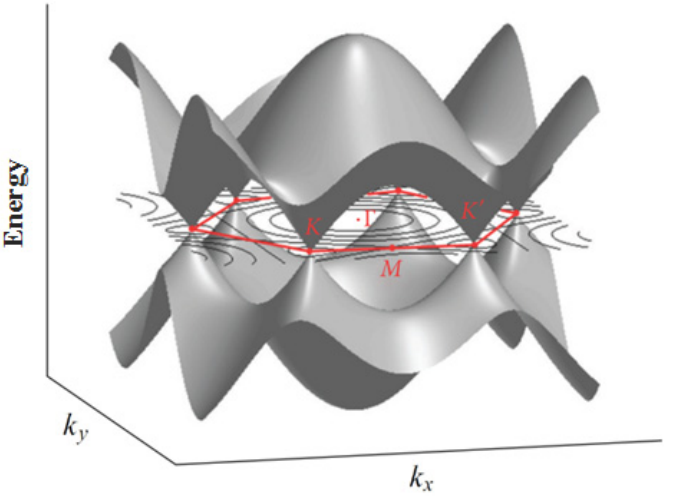

Figure 3. First Brillouin zone (depicted in the horizontal plane) and band structure of graphene. K and K' points are the two nonequivalent corners of the zone, and M is the midpoint between them. Γ is the zone center [45].

However, while charge carriers' density vanishes near Dirac point, graphene conductivity never drops to zero [39]. The origin of the nonzero minimal conductivity of graphene is debated. The Dirac nature of graphene charge carriers is supported by the observation of the anomalous quantum Hall effect in graphene [48]. Noteworthy, the observation of the quantum Hall effect in graphene is possible even at room temperature. Among other remarkable quantum electrodynamic properties of graphene are Klein tunneling paradox and breakdown of the Born-Oppenheimer approximation [49].

Graphene also has remarkable optical properties. The one layer of graphene absorbs 2.3% and transmits 97.7% of incident light independently of the light wavelength [50]. Unusually high absorption of the atomically thin material is defined solely by the fine structure constant that describes the coupling between light and relativistic electrons [50]. The absorbance of few-layer graphene (FLG) sheets is roughly proportional to the number of layers. Such a linear dependence of the absorbance is related to the two-dimensional gapless electronic structure

of graphene [49]. On the contrary, the reflectance of graphene is very low: < 0.1% [50].

The mechanical properties of graphene are also exceptional. The defect-free graphene sheet is the strongest material ever tested [51]. On the scale of tens of nanometers, graphene is also exceptionally rigid. Micrometer-sized graphene, however, readily conforms to the underlying substrate [40]. Without a substrate, large-scale graphene bends easily because of its atomic thickness. Due to the π-bonds graphene tends to be planar, but the resistance to bending is not so strong to prevent it. Thus, graphene has very high tensile strength due to covalent bonding, but when the dimensions of graphene sheet increase its thickness more than 10^4 times, it becomes weak against flexing motion [40].

Graphene is stable in spite of the predicted limitations of two-dimensional crystals [52]. Mermin–Wagner theorem proves that the amplitude of long-wavelength fluctuations grows logarithmically with the scale of the 2D structure and the long-range order will be destroyed in the 2D crystal of infinite size [52]. TEM studies, however, have been demonstrated that graphene does not only show a long-range order but also exists without a substrate [53]. The key to the stability of graphene can be the short-range distortions of the graphene lattice where carbon atoms are shifted regularly in opposite directions relative to the plane [54]. In addition, TEM inspection revealed that suspended graphene sheets are corrugated within the submicrometer area [53]. The authors believe that micro-scopic bending of graphene in the third dimension provides another explanation of the stability of the 2D membrane. There is still no conclusion on whether the observed corrugations are intrinsic [55] or a response to the strain from boundary conditions [40].

2.2. Graphene preparation methods

2.2.1. Exfoliation methods

2.2.1.1. Micromechanical exfoliation

The micromechanical exfoliation of graphite is a technique that allowed isolation of graphene for the first time. Micromechanical exfoliation, also called as “Scotch tape” method, involves repeated “peeling” of highly-oriented pyrolytic graphite using adhesive tape with subsequent transferring of the thinned down graphite to oxidized silicon wafer [56]. Graphene being placed on a silicon substrate with a 300 nm thick layer of SiO_2 can be discerned from the substrate despite its atomic thickness [57]. Graphene’s visibility is a result of interference with SiO_2, which acts as a spacer [58]. In the first experiments, the thin flakes were transferred by dissolving the scotch tape`s glue in acetone [56,59], further by rubbing against the oxidized silicon wafer surface [39]. When placed on the silicon wafer with a 300 nm-thick oxide layer, even SLG gives enough contrast for the flake to be visible under the optical microscope [60].

The ease of graphene production by micromechanical exfoliation and the high quality of the obtained samples made this method widely used in scientific experiments. Although the fine-tuning of the method allows now to produce graphene flakes up to 1 mm is size [61], the micromechanical exfoliation is not suitable for large-scale graphene production. This method is of low-yield and produces randomly placed graphene flakes accompanied by thicker flakes.

To achieve large-scale production of graphene, other exfoliation methods were developed. These methods use the root idea of the cleavage of graphene layers from the bulk graphite.

2.2.1.2. Ultrasonication

In the ultrasonication method, graphite is sonicated in a suitable liquid medium [62]. The exfoliation mechanism stems from shear forces and cavitation induced tensile stresses acting on graphene layers during sonication [62]. After removal of thick graphitic flakes by centrifugation, a graphene dispersion is obtained [63]. Hernandez et al. have concluded by testing various solvents that the solvents with the surface energy close to the surface energy of graphene (e.g., N-methyl-pyrrolidone) favor the exfoliation process the most [63]. For industrial-scale production, these solvents, however, might not be the best choice due to environmental hazard issues, relatively high cost and high boiling point, which makes deposition of graphene from dispersion to the desired substrate and removal of the solvent residues more difficult. Due to the aspects mentioned above, water has been widely employed as a sonication medium [64,65]. Different additives (dispersants) such as surfactants [66,67], ionic liquids [68,69], polymers [70,71] and biomolecules [72,73] are commonly added to water to improve initially poor exfoliation efficiency and impede restacking of graphene layers after sonication. The additives, however, may negatively affect graphene intrinsic properties [74] and their removal after graphene deposition onto substrates can be troublesome [75]. Conversely, graphene-additive combinations may show synergic properties desirable for novel hybrid materials [76,77]. Furthermore, additives can contribute to charge development on the graphene surface, which can be used for controlled graphene deposition on the surfaces with different morphologies by electrophoretic deposition [78,79]. An alternative approach to increase graphene exfoliation efficiency is to adjust graphene solubility by mixing water with another cheap solvent with low boiling point like acetone [80], ethanol [81,82] or isopropanol [82]. Sometimes the combination of different approaches can be used to increase exfoliation yield [83,84]. The sonication-assisted exfoliation is considered a mild technique, but prolonged sonication times are associated with a size reduction of the exfoliated flakes [85]. Another drawback of the method is that in addition to SLG and FLG, thin graphitic sheets can also be present in obtained dispersions [85].

2.2.1.3. Ball-milling

The ball-milling is another exfoliation method used for graphene production. The shear forces the ball-mill exerts on graphite lead to exfoliation of graphite into FLG and SLG flakes. Grinding can be performed in a dry or wet environment. This method is simple, low cost and provides high exfoliation yield, but the dimensions of the obtained flakes are still small, and it is difficult to control the precise number of graphene layers [86,87]. Moreover, the collisions during milling can lead to fragmentation and defects.

2.2.1.4. Hydrodynamical exfoliation

Graphene exfoliation method using fluid dynamics events was recently proposed [88]. Rapid fluid movements generated in the rotating tube or high-shear mixer can split stacked carbon layers [62,88,89]. This exfoliation method consumes less energy than sonication and avoids harsh cavitation process [89,90]. By using high-shear mixing, it is possible to prepare graphene in large quantities, but the mean size of the produced graphene flakes is under one μm [89]. Furthermore, like other liquid exfoliation methods, it suffers from organic solvent or surfactant contamination [91].

2.2.1.5. Mechano-chemical exfoliation

Oxidation of graphite with the formation of oxygen-containing groups can also be used to weaken the interlayer interaction [92]. The oxidized graphite, called graphite oxide is hydrophilic and by using moderate sonication it can be exfoliated in water producing graphene oxide sheets. The graphite oxide is mostly produced by the Hummers' method [93] – treating graphite with a mixture of sodium nitrate, concentrated sulfuric acid and potassium permanganate, or its modifications [94]. Produced graphene oxide is further reduced using various reduction methods, like chemical one, e.g., by hydrazine hydrate, heating in the vacuum or electrochemical reduction [95]. While this method allows obtaining graphene at low cost and in large quantities, it is still hard to remove all oxygen-containing functional groups bonded to graphene and even after reduction of these groups the conjugated graphene network may not be recovered [96]. Since the properties of graphene produced by this method are significantly inferior to pristine graphene, it is usually referred to as reduced graphene oxide instead of graphene [96].

2.2.2. Growth methods

While the methods mentioned above are based on splitting graphite into atomic layers, the alternative way is to synthesize graphene from another carbon source. One of these methods is the thermal decomposition of silicon carbide (SiC) [97]. The SiC is thermally treated at high temperature (>1100 °C) typically in ultra-high vacuum conditions which results in the sublimation of silicon atoms due to the difference in the vapor pressures of silicon and carbon, and the carbon-enriched surface undergoes reorganization and graphitization [98]. The growth of graphene in argon atmosphere has been demonstrated both Si-terminated and C-terminated faces of the {0001} surface of SiC single crystal. On the Si-terminated face, the number of obtained graphene layers is governed by the growth temperature [99]. The disadvantage of graphene grown on the Si-face is the formation of the buffer layer between graphene and silicon carbide. This buffer layer has a graphene-like honeycomb structure with about 30% of its atoms covalently bonded to the silicon atoms of the SiC(0001) surface. Due to the covalent bonds with the substrate, the buffer layer is strained, corrugated, and lacks the electronic properties of pristine graphene [100]. Moreover, the buffer layer has a negative effect on the electrical properties of the graphene layer above [101,102]. The buffer layer is absent when graphene is grown on C-face of SiC, but due to different nucleation mechanism, the multilayer graphene is obtained on this face [103]. On the Si-face, the steps on the substrate can also be covered with more than one graphene layer [104]. Better control of the surface morphology can be achieved by growing graphene in argon atmosphere close to atmospheric pressure in comparison to the vacuum graphitization. The higher argon pressure leads to a reduced silicon evaporation rate, so much higher (1650 °C) growth temperature can be used. At higher temperature, the reconstruction of the surface is completed before graphene is formed, which results in larger lateral dimensions of SLG coverage [104]. Although high-quality graphene has been obtained, the graphitization of SiC has several drawbacks. The SiC wafers are expensive, and the requirement of very high temperatures leads to elevated process cost. Moreover, the size of the synthesized graphene is limited by the SiC wafer size.

Another bottom-up synthesis method to produce high-quality graphene is chemical vapor deposition. The method uses the catalytic decomposition of carbon-containing gas or less frequently liquid or solid precursor's molecules on transition metal surfaces. Compared to the decomposition of SiC, CVD process is conducted at a lower temperature ≤ 1000 °C and allows synthesis of significantly larger graphene sheets, e.g., the successful synthesis of 100-m long graphene on a copper foil with subsequent transfer to polymer film has been demonstrated [105]. Graphene growth has been demonstrated on Ru [106], Ir [107], Co [108], Ni [109], Cu [110], Pt [111], Au [112], Pd [113], Fe [114], Re [115] and Rh [116], where depending on carbon solubility in metal and growth conditions SLG, FLG or MLG graphene is produced. From an industrial point of view, copper and nickel catalysts are of particular interest because of their availability and low cost.

Metal catalysts in the form of single crystals, metal films deposited by electron beam evaporation or sputter coating and polycrystalline foils can be used for graphene growth. The foils are inexpensive and available in large sizes and thus are beneficial from the economic point of view and feasible for industrial applications. The methane is the most widely used carbon precursor for the graphene synthesis. However, as it has been demonstrated by Ruan et al. [117], in principle, any carbon-containing feedstock is suitable for graphene synthesis. In the typical CVD process, a metal catalyst is first annealed in argon/hydrogen flow, and then a hydrocarbon gas is introduced into the system. The hydrocarbon gas then catalytically decomposes on the metal surface to carbon adatoms, which then form SLG and/or FLG. The quality of the synthesized graphene varies depending on synthesis conditions and the character of the substrate. The large-area graphene films synthesized are typically polycrystalline.

2.2.3. Other methods

In addition to the methods reviewed above, some other less widespread methods have also been developed for graphene production. In 2008, Choucair et al. synthesized graphene by pyrolysis of sodium ethoxide, obtained via solvothermal route [118]. Later the direct solvothermal process in the autoclave, without post-pyrolysis step was proposed for graphene [119] and n-doped graphene [120]. This wet chemical approach for graphene synthesis is rather attractive due to its simplicity and commercial viability, though only small-area graphene sheets can be obtained. The reaction product can also be contaminated with amorphous carbon [119].

Another method is graphite exfoliation in a supercritical fluid [121–124]. A supercritical fluid has both gaseous and liquid properties. As a gas, it has high diffusivity, low viscosity, and zero surface tension, but similarly to liquid is capable to dissolve materials [121]. These features make supercritical fluid a solvent of choice for intercalation of the layered structures [124]. In this method, graphite is immersed in the supercritical fluid in the sealed vessel for some time, followed by rapid depressurization. A supercritical carbon dioxide [121,124], ethanol [122], N-methyl-pyrrolidone [122], dimethylformamide [122,123] have been used for graphene exfoliation. The advantage of the supercritical carbon dioxide is that it evaporates during depressurization leaving no solvent residues [121].

The exfoliation of the graphite can also be achieved by laser beam irradiation [125–127]. Laser influence induces a vibrational excitation of the graphene planes, which causes the collision of the upper planes during which the surface plane receives sufficient momentum to leave the HOPG crystal [128]. In order to avoid the damage of the graphene sheet, the photon energy of the laser should not exceed the C–C bond energy (3.7 eV).

The unzipping of carbon nanotubes (CNT) is also one of the methods for graphene production. In this process, CNTs are fractured along their longitudinal

axis with the formation of graphene nanoribbons. Various techniques have been reported for this purpose. CNTs can be unzipped by a chemical treatment with H_2SO_4 and $KMnO_4$ mixture, plasma etching, intercalation with alkali metal atoms, passing a high current through the tube or calcination followed by sonication [129].

2.3. Chemical Vapor Deposition

2.3.1. Principles of Chemical Vapor Deposition

Chemical vapor deposition is a synthesis method, which involves chemical reaction (including dissociation reaction) of gaseous precursors in the vapor phase near the substrate surface or on its surface with a formation of a solid deposit [130,131]. For the deposition of the films, the process conditions are tailored to favor the heterogeneous reaction [131]. The reaction is generally also accompanied by the formation of gaseous by-products that are transported out of the chamber along with unreacted precursor gases [132]. The energy required for the CVD reaction can be provided by thermal, photon or plasma activation [132]. There are two basic reactor types used for conducting a CVD process: "closed reactor" and "open reactor". Nowadays most CVD processes are performed in the "open reactor", where the continuously delivered precursors flow through the reactor [131]. The deposition process and processing parameters affect the nucleation and growth of the synthesized material.

2.3.2. Factors affecting graphene synthesis by the CVD method

The CVD of graphene is based on the catalytic decomposition of carbon precursors on transition metals. The catalytic power of transition metals stems from their incomplete d-orbitals. The outcome of the synthesis is largely dependent on the transition metal utilized as a catalyst. Metals with high carbon solubility like rhenium, ruthenium, rhodium, nickel, and cobalt at a high temperature can store much more carbon than it is needed for a single-layer formation on the surface of their bulk crystals or films. As a result, the carbon segregation during their cool-down will lead to the MLG formation on their surface. The amount of dissolved carbon, however, can be adjusted by reducing the thickness of the catalyst substrate and controlling the hydrocarbon exposure [109,133]. The graphene synthesis on transition metals with very low carbon solubility like iridium, copper, gold and platinum results in predominantly SLG. As in the absence of precipitation, there will be no carbon supply when the whole catalytic surface is covered with graphene.

The growth of graphene is also affected by the interaction of growing graphene sheet with the underlying metal. The interaction varies from pure physisorption to relatively strong chemisorption [134]. Graphene interacts weakly with copper, silver, iridium, platinum, and gold, but on the contrary, the strong interaction has

been observed on nickel and cobalt. On ruthenium, rhenium, rhodium, and palladium the interaction between carbon and metal atoms varies across the unit cell depending on the adsorption site of the carbon atoms giving rise to the corrugation of the graphene sheet [135]. The weak interaction of graphene with the metal results in the formation of various rotational domains, which leads to the formation of grain boundaries as these domains stitch together. The grain boundaries, in turn, have a negative effect on graphene properties. On the other hand, the weak interaction allows the continuous growth over edges and steps on the substrate surface [136]. Whereas, for example, the strong interaction with ruthenium step edges has been showed to prevent the graphene growth in a step-up direction [135].

The metals also differ in their effectiveness as the catalysts for dissociative chemisorption of hydrocarbons and graphitization. For example, the dissociative chemisorption of methane on Cu(100) is five orders of magnitude lower compared to Ni(100) surface [137]. The catalytic activity of a metal is related to its electronic structure. Metals with few unpaired electrons in the outer d-orbital show higher catalytic activity compared to the metals with full outer d-orbitals.

Prior to a graphene synthesis, the pretreatment of catalyst substrate is generally required. The goal of the pretreatment step is to improve the surface of the metal catalyst to obtain the graphene with better quality. One common pretreatment strategy is to make the metal surface more uniform by removing surface contamination/oxide layer and various imperfections. For that purpose, various surface pretreatments such as soaking in dilute acid [138], mechanical [139] and/or electrochemical polishing [140,141], sonication in acetone [136,142] as well as prolonged annealing in reducing atmosphere [141–143] have been reported. From the mentioned above, the annealing in Ar/H_2 mixture is the most used treatment, as in addition to removal of native oxide and smoothing the surface, it allows improving the microstructure and texture of the catalyst [144]. Another emerging pretreatment strategy is to preserve the oxide layer on the metal surface up to initiation of the graphene growth by heating the substrate to the growth temperature in air or pure argon. The oxide layer on the catalyst leads to the drastic suppression of graphene nucleation density and significant increment in the size of graphene domains [141,145].

CVD of graphene can be conducted at atmospheric pressure (AP), low pressure (LP) (0.1–1 mbar) or in ultrahigh vacuum (UHV) conditions [146]. Conducting CVD in UHV allows better control of the growth process; making it possible to obtain SLG on most of the graphene catalyzing metals (including nickel) if clean single-crystalline substrates are employed [135]. However, UHV conditions are not viable for graphene production on an industrial scale due to high expenses on maintaining ultrahigh vacuum systems [147], and thus, these are mostly used for studying the mechanism of graphene growth in accordance with the requirements of surface sensitive characterization methods. From an economic point of view, the atmospheric pressure CVD is the most advantageous. However, it was reported that the increase in the chamber pressure could have an adverse effect on graphene quality. For catalysts with high carbon solubility, it is

more difficult to control carbon precipitation at APCVD conditions [148]. Furthermore, Bhaviripudi has studied the role of pressure of the reaction chamber in CVD synthesis of graphene on low carbon solubility catalyst [146] and has found that in contrast to LPCVD, in APCVD the growth of graphene on copper is not self-limiting, and multilayer domains can be obtained if the hydrocarbon pressure is not optimized. Besides, graphene synthesized at APCVD had a higher density of defects and inferior uniformity compared to LPCVD synthesis. It is generally believed that at high temperatures at atmospheric conditions the rate-limiting step is the diffusion through the boundary layer, the thickness of which is affected by the geometry of CVD chamber and the effects of gas flow. A variation in the thickness of the boundary layer results in thickness inhomogeneity of the synthesized graphene. At low total pressure, the diffusion through the boundary level is enhanced and is no longer the rate-limiting step. At LPCVD, the growth becomes surface-reaction limited and higher graphene uniformity can be achieved over large areas [146]. The higher defect density at APCVD conditions can be explained by significantly higher graphene nucleation density compared to LPCVD due to a lower activation energy of graphene nucleation [148]. Higher nucleation density results in higher grain boundary densities, and thus a higher number of defects. It should be noted, however, that a low pressure at the high growth temperatures promotes a sublimation of the catalyst.

Another critical parameter of CVD graphene synthesis is a growth temperature. In conventional CVD, the temperature range of 800–1000 °C is usually employed for most of the catalysts [148]. Although the temperature at which graphene can be synthesized largely depends on the utilized metal catalyst and hydrocarbon precursor, the improvement of the quality of graphene with an increase of the growth temperature is the overall trend. The decreased number of defects with increasing the temperature has been reported on copper [149], nickel [150], and iron [151] with no detectable defect-related band observed in Raman spectra of graphene synthesized at 1000 °C. Besides the number of defects, the growth temperature was reported to affect the orientation of graphene domains relative to the catalyst surface. For iridium, multiple domains are observed at low growth temperatures, but a single-domain structure can be obtained at high temperature [135]. A similar observation was made on Cu(111) [149], but the rotational boundaries were still observed even at the high temperature due to misalignment of graphene domains after overgrowing the step edges on the copper surface. In turn, the density of the grain boundaries is also influenced by temperature. Higher temperature favors the formation of larger graphene domains [141,152], which is related to the lower nucleation density of graphene due to significantly increased desorption rate of carbon-adatom species [153]. It should be noted, however, that higher temperature increases the possibility of saturating the catalyst with carbon, which can result in a larger number of graphene layers [154].

The exposure time to hydrocarbon precursor should be sufficient to ensure the merging of individual graphene domains into a continuous graphene sheet. At the same time, more prolonged exposure to the carbonaceous source in common with high hydrocarbon concentration leads to the formation of a higher number of

graphene layers [150,155,156]. It has been shown that even on copper, where the growth is considered to be "self-limiting", additional graphene layers can nucleate at the metal-graphene interface despite the full coverage of the catalyst surface [154].

The partial pressure of the hydrocarbon precursor is an important parameter, which affects graphene nucleation density. For a low seeding density, it is favorable to use a low concentration of the precursor [157]. Too low concentration, however, leads to the formation of separate graphene domains instead of the complete coverage of the catalyst [136,158]. Besides, on metals with high carbon solubility, by changing hydrocarbon concentration, it is possible to affect the thickness of few- or multi-layer graphene sheet [150,155,159].

During synthesis, the hydrocarbon precursor is mixed with argon and hydrogen. The partial pressure of hydrogen used during the synthesis varies immensely among publications. Initially, the hydrogen gas was regarded solely as a reducing agent maintaining the metal surface free of oxide during the graphene growth. Later it was proposed by Vlassiouk [160] that hydrogen may also serve as a cocatalyst promoting the chemisorption of methane with the formation of more active surface-bound methyl radical. The above assumption was made based on the observed dependence of the graphene growth rate on the hydrogen partial pressure: the graphene growth at APCVD had initiated only when the hydrogen partial pressure was sufficiently high, and the maximum growth rate was achieved when the hydrogen partial pressure was 200–400 times that of methane. The evolution of the graphene domains at high hydrogen partial pressure from irregularly shaped with small bilayer region to perfect single-layer hexagons further corroborated the distinct role of hydrogen in graphene growth. The observed shape change of graphene domains, as well as the saturation of the growth speed at high hydrogen partial pressures, was explained by the reaction of hydrogen radicals with the carbon-carbon bonds of lower stability catalyzed by transition metal surface. The etching of graphene at high hydrogen partial pressure has been later reported by several other groups both at atmospheric and low-pressure conditions [144,150,161] More recently, however, Choubak et al. demonstrated that no graphene etching takes place when purified hydrogen is employed, while graphene sheets exposed to unpurified hydrogen were notably etched apparently by the residual oxygen or other oxidizing impurities [162]. The concomitant etching by oxidizing contaminants explains well the inhibition of graphene growth in the absence of H_2 and questions the necessity for "activation of the surface-bound carbon by hydrogen" reported earlier [160]. Indeed, it has been demonstrated that if the presence of oxidizing impurities is below 1 ppb, hydrogen is not required for graphene growth from methane [163]. In practice, however, it is challenging to limit the presence of oxidizing impurities to such a degree, and the flow of pure hydrogen is helpful to prevent graphene from etching and amorphization [164]. Whether all observed effects of the hydrogen partial pressure on graphene growth can be explained by its counteractive action on oxidative species, is not clear yet. Among other possible factors is the reduction of surface sites available for dissociation of methane due to chemisorptions of

hydrogen on the catalytic metal surface [137]. The adsorbed hydrogen has also been shown to alter the migration and polymerization speed of carbon on metal surfaces [165]. In addition, according to ab-initio calculations at low hydrogen pressure the edges of graphene are bound to the catalytic metal surface, whereas at high hydrogen pressure the edges of graphene are terminated by hydrogen and, therefore, detached from the metal surface, which facilitates migration of active carbon species underneath the first layer of graphene and formation of the adlayer [166].

2.4. Graphene transfer methods

After CVD synthesis, graphene can be separated from the catalyst metal and moved to the desired substrate. Nickel and copper can be readily removed by etching. The most widely used etchants are iron chloride, iron nitrate and ammonium persulfate [167]. Nitric acid is also an effective etchant, but the release of the gas during the reaction can break a graphene sheet. The etching is performed by immersing the catalyst substrate covered with graphene into the etching bath. When the metal foil is used for graphene synthesis, graphene is formed on both sides of the foil. In this case, it is preferable to remove graphene from one side of the foil, e.g., by argon plasma prior to etching.

Before metal etching and a subsequent transfer, the graphene film is covered with a support polymer. Support polymer facilitates handling of graphene film after etching of the metal and prevents it from folding and tearing during the transfer process. The most popular supports for graphene transfer are polymethylmethacrylate (PMMA) [168], polydimethylsiloxane (PDMS) [169] and thermal release tape [170].

The general transfer using PMMA is the following. First, the graphene-covered metal sample is spin-coated with a PMMA solution. When a solvent is evaporated, and PMMA is solidified, the sample is placed into an etching solution until the transparent PMMA/graphene membrane floating on the etching solution can be seen. The floating PMMA/graphene membrane is then cleaned in deionized water and is captured by the target substrate. When water is evaporated, and good contact between PMMA/graphene and the substrate is obtained, the PMMA is dissolved in acetone or dichloromethane [168]. Often the annealing of transferred graphene is performed at 200–300 °C to get rid of PMMA residues. This method generally yields high-quality transferred graphene films with the reported mobility as high as 16 000 $cm^2V^{-1}s^{-1}$ [152]. Nevertheless, water residues that could be trapped between graphene and the substrate have been shown to introduce a disorder affecting graphene electrical properties [171].

In the PDMS-mediated transfer, metal/graphene sample is directly attached to the PDMS stamp [169]. Alternatively, the liquid PDMS is poured onto the graphene [172]. When a solution-phase PDMS is used, a better contact between graphene and polymer can be achieved [172]. In contrast to PMMA-mediated transfer, no PDMS dissolution is generally required. The PDMS has low surface

energy and does not adhere strongly to graphene. Once PDMS supported graphene with the removed metal catalyst is brought into contact with target substrate, PDMS stamp can be peeled back, leaving graphene on the substrate [167]. In the case of multilayer graphene, the top graphene layers can be transferred without etching of the metal substrate [172] as PDMS adhesion to graphene can excel the adhesion between adjacent graphene layers. This allows avoiding the contamination of the graphene with metal impurities originating from etching solution and incomplete catalyst etching [173]. In addition, the catalyst substrate can be reused. The nearest to catalyst graphene layer, however, has greater adhesion to the substrate compared to PDMS and therefore cannot be transferred without etching of the metal.

For large-scale transfer of graphene in the industrial process, it is convenient to use thermal-release tape (Nitto Denko Revalpha). The thermal-release tape adheres to graphene at room temperature but can be easily peeled off by heating. As in the previous transfer methods after attaching graphene to the tape, the etching of the metal substrate is performed. The hot pressing or roll-to-roll processes can be used to transfer graphene from the tape to the desired flexible or rigid substrates, accordingly [167]. The roll-to-roll process allows the continuous transfer of graphene at meters' scale on flexible substrates. The hot pressing process, however, results in less mechanical defects in graphene films transferred to rigid substrates [174].

2.5. Scanning electron microscopy

2.5.1. Basics of the image formation

The working principle of the scanning electron microscope (SEM) is based on scanning of the sample surface with an electron beam (e-beam). Primary electrons generated by electron gun are focused into a small-diameter electron probe that is scanned, usually digitally, across the specimen. E-beam scanning is realized by using scanning coils/plates, which deflect the e-beam using a magnetic/electric field. The e-beam is principally deflected in two perpendicular directions, sequentially covering the rectangular area on the sample (a raster). The signal intensity derived from the interaction of the e-beam with the specimen at every point is converted to gray level values on the display screen, producing an image. If the raster scanned by the e-beam on the specimen is smaller compared to the raster displayed on the screen, a magnified image is produced [175,176].

Two signals, generally used to form SEM images, are secondary electrons (SE) and backscattered electrons (BSE). By definition, SE are all electrons emitted from the sample with energy less than 50 eV. Since SE generally receive only a small amount of energy from the primary electron upon their generation, they can lose all of their kinetic energy before reaching the surface of a sample. Furthermore, at least part of the remaining energy is required to overcome a surface potential barrier. As a result, despite being produced along the entirety of

the trajectories of primary electrons within the sample, only those generated in the vicinity of the surface will contribute to an SEM signal. [177]. The maximum depth of emission for SE is for metals about 5 nm and 50 nm for insulators. The shallow escape depth makes the SE signal very sensitive to surface features. The sensitivity to surface features can be further improved by using low electron accelerating voltages ($\leq$ 5 kV).

Backscattered electrons are the e-beam electrons the trajectories of which have intercepted sample surface, but not necessarily their exact entrance surface, and therefore escaped from the sample. As a rule, these electrons have undergone multiple elastic scattering events to accumulate sufficient deviation from the initial trajectory to return to the surface. A small fraction of the probe electrons, however, backscatter elastically with a sufficiently large angle immediately upon entering the specimen [177]. The BSE energy range is broad, by convention it is from probe electrons' energy to 50 eV [178], but the majority of BSE retain at least 50% of the primary beam energy. As a consequence, BSE can escape from significantly larger depths in comparison to SE. The BSE signal can, therefore, be sensitive to subsurface features of the sample structure [177].

The SE and BSE yield is a minimum when the surface of a sample is perpendicular to the electron beam [175]. On the tilted surface, more SE are generated within their escape depth, and therefore, a higher number will be able to escape. Edges and the protruding parts of surfaces hence produce more SE [176]. The backscatter coefficient also increases as a monotonic function of the surface tilt. Thus, the number of emitted SE and BSE from every point irradiated by e-beam provides information on the inclination of the local specimen surface. However, the number of the BSE measured also depends on the orientation of the surface to the detector because in tilted regions, the majority of BSE move in a forward-scattering direction [177]. The standard detector for SEM observation – the Everhart-Thornley detector is located on the right side of the microscope chamber below the electron column. Thus BSE will be efficiently collected from the sample areas facing the detector making these areas appear bright in the image. In contrast, few BSE will reach the detector from areas inclined to the other side from the detector, and these areas will appear dark. The number of the detected SE also depends on the position of the detector relative to the surface under observation. However, due to their low energy, the trajectories of SE can be altered by the positive bias of the collector grid in front of the Everhart-Thornley detector, which significantly increases the SE collection efficiency even from the areas not facing the detector. This results in the reduction of the directional contrast, still the SE collection efficiency will be highest in the areas facing the detector. If the Through-the-Lens detector is used instead of the Everhart-Thornley detector, SE electrons are most efficiently collected from the surface perpendicular to the electron beam. Hence, the topographic contrast in the obtained image is a function of the number of detected BSE and SE, which in turn depends on local surface geometry, the type of the detector and its position with respect to the sample [177].

SEM images can give the information not only about surface topography but also about the composition. The pure SE yield is relatively insensitive to atomic number, except for carbon and gold with anomalously low and anomalously high yield, respectively [177]. On the contrary, as the yield of BSE increases with increasing atomic number, the regions of the sample with a higher mean atomic number will appear brighter. In addition, BSE from targets with higher atomic number tends to be more energetic. In turn, the efficiency of the most BSE detectors generally increases with the energy of the BSE [177]. Therefore, the contrast between areas with a different atomic number can be even more pronounced.

2.5.2. Crystallographic information from the SEM

When the electron beam strikes a surface of a polycrystalline material, the density of atoms it encounters depends on the crystal orientation. At directions of lower atomic density, the electrons can penetrate deeper into the sample before they are scattered. The futher the scattering starts from the sample surface, the lower the probability for the backscattered electron to reach the surface. If the crystal orientation has a dense atom packing, the scattering of electrons starts at the surface instantly, and the BSE yield of this surface will be higher than that of the amorphous surface [177]. Thus, the BSE coefficient is dependent on the orientation of the crystal with respect to the incident beam. As a consequence, grains with different crystallographic orientation exhbit different grey levels in the image. Though the magnitude of variation in the BSE yield rather is small, this crystallographic (electron channeling) contrast can be utilized to obtain information about the microstructure of crystalline materials [175,177].

However, in certain cases, it is necessary to determine the actual orientation of the crystal. Different gray levels in SEM image showing crystallographic contrast do not give quantitative information about the crystallographic orientation of grains. However, the electron channeling can be used to form diffraction patterns [175]. The local crystallographic orientation of a surface can be determined quantitatively by electron backscatter diffraction (EBSD) technique.

EBSD operates by arranging a flat sample at a shallow angle, usually 20°, to the incident electron beam (Figure 4). When electron beam points the crystal lattice, the diffracted electrons form flat cones of intensity above the sample. As the electrons can diffract from both sides of the atomic planes, two cones of diffracted electrons are produced on each atomic plane. If to place a phosphor screen adjacent to the tilted specimen, in the way of diffracted electrons, these pairs of cones will be displayed as two almost straight lines, which are called Kikuchi lines. The EBSD pattern consists of many Kikuchi lines, which intersections correspond to the zone axes, while the distances between them to the angles within the crystal. [177,179].

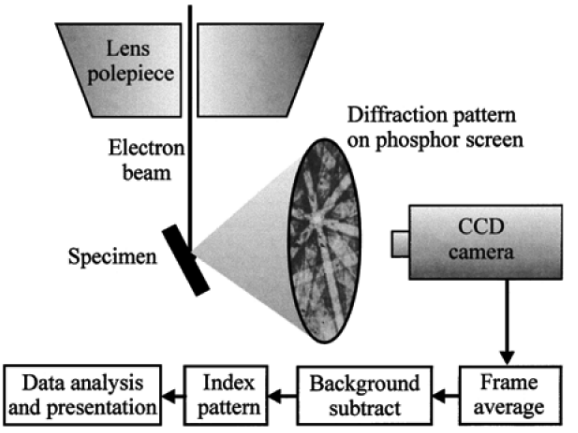

Figure 4. Schematic diagram of the EBSD technique [180].

The EBSD pattern produced on the phosphor screen is recorded using a CCD camera. Before the EBSD pattern can be analyzed, the averaging of several recorded image frames is usually required to improve the signal to noise ratio. The diffraction pattern is analyzed by the software, which measures the position of the lines and angle between them, comparing them to the predicted for given crystal structure [175]. The nominal angular resolution limit is ≈ 0.5°, and the spatial resolution correlates with the resolution of the SEM in backscattered electron imaging [179]. Extensive data can be received by scanning the e-beam over the sample and measuring the orientation at every step. The obtained data can be used to visualize the variation in crystallographic orientation over the sample. By using these orientation maps, the information about grain sizes and shapes, orientation, texture, misorientation and phase distribution can be obtained [175].

2.5.3. SEM studies of graphene

Despite its atomic thickness, graphene can be imaged by SEM. The contrast mechanism under graphene imaging has been debated. Obviously, graphene is too thin to produce thickness contrast. Nevertheless, graphene-covered areas and bare substrate have different brightness levels on SEM micrographs. The areas with a different number of graphene layers can also be distinguished by discrete shifts in contrast. The contrast between individual graphene layers is especially prominent at low accelerating voltages [181,182]. Currently, the most feasible explanation of the observed contrast is the attenuation of secondary electrons emitted from the substrate under graphene [182]. This explanation is consistent with signal intensity dependence at graphene region on a number of graphene layers [181,182]. The observations of graphene growth in situ by SEM, though, pointed out that graphene-covered surface and the bare substrate were not

distinguishable prior to the sample air exposure [183,184]. These observations question the ability of graphene to affect secondary electron emission from the underlying substrate considerably. Among other contrast mechanisms reported for graphene imaging is the voltage contrast [181]. The voltage contrast is a result of electric fields developed in response to the charge introduced by the primary e-beam. The voltage contrast can develop when graphene is located on an insulating surface like commonly used SiO_2-covered Si substrate. This contrast mechanism can explain graphene contrast reversal (graphene appears brighter than the substrate) [181,182] at low ($\leq$ 1–2 keV) accelerating voltages.

Although the exact mechanism behind the SEM imaging of graphene is not fully understood, the use of SEM for graphene studies becomes more and more widespread. SEM allows to estimate a homogeneity of a synthesized graphene film, detect the presence of discontinuities and areas of a few or multilayer growth [185]. It can be utilized to monitor graphene growth characteristics like the size, shape, and distribution of graphene domains [186–188].

Graphene studies by SEM are similar to graphene studies by optical microscopy, only in this case, not the color but the brightness values of the graphene-covered surface are compared to the brightness values of the substrate. The resolution of SEM being around 1 nm significantly surpasses the possibilities of optical microscopy. Also, the graphene characterization by SEM can be performed directly on the catalyst surface without the need to transfer graphene to silicon substrate covered with silicon dioxide of the required thickness. In the case of transferred graphene films, SEM can be successfully used to evaluate the quality of the transfer procedure, namely whether the transfer procedure has introduced defects or impurities that can have adverse effects on graphene properties. Usually, SEM instruments are equipped with EDX spectrometers, which allow easily to determine the nature of the contaminants.

Graphene measurement by SEM successfully complements Raman spectroscopy [189]. Raman spectroscopy has become a standard method to determine the number of graphene layers, but it is not that easy with Raman spectroscopy to get the information about the homogeneity of large-area graphene coating. Raman mapping, for sure, can provide information about the homogeneity of the sample, but it is inferior to SEM in a spatial resolution and speed. Due to the lower resolution small discontinuities, cracks and patches of multilayer growth can remain overlooked. SEM, in contrast, can be applied to characterize nanometer-sized defects in graphene. The rapidity of SEM measurement allows to inspect the influence of various synthesis parameters and find optimum conditions for synthesis [190].

Generally, SEM is not employed for the determination of the number of graphene layers, however, such a possibility has been demonstrated for the first time by Hiura et al. [182]. They found a relationship between the SEM contrast and a number of graphene layers on insulating substrates. Further, Kochat et al. presented a quantitative approach for the determination of thickness of graphene films on SiO_2-covered Si substrate based on attenuation of SE by graphene [181]. For correct layer number determination, graphene sample should be measured at

the same imaging conditions as used by Kochat. The method showed its feasibility on the samples with a thickness of up to several graphene layers. In case of graphene on a polycrystalline substrate, the orientation of the crystallites relative to electron beam will affect the secondary electron yield and consequently the signal intensity, which makes the determination of graphene thickness based on the intensity values in an SEM image unreliable.

2.6. Atomic force microscopy

The working principle of atomic force microscopy (AFM) is based on the measurement of the interaction force between a tip and a specimen surface using specially-designed probes consisting of a flexible cantilever and a ultrasharp tip on its free end. At tip-sample separations on the order of several to tens of nanometers the interaction is governed by long-range attractive interactions largely as a result of the van der Waals forces, although at shorter distances, the short-range repulsive interactions start to dominate, which stem from the overlapping of the electron shells of the tip and specimen atoms [191]. Under the force exerted by the surface the cantilever starts to bend. The cantilever deflections are measured as the tip is scanned over the surface of the sample, or conversely, the sample surface is scanned beneath the tip. The deflections of the cantilever are, as a rule, measured with a beam-bounce optical method. In this method, a diode-laser is directed on the rear side of the cantilever right above the tip, and the position of the reflected beam is monitored with a position-sensitive photodetector. The measured deflections of the cantilever allow the software to construct a map of surface topography. Besides interatomic forces, different long-range forces such as magnetic or electrostatic forces can also be detected and mapped. AFM offers high-resolution three-dimensional images of the surfaces of both conducting and insulating samples.

The AFM instrument can be operated in one of three modes: (i) contact, (ii) non-contact (iii) or tapping mode.

In contact AFM mode, the tip of the cantilever is in physical contact with the surface of the sample. As the tip is scanned across the surface (or a surface is scanned under the tip), a repulsive force is detected as an upward deflection of the cantilever [191]. Then either the deflection of the cantilever is used to generate topographic info while the height of the piezoelectric scanner is fixed, or a constant repulsive force is set as a fixed cantilever deflection, and the changes in the height of piezoelectric scanner controlled by z-axes voltage required to keep this constant force are monitored. The constant-height mode is usually a method of choice for obtaining the atomic resolution on atomically flat surfaces, for non-atomically flat surfaces, the constant force mode is appropriate. In contact mode, the tip always exerts a mechanical load on the sample surface, which can lead to damage of the sample or displacement of the molecules weakly bonded to the substrate. In addition, tip wear is often a problem in a contact mode [191,192].

In non-contact AFM (NC-AFM) mode, the spacing between the tip and the sample surface is in the order of several to tens of nanometers. A stiff cantilever is excited to vibration near its resonance frequency by an additional piezo element. The frequency alternation of the oscillating cantilever is utilized to detect changes in the force gradient, which reveal changes in the distance between the tip and the sample, and thus, sample topography. The feedback system keeps the resonance frequency constant by changing the height of the scanner. As in the contact mode, the voltage applied to the scanner is used to generate the image of surface topography. Because the tip does not touch the sample during the measurement, lateral forces and surface/tip damage are minimized [193].

In the tapping or intermittent contact mode, the oscillating tip during scanning alternately touches the surface and lifts off with an amplitude of 10–100 nm. Energy losses due to intermittent contact of the tip with the surface cause a change in the oscillation amplitude. The feedback system keeps the oscillation amplitude constant by changing the voltage regulating the height of the scanner, and the latter gives topographic information of the sample surface [192].

2.6.1. AFM imaging of graphene

Atomic force microscopy was the first technique used to identify SLG [56]. After the micromechanical exfoliation technique was employed, there was a need to select SLG from thin graphitic flakes and FLG for further experiments. The thinnest flakes were first identified by optical or scanning electron microscopy and further measured by AFM. The relevant thickness, as well as the absence of atomic steps within the flake, affirmed their two-dimensional nature. At this time, AFM was the only method to reliably identify single-layer crystals prior to the measurements of their properties [194].

The AFM approach for estimation of the number of graphene layers seems very straightforward. However, several factors can affect the accuracy of the measurement. Graphene, especially the one produced by exfoliation methods, may not lay flat on the substrate. Furthermore, even when the spacing between the layers in graphite is well known, then the distance between graphene and the substrate can be obscure. The comparison of the AFM measurements of the same area in ambient air and UHV showed more than twofold difference in graphene thickness [195]. The discrepancy between the ambient/vacuum measurements was attributed to the presence of ambient species between the substrate and graphene [195]. Obraztsova et al. have measured the thicknesses of graphene flakes in contact mode and observed that the measured values depended on the force applied by the AFM probe [196]. Apparently, the flakes that were not attached firmly to the substrate were pushed closer by the AFM probe. So, for the correct thickness measurement, the right amount of force between the probe and the substrate needed to be found. The tapping mode is also widely employed for the imaging of graphene. It has been shown, however, that for graphene thickness measurements, the imaging parameters should be chosen with care [197]. The

difference as much as 1 nm can be observed in the measured height depending on the free amplitude of the tapping cantilever and the amplitude setpoint. The difference in height comes from the fact that the tip enters the repulsive region on graphene and oxide surface at different free amplitude. Therefore, for correct thickness measurement, either the free amplitude or setpoint should be chosen in such a way that the measurements are performed in the repulsive region on both oxide and graphene surfaces [197]. If the thickness is measured on the step height relative to another graphene/graphite surface, the measured value is reliable despite the free amplitude or setpoint parameters [197].

The thickness evaluation of graphene is generally performed on a Si/SiO_2 substrate. The thickness measurement of CVD synthesized graphene directly on the catalyst is difficult due to its unevenness and because the oxide layer might start to develop on the uncovered areas of the metal. If the graphene coverage is continuous over the substrate, it will not be possible to estimate the number of the graphene layers with AFM.

Besides thickness determination, AFM is used to study the nanoscale morphology and atomic structure of graphene. Atomic resolution on graphene is more commonly obtained by scanning tunneling microscopy. The tunneling current, however, aside from the surface topography is also dependent on the local density of states near the Fermi energy and the local tunneling barrier height. The combination of STM with AFM high-resolution imaging allows separating electronic and topographic effects [198,199].

In addition, the ultimate sensitivity to surface topography makes AFM the primary method to assess the purity of the graphene surface. The residues introduced during graphene exfoliation, transfer or/and the lithographic patterning may have an adverse effect on graphene properties [200,201]. The electrical and mechanical properties of graphene are also considerably affected by the presence of grain boundaries [202]. The grain boundaries cannot be imaged directly by AFM due to tip convolution effects [203]. Nevertheless, AFM can reveal the grain structure of graphene if selective etching of the defects is performed prior to the AFM imaging [203]. The trenches formed on the grain boundaries' sites can be discerned on AFM images.

AFM has a low throughput, which makes it difficult to measure large-area graphene samples. On the other hand, it is highly suitable for imaging of graphene-based nanoelectronic devices, giving a possibility to observe local imperfections and identify areas of malfunction [204]. In the development of graphene-based devices, the formation of a suitable gate insulator is of particular interest. AFM is widely employed for characterization of nucleation, growth, and homogeneity of the ultrathin dielectric films [205–207].

2.7. Transmission electron microscopy

In a transmission electron microscope (TEM), an electron-transparent sample is irradiated with an e-beam of uniform current density [208]. Electrons are generated in an electron gun via thermionic, Schottky, or field emissions. All the emission types use a negatively biased source (cathode), which, except the cold field emission, is heated to high temperatures. The emitted electrons are converged by the gun electrode(s) and form the first image of the source, the crossover. Then they are accelerated down the column to their final kinetic energy by the electric field parallel to the optical axis of the column produced by the grounded anode. The acceleration voltage of conventional instruments is commonly within the range of 60–300 kV. The system of condenser lenses and the upper objective lens then form a parallel electron beam in the plane of a sample. A condenser lens system determines the beam current and controls the beam diameter. The electron-intensity distribution behind the sample is visualized on a fluorescent screen using a lens system composed of lower objective, intermediate and projection lenses. The lower objective lens produces a magnified real image of the sample. The objective lens is followed by the intermediate lens, which is used to magnify the image formed in the image plane of the objective lens or the diffraction pattern formed in the former's back focal plane. The switching between image and diffraction mode is performed by changing the excitation of the intermediate lens. The projector lens/lenses project the image or diffraction pattern further on the TEM screen. The fluorescent screen is used for real-time imaging and electron optical system adjustments. The image can also be viewed and recorded digitally via a charge-coupled device (CCD) camera coupled with a fiber-optic plate to a fluorescent screen [176,208].

The sample for the characterization using TEM should be sufficiently thin to be transparent to the beam electrons. As electrons interact strongly with matter, the sample thickness must be on the order of 20–100 nm depending on the density and average atomic number of the object and the required resolution. If the sample is thin enough, then almost all of the incoming electrons are transmitted through the specimen. During propagation through the sample, the electron wave can change both its amplitude and its phase. The change in amplitude and a phase generate amplitude (scattering) and phase contrasts, respectively. Generally, both types of contrasts are present in the image; however, the imaging conditions are selected so that one type of contrast is predominant [176,209].

There are two major types of amplitude (scattering) contrast: mass-thickness and diffraction contrasts. Mass-thickness one stems from the incoherent elastic scattering of electrons. As the elastic scattering cross-section depends on the atomic number, the regions of a sample with different atomic numbers scatter a different number of electrons. Similarly, the thickness variation produces contrast because the thicker is the region, the higher is the scattering and multi-scattering probability for materials of the same average atomic number. To obtain interpretable amplitude contrast in the image, either direct or scattered e-beam is selected by the objective aperture. Although nearly all materials show some mass-

thickness contrast, it is the most useful contrast mechanism in the case of non-crystalline materials. If the sample is crystalline, a diffraction contrast can be observed. Diffraction contrast is a special form of amplitude contrast where the scattering occurs at Bragg angles [209]. In order to form a diffraction contrast image, the direct beam (Bright-field image) or a Bragg-scattered beam (Dark-field image) can be selected. The diffraction contrast on the TEM images looks like a variation of intensity between different grains in the polycrystalline material. The individual grains in the polycrystalline material will, therefore, have a different level of intensity in a TEM image depending on their orientation relative to the incident beam. Crystal defects also can be a source of diffraction contrast, which appears as an intensity variation within an individual grain [176,209].

The contrast in TEM images can also arise due to the change in the phase of the electron waves propagating through a thin sample. The difference in phase leads to interference between the unscattered beam and the diffracted beam. Different beams are brought together by slightly defocusing the objective lens. Unlike amplitude contrast imaging where the single beam is selected with an objective aperture, no objective or a large diameter objective aperture is inserted to enable several beams to take part in the formation of the image. Due to its sensitivity, the phase contrast can be used to obtain the atomic resolution, or more precisely atomic column resolution because in the high-resolution image atomic columns through the specimen thickness are visualized [176,209].

The electrons can come through the sample without losing energy or may suffer inelastic interactions. If to measure the amount of energy loss of inelastically scattered electrons, the information about the structure and composition of the sample with a lateral resolution on the atomic level, in the favorable cases, can be obtained. The energy of the electrons that have come through the sample can be measured in a TEM by electron energy loss spectrometer (EELS) [176,209].

A further capability of modern TEM instruments is the formation of a fine highly focused electron probe, which is scanned over the sample in a raster pattern similarly as in an SEM. In scanning transmission electron microscopy (STEM) mode for bright field (BF) image formation, the BF detector is inserted into the axis of the microscope to pick up the unscattered probe electrons. For the dark field (DF) imaging, the annular dark field detector (ADF) is employed. The ADF detector surrounds the unscattered probe electrons and collects only scattered electrons. Another annular detector that sits around the ADF can be used to detect electrons scattered to high angles exclusively for high-angle annular dark field (HAADF) imaging, which allows observing atomic number contrast with high-resolution [209]. The primary advantage of STEM over TEM is a possibility to perform electron probe microanalysis and electron energy loss spectroscopy with significantly higher spatial resolution. The atomic resolution has been reported for X-ray and EELS microanalyses in an analytical STEM [210].

2.7.1. (S)TEM studies of graphene

TEM is a valuable technique for graphene study. The capability of atomic resolution by TEM is used for the determination of the number of graphene layers. In contrast to other methods employed to estimate the number of graphene layers, TEM provides the number of layers by direct visualization and therefore can be considered as the most reliable one. The number of layers can be determined from the image of a cross-section or by observing edges or folds in case of free-standing graphene sheets [211–213]. A folded SLG sheet, which is locally parallel to the electron beam, appears on a bright-field TEM image as one dark line. The folded bilayer graphene appears as two parallel dark lines, similar to the double-walled carbon nanotube. Accordingly, the graphene sheet consisting of three graphene layers, will show three dark lines, etc. In addition, the hexagons are observed on atomic-resolution TEM images of SLG flakes even after a tilt to 20 degrees around the axis in their zigzag and armchair directions, while it is not the case for thicker flakes [214].

EELS can also help to identify the SLG. The low-loss EELS spectrum of graphitic structures is characterized by plasmon excitations consisting of π-and σ-plasmons at 6.2 and 26 eV, respectively, both showing distinct bulk and surface modes. In the EELS spectrum of SLG, the π- plasmon occurs at 4.7 eV and the π+σ plasmon at 14.5 eV. Moreover, in single-layer, the π+σ plasmon consists only of the surface mode. However, it should be noted, that this is valid only for clean graphene surface, the contamination layer and dopants on the surface add the out-of-plane component to the π+σ plasmon, which leads to apparent peak shift, and a general increase in intensity above 14.5 eV [215].

EELS can also be used to measure the total concentration of dopants in graphene, especially of very light elements like boron [216], which is difficult to analyze by other methods. EELS allows not only identification of impurities but also reveals their bonding characteristics, e.g., the oxidation state of ions [217]. It is possible to gain even more information on interstitial atoms and impurities in graphene by combining EELS with an aberration-corrected annular dark-field scanning transmission electron microscopy (ADF-STEM) imaging [218]. In ADF-STEM angstrom-scale electron beam is scanned over the sample while the medium-to-high angle scattered electrons are collected. The ADF-STEM combined with EELS allows doing site-specific single-atom spectroscopy [217,219]. HAADF mode has also been used for detecting foreign atoms within the graphene sheet [220]. In this mode, the annular dark field image is formed only by very high-angle incoherently scattered electrons. The scattering probability has a strong dependence on the atomic number, and therefore it is possible to see atomic contrast on HAADF images, which makes them ideally suitable for visualization of adsorbates [221] or substitutional atoms [220] in a graphene sheet.

The analysis of electron diffraction patterns can also be used for graphene characterization. Normal incidence electron diffraction pattern of a graphene sheet exhibits the typical sixfold symmetry expected for graphite/graphene. If there are

many families of six-fold symmetric spots in the selected area electron diffraction (SAED) pattern, it indicates that there are several grains of different orientation in that particular area. Twelve-fold periodicity would indicate that there are two main families of grains rotated from one another by 30°. The only weak and diffuse rings in the SAED pattern indicate the loss of long-range order in the graphene sheets [53,222].

The SLG can be directly distinguished from thicker samples by analyzing nanobeam electron diffraction patterns (the smallest condenser aperture is used to obtain small illumination area) as a function of incidence angle. The SLG has only the zero-order Laue zone, and therefore the intensities in a diffraction pattern vary only weakly and monotonically with an angle between graphene and the incident beam. The bilayer and thicker graphene flakes show a strong variation of the peak intensities with the tilt angle so that the sixfold symmetry remains undisturbed only for normal incidence [53]. Also, it has been shown, that the SLG can be distinguished from the AB-stacked thicker layers already by intensity ratios of the diffraction peaks. In single-layer, the {1100} spots appear to be more intense relative to {2100}, and the opposite is true for thicker flakes [222] (Figure 5).

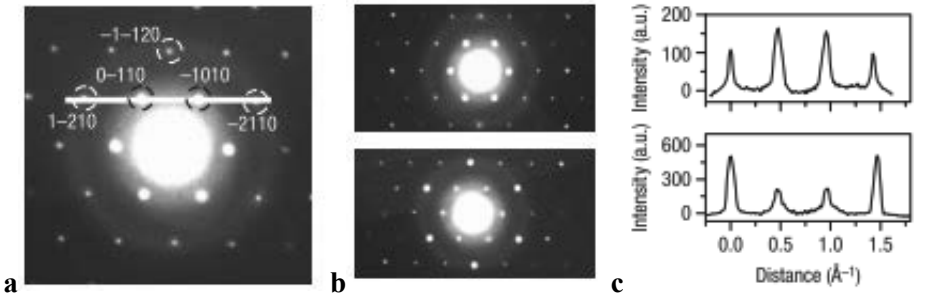

Figure 5. (a) Electron diffraction pattern of graphene with the peaks labeled by Miller–Bravais indices and (b) electron diffraction patterns obtained from SLG (upper) and BLG (lower) with a corresponding diffracted intensity taken along the $1\bar{2}10$ to $\bar{2}110$ axis (c) [63].

Graphene grown by the CVD method is usually polycrystalline. The grain boundaries of graphene can be studied by both TEM and STEM. The images of detailed atomic structure at the grain boundary have been obtained [218,223] revealing how graphene domains coalesce together. To get atomic resolution images of the grain boundaries the aberration-corrected TEM [223] and ADF-STEM [218] have been employed. However, the atomic resolution imaging even of the micrometer-sized graphene membrane is very time-consuming. In order to spot grain boundaries in sufficiently large-area graphene samples, the sample stage can be moved while observing the diffraction pattern [223]. After crossing the tilt grain boundary, the diffraction pattern shows a transition of the diffraction angle. The atomic resolution imaging can then be performed in this particular area. The nano-area parallel electron diffraction in STEM mode [224] can also be

used for grain identification [223]. In this method a quasi-parallel beam (convergent semi-angle < 0.5 mrad) with a diameter of less than 100 nm is scanned over the graphene membrane in the diffraction mode of STEM to detect the transition of a diffraction angle taking place at a tilt grain boundary. For high-throughput grain analysis, dark-field TEM diffraction-sensitive imaging technique can be used [218]. This technique allows determining the size and shapes of the grains as well as their relative angular orientation. For the grain imaging by dark-field TEM, an aperture is placed in the diffraction plane to filter electrons diffracted through only a small range of angles. The resulting image thus shows the grains corresponding to only this selected in-plane orientation. Using several different aperture-locations and color-coding one can create a false-color DF-image overlay revealing shape and orientation of the grains in the region of interest.

Besides grain boundaries, other imperfections of the sp^2-bonded carbon network can be revealed through atomic-level TEM imaging. In contrast to Raman spectroscopy, which can provide information about the crystallinity of the sample and the number of defects, TEM and STEM allow also studying single defects and clarify their exact nature. Stone-Wales defects, single and multiple vacancies, substitutional impurities, foreign adatoms, as well as defects at the edge of graphene sheet have been experimentally observed in graphene samples using TEM and STEM [225]. The electron irradiation itself, however, can introduce various types of structural defects in graphene. So, the sample might not be stable under the beam during the time needed to acquire an image. Two main transformation mechanisms observed in graphene lattice as a result of electron irradiation are atom ejection and bond rotation [226]. To avoid the displacement of carbon atoms the electron beam energy higher than 80 keV should not be used for graphene imaging, as the knock-on damage begins at a few keV above 80 keV [227]. The bond rotation requires less energy than a knock-on displacement. As a consequence, the formation of single and multiple Stone-Wales defects can be observed already at 80 keV [228]. In addition to Stone-Wales defects, the formation of extended holes has been observed in graphene at low beam energies [227]. The formation of holes at electron beam energy below the threshold for displacing atoms is associated with beam-induced etching due to residual oxygen or water in the microscope chamber and is prominent for contaminated samples/areas [227]. Thus, in addition to the requirement for low beam energies, the purity of a graphene sample is highly necessary for successful graphene TEM/STEM studies.

2.8. Raman spectroscopy

Raman spectroscopy is an optical technique based on the registration of inelastic scattering of primary photons illuminating the sample due to their interaction with the phonons existing/generated in the sample [229]. The latter is a molecule, crystal or other condensed matter that is further named as a system. During the interaction process, the primary photon is absorbed, and an electron of the system is excited into a higher energetic level (Figure 6). If the energy of the primary

photon is not enough to excite the electron into a higher stable electron level, as it is usually in case of the conventional (non-resonant) Raman spectroscopy, the electron is excited to a 'virtual state', the level of which is beneath this higher stable electronic level. As the virtual state is not stable, having an extremely small lifetime, the electron quickly leaves the level, generating a scattered photon, and the system returns to the stationary state. With high probability in the photon scattering process, the electron is excited from an electronic ground level and after the process returns to the same level – this is the Rayleigh scattering process. There is also tiny but a finite probability that during the interaction process, the absorbed primary photon excites an electron from a phonon level, and after the virtual state relaxation falls to ground state, or in the other case, the electron is excited from the ground state and after the virtual state relaxation it falls into a phonon level. In the first case, the scattered photon has lower energy than the primary photon, giving in the Raman spectrum the Stokes band, and in the second case, it has higher energy giving the anti-Stokes band. If the system has several phonon levels, several Stokes and anti-Stokes bands appear in the spectrum located symmetrically to both sides from the Rayleigh band. The phonon levels' energy and their population depend not only on the system structure but also on the temperature. From the other hand, the photon scattering process is dependent on the primary photon energy – thus, the Raman spectrum of a system is dependent on both of these parameters [230].

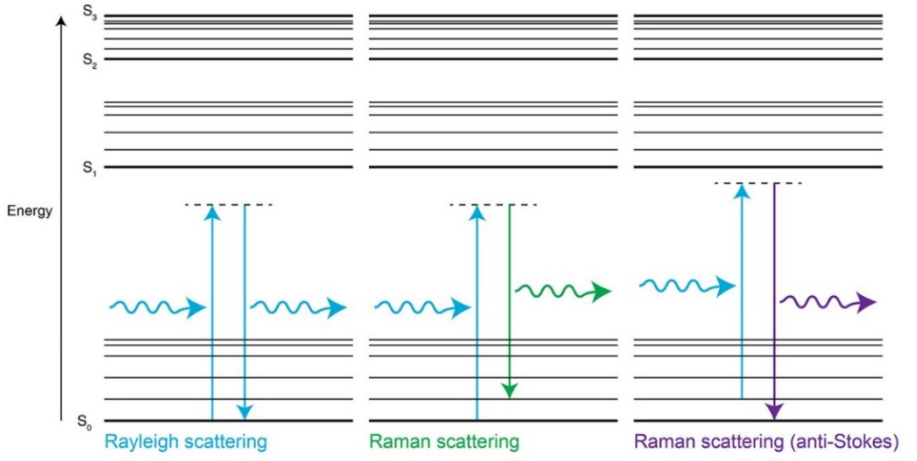

Figure 6. Diagram showing basic processes involved in Rayleigh and Raman scattering. S0 represents the ground electronic state with vibrational energy levels, and S1, S2, S3 represent excited electronic states with vibrational energy levels [231].

In an experiment, a sample is irradiated with a laser beam with a wavelength in the ultraviolet (UV), visible (Vis) or near-infrared (NIR) region. The light scattered from the sample is collected with a lens, e.g., with an objective lens of an optical microscope, and passes through an optical filter, which transmits Raman scattering

signal and blocks Rayleigh scatter – a notch filter. The filtered signal is then focused into the entrance slit of a monochromator, which separates Raman scattered photons with different energies. The light is then directed to a sensitive sensor, a cooled charge coupled device [232].

2.8.1. Raman spectroscopy of graphene

Raman spectroscopy is a widely used method for characterization of carbonaceous materials. It allows one to distinguish between amorphous carbon, graphite, diamond, fullerene, SWCNT, and graphene [233,234]. Combining surface sensitivity and non-destructiveness with high speed of analysis Raman spectroscopy has become one of the essential techniques in graphene studies. Raman spectrum of graphene provides information on the number of graphene layers [211], structural disorder [235], strain [236], doping [237], interlayer coupling [238,239] and the stacking order [240,241] of the layers in FLG.

Similar to graphite, the Raman spectrum of graphene shows two major features (Figure 7a): the G band at ~ 1580 cm^{-1} and the 2D band (historically called G') at ~2700 cm^{-1} [211]. The G band corresponds to a doubly degenerate phonon mode (E_{2g} symmetry) at the center of Brillouin zone [242] and is related to carbon-carbon stretching motion in the sixfold ring of graphene. The 2D band is an overtone of D band at ~1350 cm^{-1}, related to breathing mode of aromatic rings (A_{1g} symmetry). The origin of both D and the 2D modes is a double resonance Raman process. For the D band, the process involves one elastic scattering event by the lattice defects and one inelastic scattering event with emission or absorption of a phonon. Thus the D band appears in the graphene spectrum only in the presence of defects. In case of the 2D band, both scattering events are inelastic, and two phonons with opposite wave vectors are involved. Therefore the 2D band is always present regardless of the presence of defects [229,242].

The shape and intensity of the 2D band relative to the G band allow distinguishing graphene from graphite and FLG [211]. In SLG the 2D band is sharp and can be fitted with one Lorentzian peak (FWHM of ~ 24 cm^{-1}), it is roughly 2–4 times higher intensity than the G band. In BLG, the 2D band is different from both graphene and graphite. It consists of 4 components: the $2D_{1b}$, the $2D_{1A}$, the $2D_{2A}$, the $2D_{2B}$, where the $2D_{1A}$ and the $2D_{2A}$ components have a higher intensity than the $2D_{1b}$ and the $2D_{2B}$ components [243]. With the increasing number of layers, the relative intensity (weight) of the components changes affecting the shape of the 2D band (Figure 7b). The splitting between two most intense components increases with the number of layers from ~ 19 cm^{-1} (BLG) up to ~ 44 cm^{-1} (HOPG) and can be used to estimate the number of layers in several-layer thick graphene samples with AB-stacking [244]. With an increasing number of layers, the shape of the 2D band becomes asymmetric exhibiting typical graphite shoulder at the high-frequency side of the 2D band. When the number of graphene layers is about 10, the Raman spectrum becomes almost identical to that of graphite (Figure 7b).

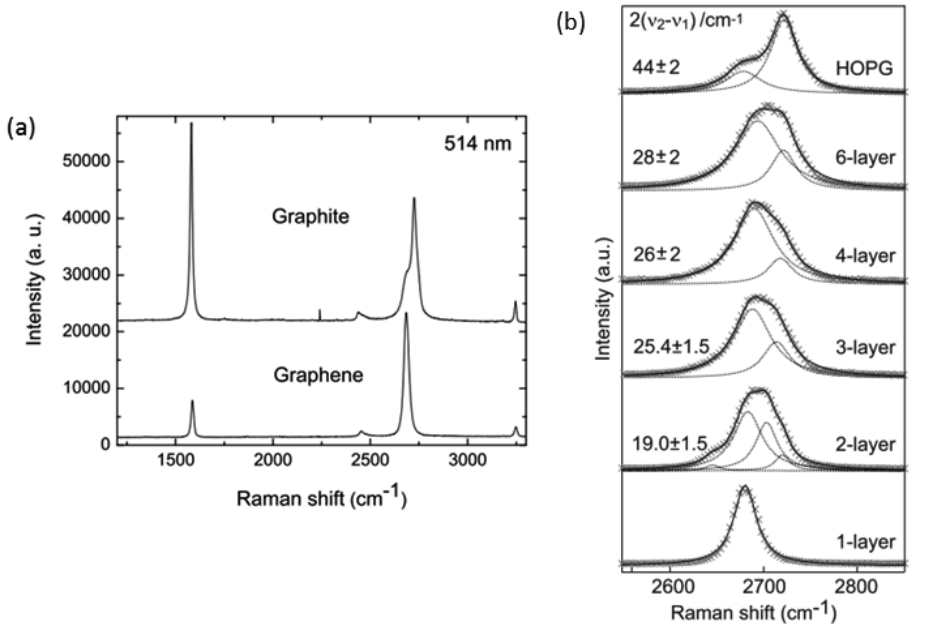

Figure 7. Raman spectra of graphite and graphene: (a) comparison of Raman spectra at 514 nm excitation for bulk graphite and graphene; the spectra are normalized by the intensity of the 2D bands at ~2700 cm^{-1} [211]; (b) change in the shape of the 2D band depending on the number of graphene layers, shown on right side. On the left side are given the values for the separation of the Lorentzian sub-peaks (in case of a BLG, two sub-peaks with the highest intensity) used for fitting the experimental data [244].

The shape of the 2D band is considered the most applicable criterion of Raman spectrum to identify SLG [245]. The intensity ratio of the 2D band to the G band as well as the position of these bands are not reliable signatures for layer number counting, as both are also affected by doping. The first of them depends on the electron concentration [245]. In highly doped graphene the ratio can even drop below 1. The origin of doping in graphene is often metallic contact in a device or substrate used, the contamination during graphene transfer, and adsorbates [237]. Along with the ratio, I(2D)/I(G) decrease in doped graphene, the sharpening and significant shift to higher wavenumbers of G band are observed [237]. The position of the 2D band can significantly change at high doping levels, but in contrast to G band, it shifts to lower wavenumbers with increasing electron concentration in graphene. Thus, the position of the 2D band can help to distinguish between acceptor- and donor-doped graphene samples [245].

The shift of G and the 2D bands can also be a result of strain. Usually both bands redshift under tensile stress [236,246] and blueshift under compression [247,248]. In case of uniaxial strain, broadening or even splitting of G band [236,249] and the 2D band [250] has been observed because of the strain-induced breaking of the crystal symmetry and the change of phonon wave vector due to

relative movement of the Dirac cones [229]. For biaxial strain, no splitting is observed.

In addition, Raman spectroscopy is very sensitive to the structural disorder in graphene samples. The estimated extent of disorder in graphene allows drawing conclusions about the graphene quality and its further performance in graphene-based devices as the structural damage affects graphene properties. The first sign of the structural disorder is a presence of the D band in the Raman spectrum of graphene. The D band is absent in the graphene samples with high crystalline quality [251]. In the near vicinity of defects, the D band scattering process is activated, and it appears in the spectrum [229]. As the D band is defect-activated, its intensity increases with the number of defects. On the contrary, the intensity of G and the 2D band decreases. The intensities of all Raman peaks, however, also depend on measurement conditions. Therefore, to estimate structural disorder, it is convenient to use the height (or area) ratio of the D band to the G band [252]. The increase of I(D)/I(G) designates the transition from graphene to the nano-crystalline graphene. However, when the defect density becomes so high that the disorganization of the hexagonal network starts to take place, the ratio I(D)/I(G) decreases again as the number of 6-fold rings becomes smaller. Fortunately, there are other Raman signatures of graphene structural damage. As disorder increases, the bands become broader compared to the bands in pristine graphene. The broadening becomes especially prominent when the distance between defects becomes smaller than ~ 4 nm. At this stage, the G band and another lower intensity defect-activated band (D') merge forming broadband at about 1600 cm^{-1}. The further amorphization to predominantly sp^2-hybridized carbon is characterized by the redshift of the G band and vanishing of the well-defined 2D band [229,253].

In the FLG and MLG in addition to in-plane vibrations, modes originating from the relative motion of the planes itself appear. Depending on whether the planes are moving perpendicular or parallel to their normal, the shear (C) and the layer breathing modes (LBMs or ZO') are distinguished [229]. The position of C band varies depending on the number of graphene layers from ~ 31 cm^{-1} in BLG up to ~ 43 cm^{-1} in graphite [254]. The C band has a low intensity, and its frequency is below the notch and edge filter cut-off of most Raman spectrometers. The latter limits utilization of the C band for the counting of graphene layers. The direct observation of the LBMs in graphene is also challenging for the same reasons. However, the two-phonon overtones [239] and the combinations of LBMs with in-plane longitudinal optical mode phonon (LOZO') [255] have been observed in the range of 80–300 cm^{-1} and around 1720 cm^{-1}, respectively. The LOZO' mode Raman band has been found to exhibit a different line shape depending on the number of layers in FLG, and whether the layers are ABA or ABC stacked [255].

In addition to ABA and ABC stacking, the graphene layers in FLG and MLG can have unconventional stacking order, where the layers are rotated relative to each other by an arbitrary angle [256]. Raman spectrum of this misoriented (or twisted) graphene contains besides beforementioned spectral bands also

additional non-dispersive Raman modes, appearing on the high-energy side of the intense G band (R') and below G band (R). These bands emerge due to the scattering of phonons with finite wavevectors, activated by involving angle-dependent wavevectors of a formed superlattice [257]. The exact position of the R band is distinctly dependent on the twisting angle between the graphene layers [258,259]. The R′ band appears in the spectrum at low twisting angles of the layers, and its frequency also has weak angle dependence [260].

2.9. Graphene-based structures and their applications

2.9.1. Atomic layer deposition on graphene

Atomic layer deposition (ALD) is a well-developed method for deposition of high-k dielectric films. The advantages of ALD are excellent conformity even on surfaces with a complex topology (like channels, pores, cracks, fibers, particles, etc.), the possibility to control the thickness and composition with high accuracy, as well as a large variety of different materials that can be deposited and the ability to obtain relatively high quality films at low growth temperatures [261]. The inherent to ALD thickness and composition control down to the atomic level makes it an ideal deposition technique to grow atomically thin films. Besides, in the ALD process, the surface is not bombarded with energetic particles, which allows avoiding the damage of the substrate surface.

During the deposition of a thin film using the ALD method, reactive precursor chemicals, each containing different elements of the deposited material, are conducted to the reaction zone, i.e., the surface of the substrate, separately. This allows preventing unwanted gas-phase reactions, and the atomic level control of the deposited thin film becomes possible [262]. One full ALD cycle is illustrated in Figure 8. In this example, HfO_2 is synthesized from $HfCl_4$ and H_2O. Initially, a pulse of $HfCl_4$ is introduced into the flowing inert carrier gas, and Hf-containing monolayer is formed on the substrate surface through a self-saturating reaction. Excess $HfCl_4$ is removed during a short purge period when only the inert carrier gas is flowing. Then, the H_2O pulse is introduced, and it reacts with the Hf-containing layer on the substrate producing a monolayer of HfO_2 or a part of it. The ALD cycle is completed with a second purge period to remove the unreacted H_2O and the reaction by-products. Usually, several ALD cycles are needed to deposit a monolayer onto the substrate. The ALD cycle is repeated until the desired film thickness is achieved [262].

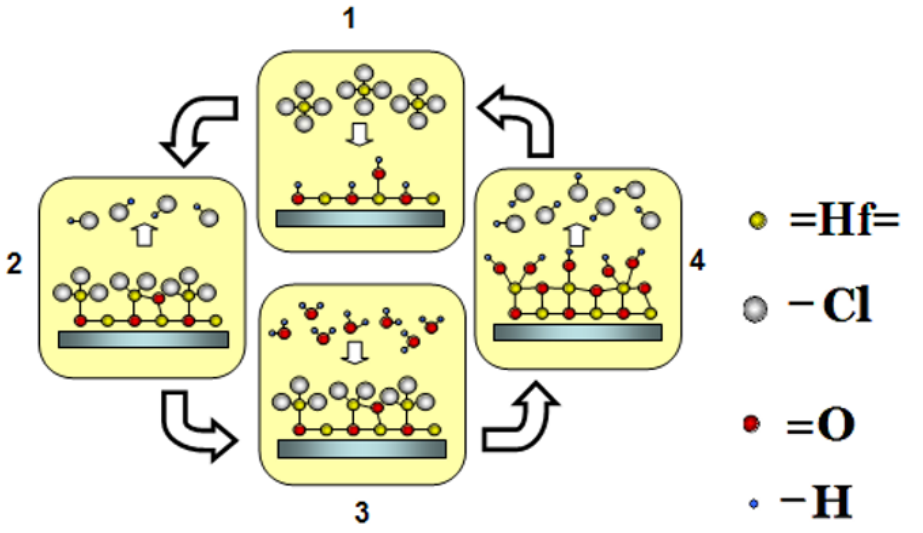

Figure 8. Schematic illustration of one ALD cycle.

The main concern of ALD on graphene is the absence of proper reaction centers for ALD precursors due to the inertness of the graphene surface. Xuan et al. have shown that conventional atomic layer deposition of metal oxides on HOPG substrate results in oxide nanoribbons at HOPGs step edges, not a continuous film [205]. In contrast to defect-free terraces, the step edges with dangling carbon bonds provide initial reaction sites for the ALD process. In order to obtain uniform oxide film, the functionalization of graphene surface can be performed [263]. Graphene functionalization aims to create evenly distributed functional groups on the graphene surface, which will serve as nucleation sites for the ALD process. As graphene can be viewed as an unrolled carbon nanotube, the methods developed for the functionalization of carbon nanotubes can also be implemented for graphene functionalization. The functionalization of CNT, as well as graphene, can be divided into covalent and noncovalent functionalization. The covalent functionalization requires highly reactive chemicals. A very high degree of functionalization can be generated upon the reduction of the aryldiazonium salt [264]. Farmer et al. achieved conformal ALD on SWCNT functionalized using the reaction with *in-situ* synthesized diazonium compounds from aniline precursor [265]. The formation of a covalent bond with functionalized groups results in the change of hybridization state of carbon atoms from sp^2 to sp^3. The latter affects the electronic properties of the system significantly [265,266].

The noncovalent functionalization allows avoiding the degradation of the sp^2 hybridized structure. The noncovalent functionalization method of CNT has been demonstrated by Lu and coworkers, who used the adsorption of poly-T-DNA molecules to supply functional groups of sufficient density and stability for uniform HfO_2 growth by ALD. Apparently, free hydroxyl groups and phosphate groups of the DNA molecule react with ALD precursors initiating the ALD

process. Remarkably, no degradation in the CNT conductance was observed after its functionalization with DNA molecules and subsequent ALD [267]. However, the functionalization mentioned above was employed for the ALD process conducted at 90 ºC and may not be suitable for deposition temperatures utilized in most of ALD processes.

The noncovalent functionalization of CNT before the ALD process has also been performed using pretreatment with sodium dodecyl sulfate (SDS) in D_2O [268]. The hydrophobic surface of the CNT attracts the hydrophobic long-chain hydrocarbon tail of the SDS molecule, whereas hydrophilic sulfate head groups serve as nucleation sites for ALD precursors leading to conformal Al_2O_3 coating.

Another noncovalent functionalization method of SWCNT was realized in [269] using alternating exposures of nitrogen dioxide (NO_2) and trimethylaluminum (TMA) vapor. During the NO_2 pulse, the NO_2 molecules adsorb on the surface of nanotubes serving further as adsorption centers for TMA molecules. The adsorbed TMA molecules after subsequent TMA pulse, in turn, prevent desorption of NO_2 molecules as well as the further attachment of both NO_2 and TMA molecules. The NO_2-TMA monolayer on the surface of the nanotubes facilitated the nucleation of Al_2O_3 oxide layer deposited using ALD from TMA and water precursors. The same functionalization recipe has also been applied for the functionalization of graphene [270]. With the help of the functionalization layer, the authors succeeded in the fabrication of graphene top-gated device. The estimated charge carrier mobility of graphene in the prepared device was reasonable, about 7000 $cm^2/V \cdot s$.

The treatment of graphene in perylenetetracarboxylic acid solution before the ALD has also been shown to significantly improve the quality of the deposited oxide layer [263]. The perylenetetracarboxylic acid presumably attaches to graphene via π–π stacking, and therefore hydrophobic forces did not introduce defects into graphene lattice. Lee et al. [271] have combined the functionalization of the HOPG surface with an ALD process by using ozone instead of water as an oxygen precursor for depositing Al_2O_3. As a result, a smooth and uniform oxide layer was achieved. The ozone treatment is known to produce oxygen-containing functional groups on the graphitic surface [272], which serve as nucleation centers for Al_2O_3 growth. However, the ozone treatment has been shown to cause considerable damage to the conjugated π-bonding of the carbon nanotubes [273].

The treatment of the graphitic material with concentrated hydrochloric acid is a simple, low-cost and readily available method to improve the nucleation and growth of the oxide film [274]. But, the hydrochloric acid induces bond cleavage in the carbon network [275], which adversely affects conductivity and charge carrier mobility in graphene.

The alternative approach to creating the nucleation centers on the graphene surface has been proposed by Kim et al. [276]. In this approach, a 1 – 2 nm thick Al buffer layer was deposited by electron beam evaporation to graphene before the Al_2O_3 deposition by ALD. Once exposed to the air, the surface of the aluminum layer is oxidized and can serve as a nucleation layer to promote the conformal growth of the top-gate dielectric. The authors believe that the suggested method

allows minimizing the carrier mobility degradation associated with the deposition of the dielectric layer on graphene.

2.9.2. Graphene-based electrodes for electrochemical applications

Carbon materials are today widely studied for the use in electrochemical applications, especially in energetics. For instance, it has been proposed that graphene should be a competitive electrode material for energy storage applications, like electrochemical double-layer capacitors (EDLCs) [277,278] or metal-ion (Li^+, Na^+, Al^{3+}) batteries [279–281]. Since the energy in EDLCs is stored through the adsorption of ions on the surface of the electrodes, the exceptionally high specific surface area of graphene made it very attractive for utilization in EDLCs [282]. It was reported that if the whole graphene surface area is utilized, the electric double-layer capacitance of 550 Fg^{-1} can be achieved [283]. The latter is a higher value than can be obtained by employing other highly researched materials for application in supercapacitors, such as activated carbon or CNTs. Also, the higher electrical conductivity of graphene, compared to activated carbon, is beneficial for the fabrication of high power density supercapacitors [34]. In practice, however, it is challenging to fabricate graphene electrode with the very high surface area due to re-stacking and agglomeration of graphene sheets [26]. In order to achieve better distribution of the graphene sheets for getting better ion accessibility, various strategies have been reported from the deposition of the graphene on porous substrates [284] to the chemical modification [285] or intercalation with other nanomaterials, like CNTs [286,287] and nanoparticles [288,289]. Making hybrids of the graphene with pseudo-capacitor materials, such as transition metal oxides and polymers, is another promising approach to increase supercapacitors performance [290].

Lithium-ion based rechargeable batteries are another class of energy storage devices where the graphene implementation has shown a potential [26]. Like graphite, graphene can be used as an anode for hosting lithium ions [282]. Currently, the reported graphene-based lithium-ion batteries (LIBs) mostly utilize rGO, graphene nanosheets or graphene paper [26]. Larger spacing between randomly arranged graphene layers compared to graphite allows accommodating a larger number of lithium ions leading to an increase in electrode capacity [279]. A large amount of edges and defects in these materials is also associated with an increased capacity [291]. Also, it is believed that nanopores within graphene-based anode positively influence the diffusion of Li ions [292]. Furthermore, graphene's mechanical properties are highly desirable for the development of flexible LIBs [282]. Still, the oxygen-containing groups present on graphene obtained by wet-chemical methods, which on the one hand prevent the restacking of graphene sheets, but on the other hand can react with Li ions leading to the dramatic decrease of the initially high electrode capacity [293]. The Li-storage on defects and edges has also been shown to hurt the performance of the battery[294] In order to improve the performance of the anodes made from bare

graphene, graphene composites with metal oxides have recently been proposed [295,296]. Besides metal oxide/graphene composites, it has been shown that combining graphene with organic molecules also gives an enhancement in the performance of the electrode [297]. There is also a growing number of reports exploring graphene implementation in the cathode system of LiBs. The use of graphene is primarily aimed to improve the electrical conductivity of the cathode material without the substantially increasing its mass [298,299]. Among the effects of graphene implementation on cathode performance are faster charging mainly due to improved electron transfer [300–302] and better stability as a result of preventing adverse reactions on the cathode surface [301].

In addition to energy storage, graphene has been reported to be utilized in energy generation devices, such as proton exchange membrane fuel cells (PEMFCs), including methanol fuel cells (DMFCs), direct formic acid fuel cells (DFAFCs), etc. [303]. Like other carbon allotropes graphene is mainly utilized in the fuel cells as catalyst support [26]. At present, the most commonly used support for accomplishing electrocatalyst nanoparticles in low-temperature fuel cells is carbon black (CB), such as Vulcan XC-72R or Denka Black [304,305]. Despite wide utilization, CB suffers from drawbacks such as the organosulfur impurities, mass transfer limitations due to its dense structure and poor corrosion resistance under the fuel cell operating conditions [304]. It is known, however, that carbon materials with higher graphitization degree are more corrosion resistant [306]. Thus, the substitution of carbon black with graphene sheets would lead to improved durability of the fuel cell. The higher degree of graphitization has also been associated with a stronger interaction between carbon support and metal catalyst [304]. The strengthened interaction with the support contributes to the increased stability of the catalyst [26]. Also, the better dispersion of platinum and a reduction of its cluster size was observed on graphene-based catalysts for fuel cell applications [307]. The improved dispersion of the catalysts can also be due to the surface functional groups introduced during the preparation of graphene sheets by chemical methods. These graphene surface groups, presumably, help to “bind” and thus, stabilize catalyst particles on graphene’s surface, hence preventing their aggregation [26]. Besides, graphene in comparison to carbon black has a significantly higher surface area and electron conductivity, which hold promise for fabrication of the fuel cell with improved performance.

The prospect for enhanced fuel cell catalysts through the employment of graphene as a support has been actively examined by preparing graphene-metal particle nanocomposites [26]. Pt nanoparticles synthesized on reduced graphene oxide showed much higher electrochemically active surface area and catalytic activity toward oxygen reduction reaction (ORR) compared to commercial Pt/CB catalyst [308]. In another work, Pt/graphene catalyst synthesized via simultaneous reduction of Pt precursor and graphene oxide suspension revealed higher catalytic activity for both methanol oxidation and ORR in comparison with platinum supported on CB [309]. Dong et al. investigated the electrocatalytic activity for methanol and ethanol oxidation of Pt-Ru nanoparticles synthesized on graphene sheets and found the enhanced efficiency of a prepared catalyst in comparison to

widely-used Vulcan XC-72R carbon black supported catalysts [310]. Another study also reported the remarkably high activity of Pt/GNS for methanol oxidation reaction in comparison to Pt/CB catalyst [311]. In addition to the enhanced catalytic activity, the much higher stability of the graphene supported noble metal catalysts has been also reported [312].

Furthermore, it has been found that nitrogen-doped graphene could act as effective metal-free electrocatalysts for ORR. In a report by Qu et al. nitrogen-doped graphene synthesized by chemical vapor deposition in the presence of ammonia showed much better electrocatalytic activity and better operation stability over time than platinum in alkaline fuel cell [313]. The work by Shao et al. has demonstrated higher electrocatalytic activity, durability and selectivity of nitrogen-doped rGO compared to Pt for ORR [314]. The replacement of expensive noble metal-based electrocatalysts with metal-free durable and efficient catalysts would be a significant advance in fuel cell technology.

Another strategy to develop graphene-based metal-free electrocatalyst is through the modification of graphene surface by specific molecules [25]. For instance, tridodecylmethylammoniumchloride-functionalized rGO showed enhanced electrocatalytic activity toward ORR [315]. Wang et al. [316] used another quaternary ammonium compound to modify the graphene surface through intermolecular charge-transfer that creates a net positive charge on carbon atoms. The resultant functionalized graphene possessed dramatically enhanced electrocatalytic activities toward ORR compared to unmodified graphene, and its stability was even superior to the commercial Pt/C catalyst. Such a strategy of "molecular doping" has the benefits of low energy consumption and compatibility with large-scale production. Moreover, attached groups allow the addition of extra functionalities and thereby broaden up a utility of graphene. For example, graphene functionalized with various functional groups has been utilized within biosensing [317]. Still, more studies are required for better understanding and control over the functionalization process of graphene. One of the aims of this thesis was to investigate the CVD-grown graphene modification with aryl groups by electrochemical reduction of the corresponding diazonium salts.

Before studying the properties of modified graphene electrodes, the electrochemical behavior of the pristine graphene is needed to be addressed. On the other hand, being one layer of graphite graphene might, in principle, show electrochemical behavior similar to HOPG. However, there are reports [28][29] showing that graphene electrodes present faster electron transfer kinetics compared to the basal plane of HOPG. It has been reported, however, that some surfactants used to stabilize the graphene suspensions have measurable electrochemical activity, which can thus be responsible for the electrochemical performance of the stabilized graphene [31]. A similar effect can also have carbonaceous debris, a common by-product of rGO synthesis [30]. Besides, iron residues in graphene prepared from graphite with subsequent reduction can also significantly influence the electrochemistry of graphene [32]. Furthermore, graphene prepared by different methods has highly varied densities of edge plane defects [33]. Considering that at least in case of graphite, the edge sites are the primary source of the electrochemical

activity [34], it is apparent that graphene preparation method influences on its electrochemical behavior. Therefore, it was of interest to study the electrochemical properties of the graphene synthesized by the CVD method on nickel foils. As it was important to exclude any factors that can affect the electrochemical behavior of the graphene, the characterization of the prepared graphene/nickel electrodes by nanoscopic methods was one of the aims of this thesis.

3. RESEARCH OBJECTIVES AND STATEMENTS

The main goal of the research was to characterize the surface, structure, and quality of pristine and functionalized FLG and MLG sheets prepared by CVD. Their properties had to be compared with properties of single-layer graphene, prepared by exfoliation from natural graphite or synthesized by CVD. The study was addressed to help create new industrial and energetic materials and structures on the basis of the FLG and MLG, which were at the time of studies much less studied than SLG.

To fulfill the goal, the author had to introduce the synthesis of FLG and MLG by CVD using Ni as a catalytic substrate. During the study, both Ni-foils and thin Ni-films had to be explored as substrates, and the CVD process had to be optimized. As compared to SLG, the dedicated synthesis of FLG and MLG growth was at the time of study significantly less researched, especially the stacking of the graphene layers and continuity of the graphene sheet. Thus, special attention had to be devoted to the growth mechanism of FLG and MLG on the Ni-substrates for complete insight on the effects of the catalytic substrate on the graphene formation.

For the characterization of the graphene samples, the author had to explore various high-resolution microscopy (HR-SEM and FIB, HR-TEM, STM) and analysis (EDX, EBSD, XPS, μRaman) methods for their complex study in the nanometric thickness range.

After the synthesis and first characterization, the integration of graphene in real devices often requires further modification of the graphene surface. So graphene, incl. FLG and MLG, functionalized with various functional groups, is a promising material for electrochemical applications in advanced energetics. Despite certain progress in this area, more studies were required for better understanding and control over the functionalization process of graphene. One of the tasks of this thesis was to investigate the CVD-grown MLG modification with aryl groups by electrochemical reduction of the corresponding diazonium salts. Before studying the properties of modified graphene electrodes, also electrochemical behavior of the as-synthesized graphene was needed to be addressed. Since the electrochemical properties of the graphene can differ depending on the graphene preparation method, and can also be affected during graphene transfer procedure, it was of interest to study the electrochemical properties of the CVD-synthesized MLG directly on nickel foils.

The realization of graphene field-effect transistors, one of the most promising graphene application, could require modification of graphene surface through the deposition of the high-k oxide on it to serve as the top-gate. Since the deposition of the high-k oxides, such as hafnium dioxide and zirconium dioxide, has been well established in the Laboratory of Thin Film Technology of the University of Tartu, revealing the feasibility of ALD for producing thin continuous high-k oxide films on the graphene sheets was another task of this study.

Following statements are presented for the defense:

1. Advanced usage of high-temperature CVD, and CH_4 as precursor and Ni-foils or thin films as substrates, can lead to controllable growth of large-area FLG and MLG.
2. Differing stacking order between the graphene layers, which on Ni can coexist not only in neighboring domains but even in the same sample area, can result in Raman spectra of MLG that closely resemble the spectra obtained for SLG. The detailed examination of less intense in-plane and out-of-plane phonon modes of graphene using μRaman spectroscopy/microscopy allows locally to study the stacking order of FLG and MLG and avoid mistakes in the determination of the number of graphene layers.
3. FLG and MLG, as well as SLG, might not be suitable to serve as protective, especially corrosion protective coatings due to difficulties in obtaining large-area continuous graphene sheet on polycrystalline substrates.
4. FLG and MLG can be used to prepare new energetic materials, structures, and devices. For example, FLG and MLG on Ni-foil are good alternatives to more expensive HOPG electrode in electrochemical studies. Also, the graphene sheets can be successfully functionalized, e.g., by attaching, electrochemically active functional groups to their surface with the help of reduction of aryldiazonium salts. As during the functionalization process, only the top graphene layer is affected, the possible adverse effects of the functionalization process on graphene structure and properties are significantly milder in MLG compared to SLG.
5. Thin ceramic coatings deposited onto graphene sheets by low-temperature ALD do not generate additional defects in the sheets but can cause mechanical stresses in the structures.

4. MATERIALS AND METHODS

4.1. Graphene preparation by micromechanical exfoliation

For the preparation of graphene samples on the micrometer scale, the method developed by Novoselov et al. [56] was employed. For micromechanical exfoliation, natural (Madagascar) graphite was used. A small graphite crystal was attached to the Scotch tape and repeatedly peeled by folding the tape around it. When the graphite attached to the Scotch tape became almost transparent, it was gently pressed on Si substrates covered with 300 nm thick SiO_2 layer. As a result, upper layers of graphite were partially transferred to the substrate. The thinnest flakes were then selected under the optical microscope based on their color. The SLG and FLG flakes were identified among the thinnest flakes using AFM and Raman spectroscopy.

4.2. Graphene synthesis on nickel foils

Graphene synthesis was carried out on polycrystalline 25 μm thick Ni foils (99.9%, Strem Chemicals, Inc.) using a low-pressure CVD method in a hot-wall laboratory reactor from methane as a carbon source. The CVD reactor was comprised of a quartz tube (length: ~500 mm, diameter: ~25 mm) placed inside the resistively heated furnace (length: ~300 mm). The temperature of the quartz holder was recorded using a K-type thermocouple. The reactor was equipped with three digital mass-flow controllers (Smart-Trak 2, Sierra Instruments) for gas lines of Ar, 10% CH_4/Ar and H_2. Prior to the growth, the nickel foils were annealed at 1000 °C for 1 hour in a flow of H_2 and Ar gases (both 99.999, AGA Estonia) with flow rates of 125 and 100 sccm, respectively. Then, 140 sccm of 10 % CH_4 in Ar gas (AGA Estonia) was introduced into the reactor for different growth periods. The total pressure in the CVD chamber was maintained at 3 mbar. Finally, the sample was rapidly cooled by moving the furnace away from the sample position (the average cooling rate was 25 °C/min). The CH_4 and Ar/H_2 flows were maintained during the cooling to 200 °C. The same cooling conditions as mentioned above were used for all the samples unless otherwise stated. For comparison, we also performed a slow-cooling process with an average cooling rate of 7 °C/min. First, the sample was cooled down to approximately 700 °C at a rate of 4 °C/min, after that, the furnace was switched off, and the sample was left to cool to room temperature. These cooling conditions are denoted in the text as a “slow-cooling process”.

4.3. Graphene synthesis on nickel films

Nickel films with thicknesses from 60 to 140 nm were prepared by electron beam deposition method at 300 °C onto Si substrates covered with 90 nm-thick SiO_2 film. The thickness and purity of the deposited nickel films has been verified by X-ray fluorescence.

Graphene sheets were grown in the same low pressure, hot-walled CVD reactor in argon flow using methane and hydrogen as precursor gases. Prior to the graphene growth, the Ni-film samples were annealed at 950 °C in a Ar/H_2 atmosphere. On these films, graphene was grown at 900 °C in the flow of a gas mixture containing Ar, H_2, and 10% CH_4/Ar (all 99.999%, AGA). Argon, hydrogen and methane/argon flow rates were the same as during the deposition on Ni foils. Finally, the sample was rapidly cooled by moving the furnace away from the sample position (the average cooling rate was 25 °C/min) using the same flow rates of the gases as during the deposition.

4.4. Graphene synthesis on copper foils

For deposition of predominantly SLG commercial 25-μm thick polycrystalline copper foils (99.999%, Alfa Aesar) were used as substrates. Prior to growth, the foils were annealed during 10 min at 950 °C in Ar/H_2 and then exposed to the mixture of 10% CH_4 in Ar at the same temperature for 30 min. Then the samples were cooled by moving the furnace away from the sample position to the room temperature in Ar flow (average cooling rate was 25 °C/min).

4.5. Graphene transfer

To transfer graphene from nickel and copper substrates, graphene was covered with PMMA protective layer. In order to deposit the protective layer, the metal substrate was spin-coated with a PMMA solution (24 mg/ml) in chlorobenzene. Graphene from the other side of the foil was removed by low-pressure Ar plasma cleaning using plasma cleaner Femto-1 (Diener Electronic GmbH). Then nickel was etched away with a 1M solution of $FeCl_3$ in water. The PMMA/graphene structures were washed in deionized water. Next, graphene/PMMA structures floating on water surface, PMMA layer above, were grabbed from below by Si/SiO_2 substrate. After drying the PMMA was dissolved by dichloromethane (Alfa Aesar). Some MLG samples from nickel foils were also transferred to the TEM grid. The transfer procedure was the same except that the PMMA was removed by the vapor of the hot dichloromethane.

For the graphene transfer from thin nickel films no Ar plasma treatment was required, but otherwise, the procedure was the same as for nickel foils.

4.6. Deposition of HfO_2

The HfO_2 films were deposited from $HfCl_4$ and H_2O in a flow-type low-pressure ALD reactor [318] on micromechanically exfoliated graphene samples. To synthesize HfO_2, an ALD cycle consisting of an $HfCl_4$ pulse (5 s in duration), a purge of the reaction zone with N_2 (2 s), H_2O pulse (2 s) and another purge (5 s) was repeated until a film of required thickness was obtained. $HfCl_4$ was volatilized at a temperature of 140 °C in the flow of N_2 carrier gas. The $HfCl_4$ pulses were formed by changing the flow direction of the carrier gas between the $HfCl_4$ source and reaction zone using a special ALD valve. The H_2O source was kept at the room temperature while the H_2O vapor was led to the reactor through a needle and solenoid valves, which controlled the precursor supply. At the reactor outlet, the partial pressure of H_2O was 5 Pa during an H_2O pulse while the N_2 pressure was approximately 250 Pa during the whole deposition process. For deposition of the films three different temperature regimes of the substrate were used: deposition at 170–180 °C, deposition at 300 °C and deposition in a two-step process (the growth was initiated at 170–180 °C, after 10 ALD cycles the temperature was increased to 300 °C).

4.7. Deposition of ZrO_2

The ZrO_2 films were deposited from $ZrCl_4$ (Aldrich, 99.99%) and H_2O in a flow-type low-pressure ALD reactor [318] using 100 ALD cycles at 190 °C. Each ALD cycle consisted of an $ZrCl_4$ pulse (2 or 5 s), purge with N_2 (2 s), an H_2O pulse (2 or 5 s) and the second purge (5 or 10 s) was repeated until the desired ZrO_2 thickness was achieved. $ZrCl_4$ was volatilized at 145 °C [319] in the carrier gas flow. The source of H_2O was kept at room temperature while the H_2O vapor was conducted to the reactor through the needle and solenoid valves. During the deposition the pressure of the carrier gas (N_2 of 99.999 % purity) in the reaction zone was kept at 200–220 Pa. The partial pressure of H_2O during the H_2O pulse at the reactor outlet was about 6 Pa. The ZrO_2 was simultaneously deposited onto the mass sensor (Figure 9) for quartz crystal microbalance (QCM) studies, graphene-covered Si/SiO_2 substrates and as-synthesized graphene on Ni film and Cu foil.

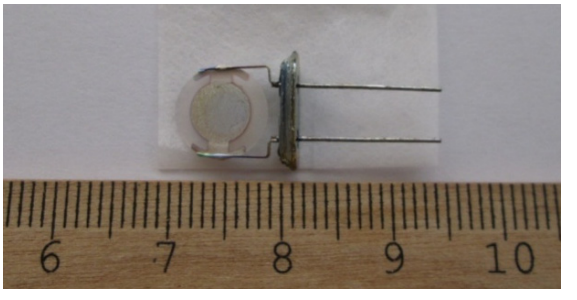

Figure 9. The QCM sensor used [VI].

4.8. Characterization of graphene samples

Raman scattering spectra of the graphene samples were recorded with inVia confocal Raman spectrometer (Renishaw) using a laser excitation wavelength of 514.5 nm (Ar^+ laser) at a relatively low incident power (1–5 mW). A 50× objective lens was used to focus the laser beam to 1–2 μm spot on the sample and to collect the backscattered Raman signal. The signal was recorded with a Peltier-cooled CCD detector. The spectral resolution of the spectrometer was set at 1–2 cm^{-1}.

The SEM studies were conducted using a high-resolution scanning electron microscope (HR-SEM) Helios NanoLab 600 (FEI Company), having a Schottky-type electron emitter. The emitter offers a small source size and high brightness, which allows achieving the SEM high-resolution imaging along with low noise and stability [177]. HR-SEM micrographs were recorded using an acceleration voltage in the range of 2 – 10 kV. The SEM images of the graphene samples were obtained using an Everhart-Thornley detector and also an in-lens detector placed inside the electron column. This immersion lens was used to obtain images of transferred graphene films. Using the immersion lens, where the sample is placed in the magnetic field of the lens allows decreasing the image aberrations and therefore acquiring higher resolution images as well as obtaining higher detection efficiency of secondary electrons and getting better contrast of the images. The immersion lenses were not used for graphene samples on nickel foils due to nickel ferromagnetic nature. The electron probe microanalysis (EPMA) was performed using an energy-dispersive X-ray (EDX) spectrometer INCA Energy 350 (Oxford Instruments), mounted to the same HR-SEM. In addition, the graphene coatings were examined in the transmission mode of the HR-SEM.

The crystallographic orientation of the grains of the nickel substrates was determined by electron backscatter diffraction (EBSD) measurements using another scanning electron microscope (EVO MA 15, Zeiss) equipped with an EBSD detector (Nordlys, Oxford Instruments). The EBSD data were post-processed using the AZtec (Oxford Instruments) and CHANNEL 5 (HKL) software programs. For the EBSD measurements, the accelerating voltage of the primary beam was 20 kV. To enhance the detection sensitivity of the EBSD patterns, the samples were inclined approximately to 70º relative to the electron beam.

The surface morphology of the nickel before and after graphene synthesis was studied using atomic force microscope AutoProbe CP II (Park SI/Veeco), in contact and intermittent contact mode. In addition, the error-signal mode was used for imaging graphene on nickel foils. In this mode, the feedback error signal is used for an image when scanning in Constant Force mode. The feedback loop filters out only the low spatial frequency components, while the high-frequency components are displayed [320]. This allows revealing subtle surface features on relatively rough (from AFM viewpoint) nickel surface. STM measurements of graphene on nickel films were conducted with a SPM measurement system 5500 (Agilent Technologies).

Transmission electron microscopy (TEM) was performed on some of the CVD grown graphene samples (5 min of exposure to methane at 1000 °C). TEM images were taken using the Titan Themis 200 (FEI) microscope equipped with Schottky field emission gun and Cs DCOR probe corrector. The microscope was operated at 80 kV, which is below the knock-on damage threshold of graphene. The lower accelerating voltage also allows increasing scattering cross section of atoms, which is beneficial for observation of very thin samples consisting of light elements.

Bare Ni, Ni/MLG and aryl-modified Ni/MLG samples were characterized by X-ray photoelectron spectroscopy (XPS). The XPS measurements were carried out with a SCIENTA SES-100 spectrometer using a non-monochromatic Al Ka X-ray source (1486.6 eV).

The quartz crystal microbalance was used to characterize the growth of ZrO_2 by ALD. The QCM data were recorded by Q-pod monitor (Inficon) connected to an AT-at quartz crystal (IQD). A 5–10 nm thick ZrO_2 buffer layer was deposited on every QCM crystal used in the experiments to avoid the unwanted impact of the sensor electrodes on the measurements. The QCM data of the ZrO_2 deposition was recorded on each sensor three times, first after the deposition of the buffer layer, then after subjecting the sensor to wet treatment procedure and finally after the graphene transfer to the upper side of the sensor. The aim of the wet treatment procedure, which included covering the sensor with PMMA with its subsequent dissolving in dichloromethane, was to mimic the wet treatment conditions during the graphene transfer process to elucidate the possible effect of such a treatment on the behavior of the sensor. In order to avoid signal variations due to possible differences in sensors characteristics, the same sensor was used for the deposition of ZrO_2 in all the three steps. Taking into account that graphene was transferred to only the upper side of the QCM sensor, the QCM signals were recalculated respectively.

4.9. Electrochemical characterization of graphene grown on nickel foils

The electrochemical behavior of Ni/MLG was compared to GC and HOPG that were purchased from NII Grafit and SPI Supplies, respectively. The GC electrode was polished to a mirror finish with 1.0 and 0.3 μm sized alumina abrasives (Buehler) and then sonicated in Milli-Q water, isopropanol and acetonitrile (Sigma-Aldrich) for 5 min in each liquid. The fresh surface of HOPG was prepared by peeling off the uppermost layers of the graphite with adhesive tape shortly before the experiments.

Electrochemical characterization was performed using an Autolab potentiostat/ galvanostat PGSTAT30 (Eco Chemie B.V.) in a specially designed three-electrode cell with a saturated calomel reference electrode and platinum wire counter electrode. The GC, HOPG, bare Ni or CVD-grown MLG on nickel served as a working electrode. The working electrode surface area of 0.64 cm^2 was defined

with the opening of Kalrez® O-ring (DuPont). All the potentials are reported relative to the reference electrode. Cyclic voltammetry (CV) was conducted at a potential scanning speed of 0.1 Vs^{-1} in Ar-saturated 0.1 M KOH (p.a. quality, Merck) electrolyte and Ar-saturated 1 mM $K_3Fe(CN)_6$ (Sigma-Aldrich) solution containing 0.1 M K_2SO_4 (Merck) as a supporting electrolyte. The electrocatalytic activity toward oxygen reduction was investigated using linear sweep voltammetry (LSV) method in O_2-saturated 0.1 M KOH). All solutions were prepared with Milli-Q water, and the electrochemical testing was performed at ambient temperature (23±1 °C).

4.10. The modification of CVD-grown graphene with aryl groups

The CVD-synthesized graphene on Ni foil was modified with aryl groups by electrochemical reduction of different diazonium salts. The mechanism of this method, first introduced by Pinson and Savéant group [321], is demonstrated in Figure 10. In order to attach azobenzene (AB), (2-methyl-4-(2-methylphenyl)azo) benzene (GBC), 2,5-dimethoxy-4-((4-nitrophenyl)azo) benzene (FBK), 4-bromophenyl (PhBr) and 4-nitrophenyl (NP) groups to graphene correspondingly azobenzene diazonium tetrafluoroborate, Fast Garnet GBC sulphate salt, Fast Black K salt, 4-bromobenzenediazonium tetrafluoroborate and 4-nitrobenzenediazonium tetrafluoroborate were used.

Fast Garnet GBC sulphate salt, Fast Black K salt, 4-bromobenzenediazonium tetrafluoroborate, 4-nitrobenzenediazonium tetrafluoroborate were of commercial origin (Sigma-Aldrich) and used as received. Azobenzene diazonium tetrafluoroborate was synthesized in the lab according to the general procedure. Specifically, 0.01 mol of 4-Aminoazobenzene was dissolved in 100 ml of the mixture of acetone (Lach-Ner) and water (1:1 volume ratio) and held in an ice bath. Then 0.01 mol of sodium nitrite (Merck) and 0.01 mol of hydrochloric acid (37%, Sigma–Aldrich) were dissolved in 50 mL of the acetone-water mixture (1:1 volume ratio) and added to the previously prepared solution. After filtering the solution, 0.01 mol of sodium tetrafluoroborate (98%, Sigma–Aldrich) was added. The reaction product was cooled below 0 °C, filtered by suction and then washed with ice water and cold ether followed by drying in a desiccator.

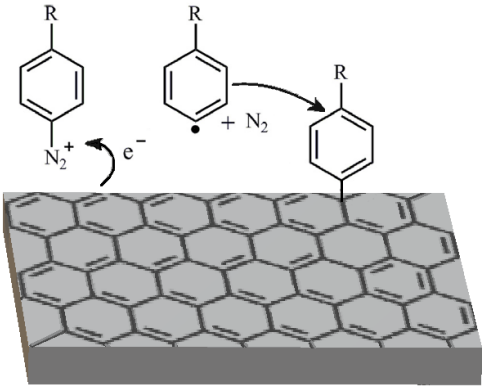

Figure 10. Proposed reaction pathway for the modification of the CVD-grown MLG on nickel with aryl groups by reduction of diazonium cation.

These aryl-modified Ni/MLG electrodes (Figure 11) are denoted further as: Ni/MLG/AB, Ni/MLG/GBC, Ni/MLG/FBK, Ni/MLG/PhBr and Ni/MLG/NP.

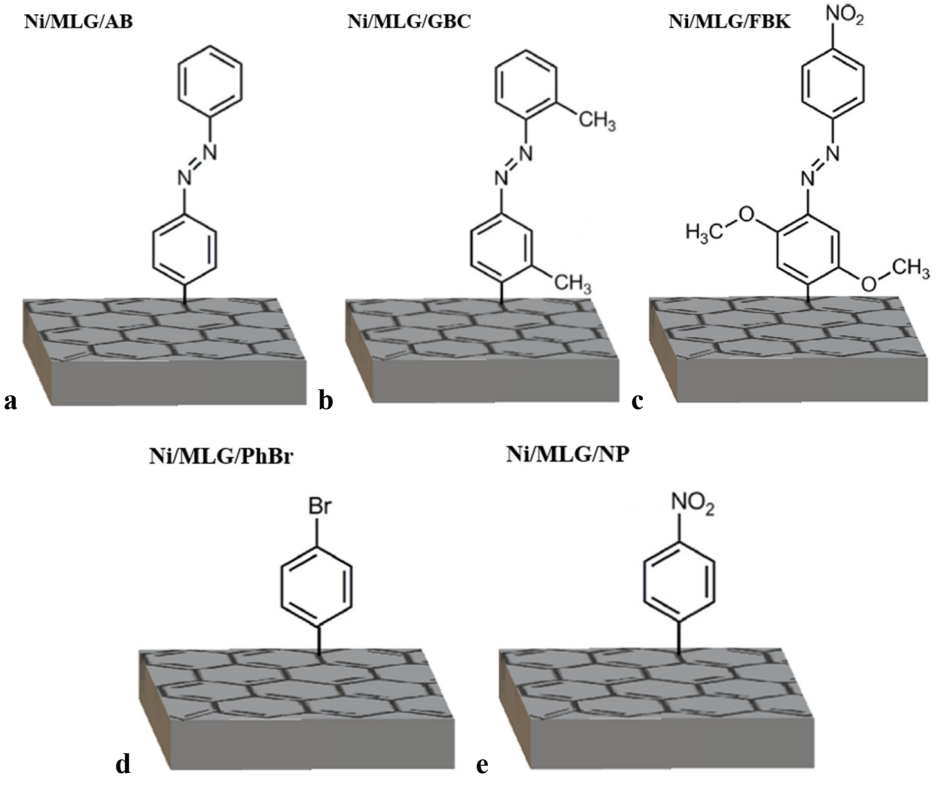

Figure 11. Surface modifiers attached to CVD-grown MLG on nickel by electrochemical reduction of: (a) azobenzene diazonium salt; (b) Fast Garnet GBC sulphate salt; (c) Fast Black K salt; (d) 4-bromobenzenediazonium tetrafluoroborate and (e) 4-nitrobenzene-diazonium tetrafluoroborate.

Surface modification of Ni/MLG electrodes was conducted using repetitive potential cycling in Ar-saturated acetonitrile (Sigma–Aldrich) containing 1mM of the corresponding diazonium salt and 0.1M tetrabutylammonium tetrafluoroborate (Fluka) as a supporting electrolyte. The electrografting of MLG with AB, GBC, FBK and PhBr groups was performed applying potential cycling from 0.4 to –0.4 V for 10 cycles at 0.1 Vs^{-1}. For electrografting with NP groups three different conditions were employed:

(1) one cycle in a potential range from 0.6 to –0.5 V at 0.1 Vs^{-1} (further denoted as Ni/MLG/NP1);
(2) ten cycles in a potential range from 0.6 to –0.5 V at 0.1 Vs^{-1} with a holding at –0.2V for 10 min in order to increase the thickness of the NP layer (further denoted as Ni/MLG/NP2);
(3) ten cycles in a potential range from 0.6 to –1.4 V at 1 Vs^{-1} (Ni/MLG/NP3);

After electrochemical grafting, the aryl-modified Ni/MLG electrodes were thoroughly rinsed with acetonitrile in order to remove weakly adsorbed species.

5. RESULTS AND DISCUSSION

5.1. Micromechanically exfoliated graphene

(Paper V)

The examples of exfoliated graphene samples are presented in Figure 12. The optical microscope (Figure 12a,c) and AFM (Figure 12b,d) images show that prepared graphene samples consist of different number of graphene layers. The thickness inhomogeneity is obvious already from the color variation within the flakes in the optical images and is further confirmed by the height variation on AFM images. On AFM images the steps between areas with different number of graphene layers can be discerned. As can be seen, the graphene flakes may not lay flat on the surface. The flakes can be partially detached from the substrate and the edges can be curved upwards. This makes the determination of the number of graphene layers by the height measurement of the graphene flake by AFM inaccurate.

The exact number of graphene layers was determined using Raman spectroscopy. According to Raman spectroscopy the number of graphene layers in the presented flakes varied from more than 10 layers to the 2 layers. Figure 13a and b show the Raman spectra recorded from the thinnest areas of the flakes in Figure 12a and Figure 12c, respectively. Both spectra show intense G and the 2D bands and no or low intensity D band, which indicates the high crystalline quality of the samples. The 2D band in both spectra is symmetric without characteristic to graphite shoulder on its low frequency side. In Figure 13a the 2D band has lower intensity compared to the G band and can be divided with 2 Lorentzian fitting curves. The splitting of the 2D band is 23.9 cm^{-1} and according to the literature [244] corresponds to the 3-layers thick graphene. In Figure 13b the 2D band is more intense compared to the G band. However, the FWHM of the 2D band is 44 cm^{-1}, which is not corresponding to the FWHM value for the single-layer graphene (30 cm^{-1}). When divided by the two Lorentzian fitting curves the splitting of the 2D band is 19.2 cm^{-1}, which corresponds to the bilayer graphene [244].

The areas of SLG were also identified among prepared flakes. The SEM and AFM images of the graphene flake containing areas of SLG are presented in Figure 14. As can be seen from the images, the thickness of this flake is not homogenous containing also thicker areas. The Raman spectrum from the thinnest area of the flake is presented in Figure 15. The spectrum features symmetric and narrow (FWHM = 28.3 cm^{-1}) 2D band, which is 4.5 times more intense than G band. All these features indicate the presence of a SLG. The thickness of the flake was also measured by AFM. The AFM measured height of the edge was 0.86 nm, which is in accordance with the reported height of the single-layer measured in the atmospheric conditions [195]. Unlike AFM, SEM images do not provide the information about height of the graphene flakes. Nevertheless, as it is apparent from Figure 14a, SEM images are very useful for rapid estimation of the thickness

homogeneity of the prepared graphene. If to compare SEM and AFM images from the same area, it is obvious that areas with different number of graphene layers are much more distinct on SEM images compared to the AFM images. Due to the superior sensitivity of AFM to height variation, the residues left on graphene surface after exfoliation as well as the upturned edges are very prominent on AFM images obscuring the milder contrast associated with difference in number of graphene layers.

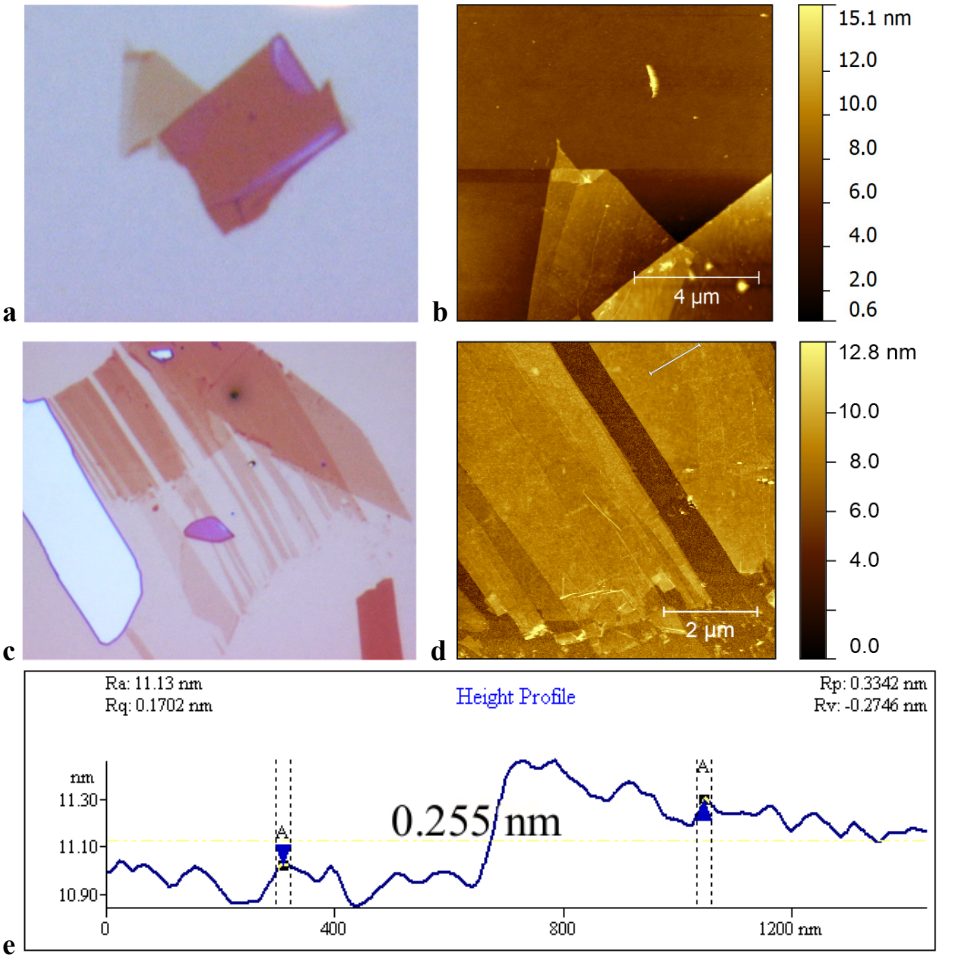

Figure 12. (a, c) Optical images and (b, c) AFM images of the micromechanically exfoliated graphene flakes. (e) AFM height profile measured on graphene flake along the line shown in the image (d).

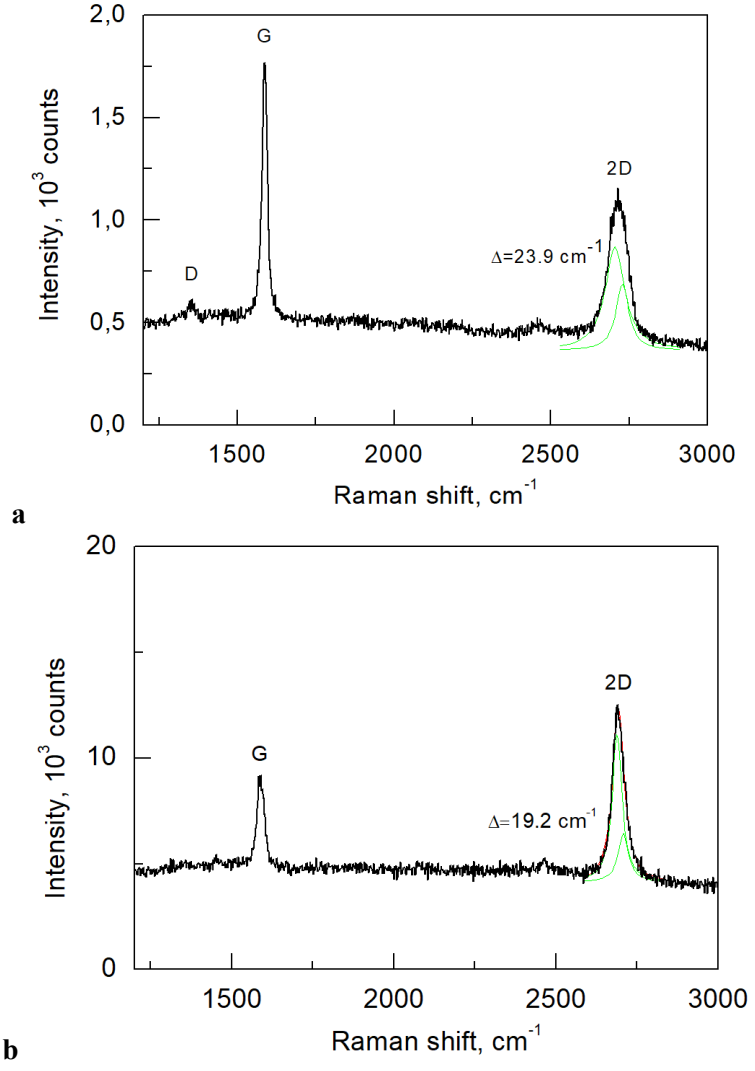

Figure 13. Raman spectra of the thinnest areas of exfoliated graphene samples presented in Figure 12.

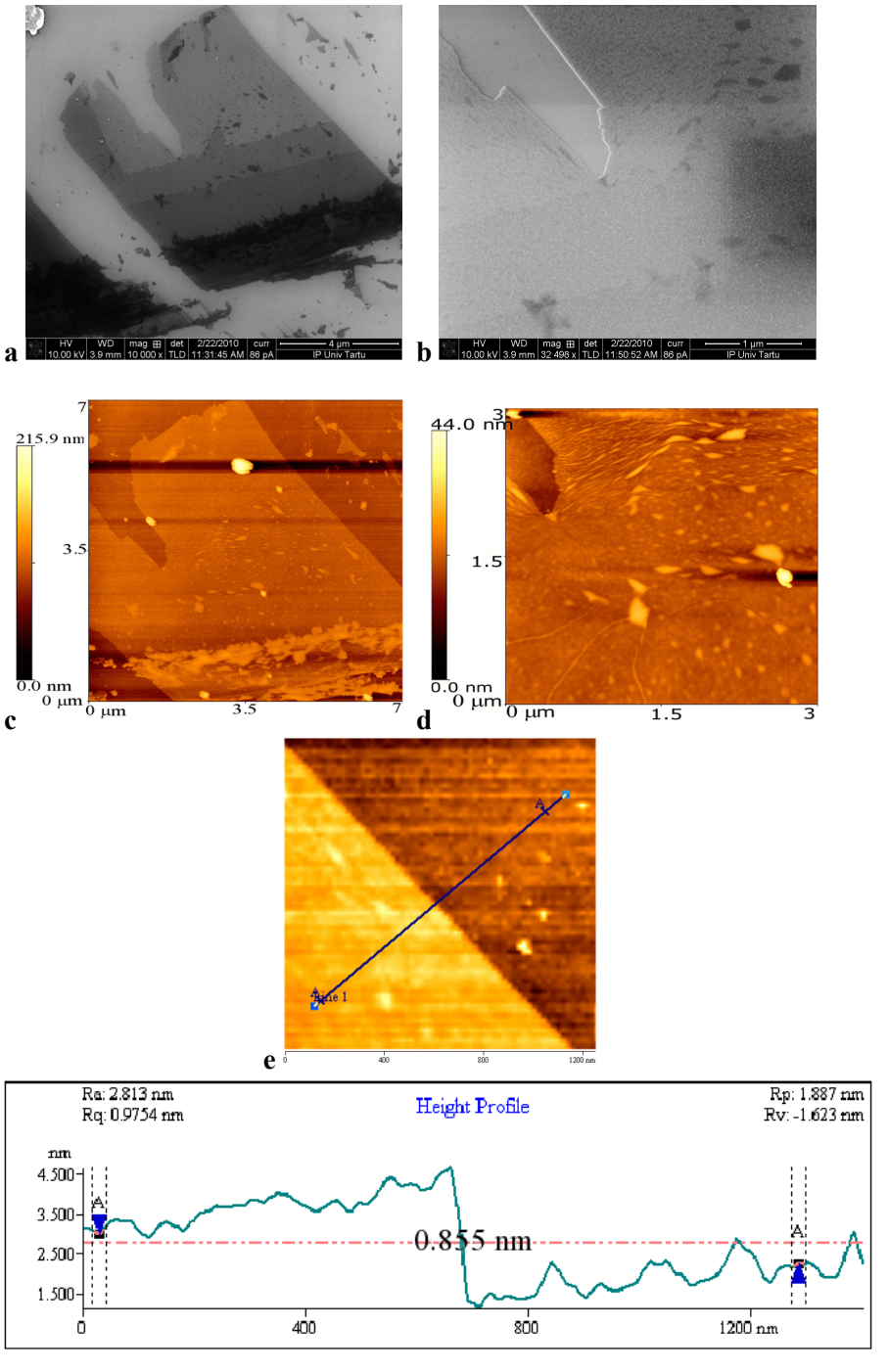

Figure 14. (a, b) SEM images and (c, d) AFM images of the same micromechanically graphene exfoliated flake. (f) AFM height profile measured at the edge of a graphene flake along the line shown in the image (e).

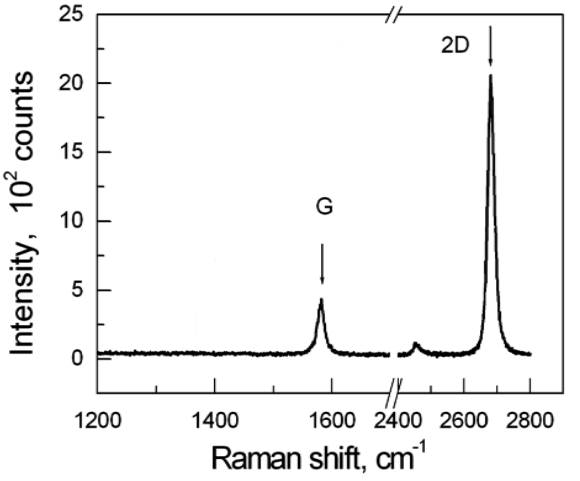

Figure 15. Raman spectrum from the thinnest area of the graphene flake presented in Figure 14.

5.2. Graphene synthesized on nickel foil

(Paper I)

5.2.1. Initial stage of growth

Figure 16a and b show SEM images of the nickel surface after 45 s of methane exposure at 1000 ºC. Two types of graphene islands can be discerned: larger ones with average dimensions of several micrometers (some being larger than 10 μm) and numerous small islands with dimensions less than several hundreds of nm. Small graphene islands can be divided into two groups. The islands of the first group exhibit somewhat elongated shape with the prolongation direction parallel to the longest side of the underlying nickel grains. The islands of the second group have nearly circular shape irrespective of the orientation of the underlying nickel grains. As the shape of the islands of both groups does not deviate much from a circular shape, it indicates that, at high temperatures of the graphene growth, the surface diffusion rate of carbon atoms can be interpreted as isotropic, at least at the island edges far enough from the grain boundaries of the substrate. For the islands nucleated near or on the grain boundaries, elongation of graphene islands was observed along the boundary.

It can be seen, that the nucleation of graphene islands is not completely random. Although some of the grains have a large number of nucleation centers, other grains can be completely uncovered. It should be noted that the contrast within the graphene islands is nonuniform, which indicates the variation in the thickness. It is remarkable that, already at the beginning of graphene growth, the islands consist of more than one layer despite the fact that most of the surface is still uncovered. Darker areas, which correspond to thicker graphene coverage,

were sometimes observed in the middle of the islands, but more frequently on the island periphery. When the exposure time to methane was increased to 2 minutes at 1000 °C, approximately half of the surface was covered with graphene (Figure 16c,d). The size of the islands increased such that their coalescence was observed in numerous areas. In addition, there are a large number of small islands that may act as secondary nucleation centers. After 5 minutes of exposure, most of the nickel surface is covered with graphene (Figure 16e, f). However, some uncovered areas, which appear as the brightest regions, still remain on the surface. The borders of the uncovered areas tend to coincide with the nickel grain boundaries. These results confirm that the crystallographic orientation of the nickel grains has an influence on graphene growth. It is interesting to note that the areas covered with graphene exhibit a wrinkled morphology, which was not observed in the initial stages of graphene growth. The stepped morphology of the uncovered areas also became more pronounced. The graphene appears to spread to uncovered grains from well-covered grains along these steps.

Even after 1 hour of exposure to methane at 1000 ºC, discontinuities in the graphene coverage remain (Figure 16g, h). Because the topography and electron channeling contrast of the underlying nickel substrate can affect how dark or bright certain areas appear in the SEM images, both EBDS and EDX mappings were conducted to investigate the carbon distribution on the nickel surface (Figure 17). The EBSD color map in Figure 17b shows the crystallographic orientation of the outermost surfaces of the nickel grains/crystallites relative to the sample surface normal direction (ND). The colors in the corners of the color-triangle (Figure 17e) show the low-index surfaces, and the colors between them indicate stepped low-cut or vicinal surfaces. The black or white points indicate that it was not possible to determine the crystallographic orientation of the crystallites surfaces in these points. To enhance surface sensitivity of the X-ray microanalysis, low acceleration voltage of 2 kV was employed for the EDS analysis. Quantitative maps of C K_α and Ni L_α are shown in Figure 17c and Figure 17d, respectively. The bar provided in the lower portion of the images represents the percentage of the element within the electron-excited near-surface volume. The EDX mapping confirmed that the carbon distribution on the surface is non-uniform, which is consistent with the SEM images. In addition, from the EDX maps an increased carbon signal was observed between nickel grains due to carbon precipitation or its faster diffusion at grain boundaries.

The holes in the coverage of graphene can also be clearly seen after graphene transfer (Figure 18a). Also, stripe-like areas produced due to not complete coalescence of long dendritic graphene branches can be seen (Figure 18b). It worth noting, that even defective sites could be transferred safely.

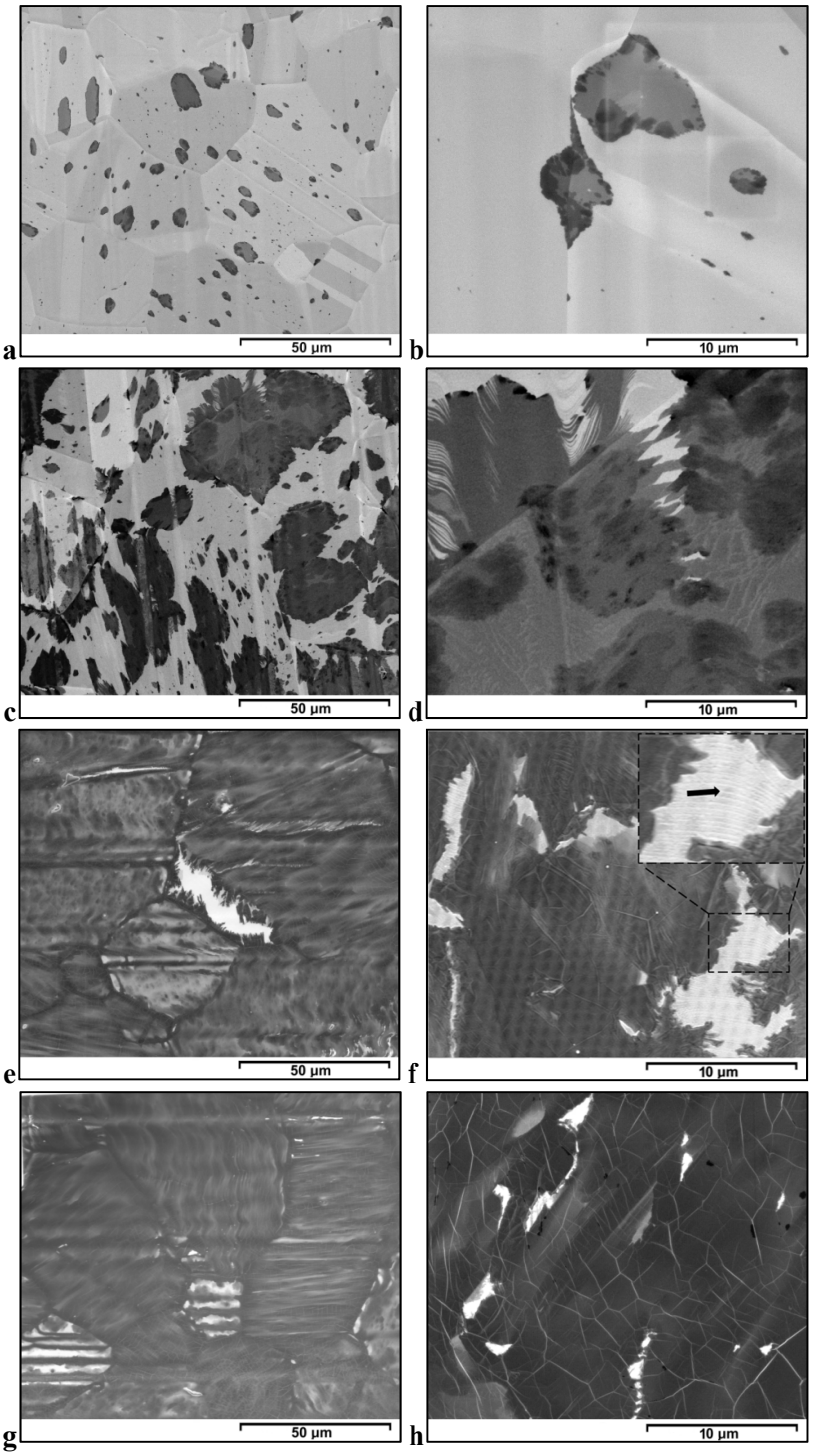

Figure 16. SEM images of the surface coverage with graphene film after the CVD process with (a, b) 45 s, (c, d) 2 min, (e, f) 5 min, and (g, h) 1 h of methane exposure at 1000 °C [I].

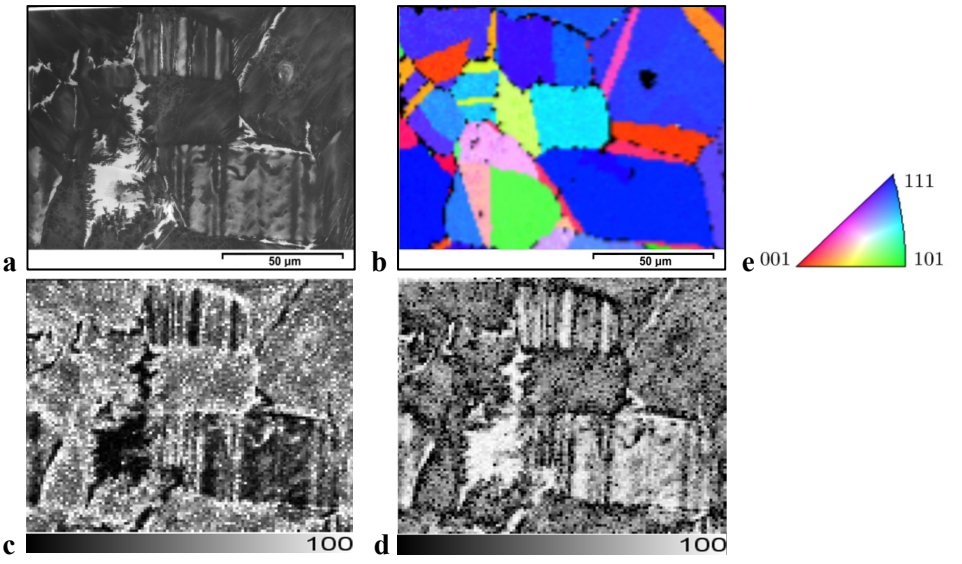

Figure 17. Comparison of the (a) SEM image and (b) EBSD map as well as the EDX quantmap of (c) carbon and (d) nickel from the same location on the sample after the CVD process with 5 min of methane exposure at 1000 °C. The bars on the EDX quantmaps indicate the concentration of the analyzed element in the analyzed volume [I].

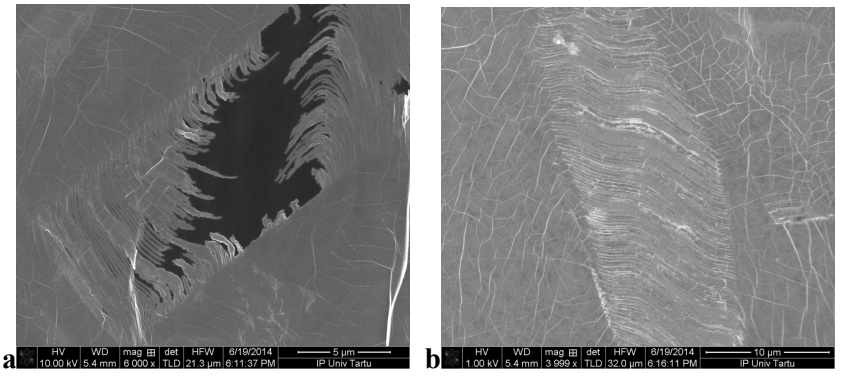

Figure 18. SEM images of CVD-grown graphene (5 min of exposure to methane at 1000ºC) after transfer to Si/SiO_2 substrate, showing areas with (a) holes and (b) not wholly merged dendritic branches.

5.2.2. Influence of the crystallographic orientation

In order to study the dependence of nickel grain orientation on graphene coverage, EBSD mapping was performed after different periods of CVD growth. As can be seen, after methane exposure for 5 minutes (Figures 16e,f and 17) and 10 minutes (Figure 19) at 1000 °C, a noticeable difference in the coverage of graphene was observed on different grains. The grains with a crystallographic orientation close to Ni(111) are well covered with graphene. However, non-continuous graphene coverage was observed on grains oriented close to Ni(001) and especially on higher index surfaces (e.g., rose-colored grains with an orientation roughly in the middle between Ni(111) and Ni(001), or yellow-colored grains with a surface orientation that was roughly in the middle between Ni(001) and Ni(101)). Graphene appears to extend to these faces from neighboring grains, forming long dendritic branches oriented along the steps on the nickel substrate (Figures 16d, 17a and 19c). In contrast, continuous graphene coverage was obtained on light blue colored high-index grains with an orientation in the middle between Ni(111) and Ni(101).

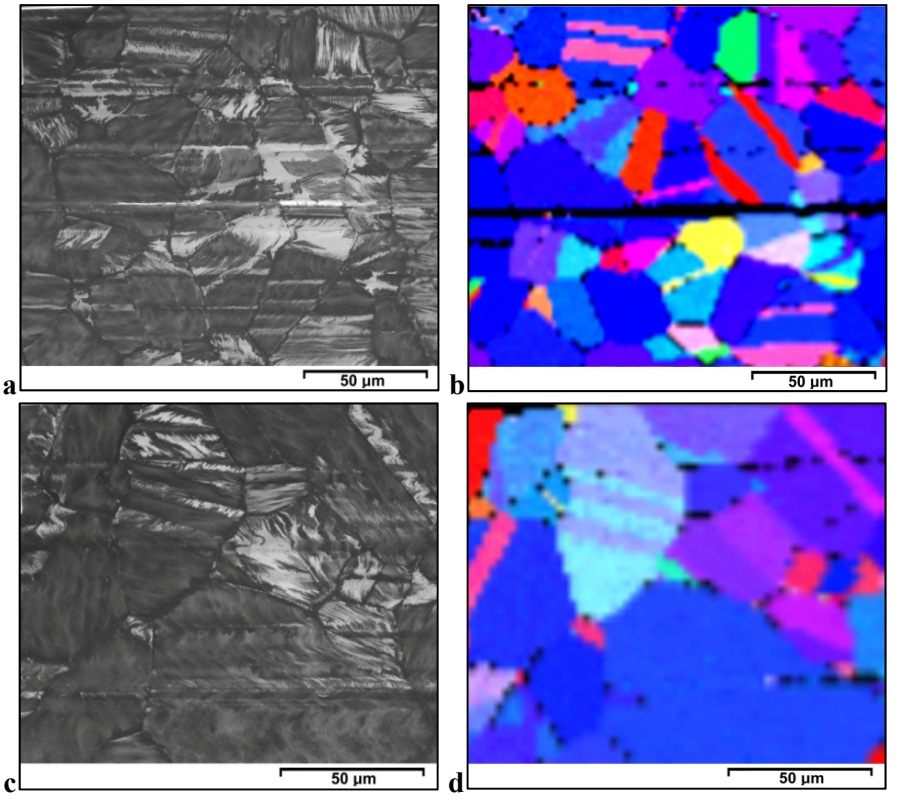

Figure 19. Comparison of (a, c) SEM images and (b, d) EBSD orientation maps taken from the same area in two locations showing the dependence of coverage on grain orientation after 10 min of methane exposure at 1000 °C [I].

After the increase of the methane exposure time to 1 h at 1000 ºC (Figure 20), the grains with a (001) orientation as well as the high-index surface areas are almost completely covered with graphene. However, some small holes or discontinuities in the graphene coverage were still observed, especially if the area of these grains was quite large (Figure 20a and b). The dependence of graphene formation on the nickel crystalline orientation has been reported by Takahashi et al. [184], who studied *in situ* graphene formation by annealing nickel foils pre-covered with disordered graphene layers in an SEM chamber. The observed difference in graphene formation on the (001)-oriented grains was explained by the higher binding energy of the carbon atoms to this surface compared to the (111) surface. However, the situation may be more complicated because during graphene growth, apparent surface restructuring occurs in some areas, including the generation of steps that introduce additional surface orientations. Besides, it may be possible that some metal areas suffer from the surface reconstruction. As shown in Figures 17b, 19b and 20d, the grains with surface orientations near to the (111) exhibit slightly different shades of blue with an average misorientation angle of approximately 10º. Notably, the less the orientation of the grain deviates from the ideal (111) orientation, the thinner the graphene coating is formed on the grain (Figure 20e). With this extended exposure time, the peculiar coverage of the grains with a sharp Ni(111) orientation was more prominent. These grains exhibit a distinctive graphene coverage pattern and are characterized by periodic bands of thinner and thicker graphene areas.

Next, to improve the homogeneity of graphene coverage, a "slow-cooling process" was utilized. As shown in Figure 21a, the slow cooling yielded the opposite effect. The SEM image shows areas with apparently very thick graphitic coating with a wrinkled morphology and areas with significantly thinner graphene coverage. The EBSD map (Figure 21b) indicates that the areas with a thinner coverage have a (111) orientation. Therefore, surface restructuring during graphene growth may cause carbon transfer from the (111)-oriented grains to the neighboring grains (e.g., by enhanced surface diffusion). The overall effect of the slow cooling rate is a significant increase in the thickness inhomogeneity of the graphene coating. The grains with orientation close to the Ni(111) have thinner graphene coating, and the thinnest coating is observed on grains with ideal Ni(111) orientations. Grains with other orientations are covered with multilayer graphene.

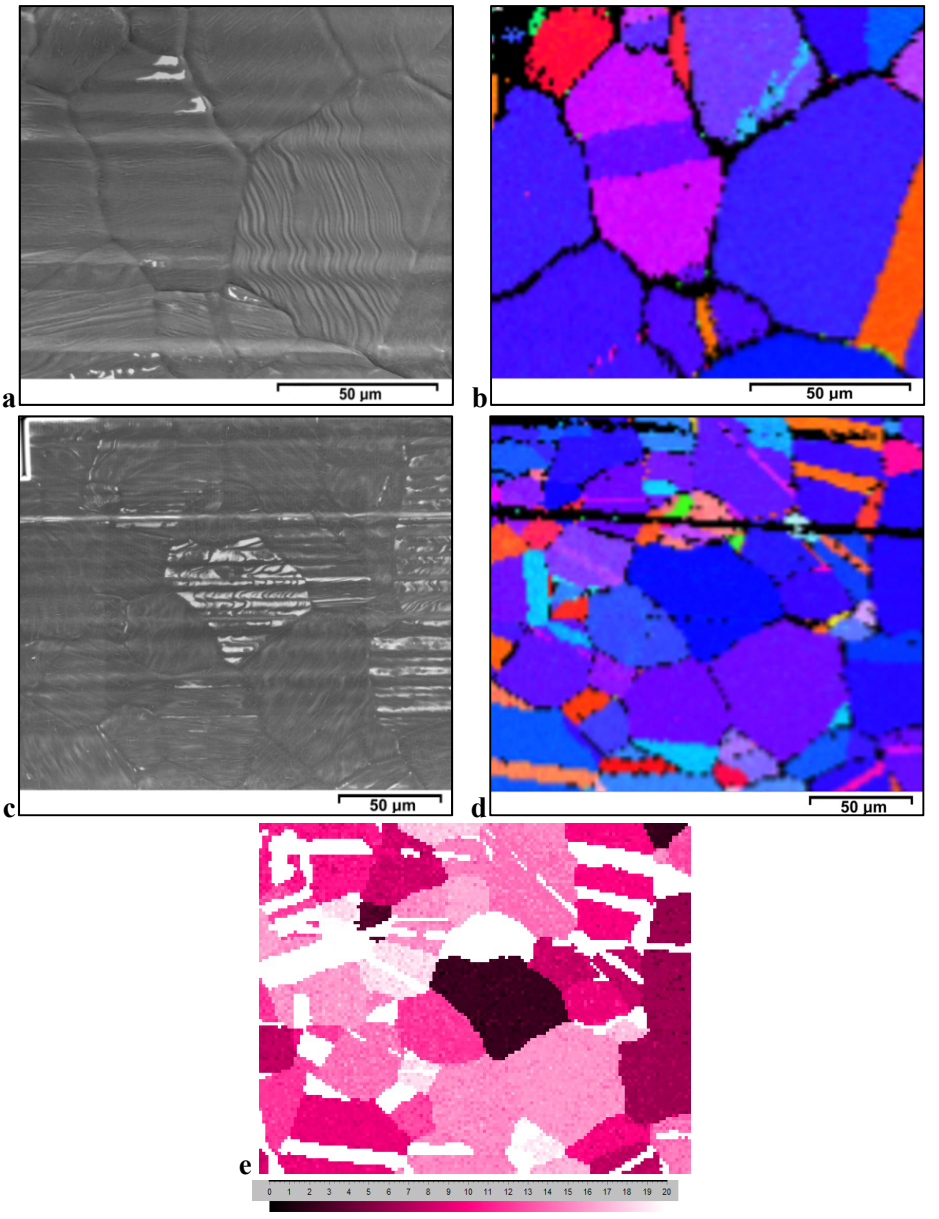

Figure 20. Dependence of the MLG coverage on the grain orientation of a sample after 1h exposure of Ni to methane at 1000 °C: (a, c) SEM images and (b, d) EBSD orientation maps taken from the same area in two locations of the sample (color-coding the same as in Figure 17e), and (e) EBSD angle map, taken from the area presented in (c, d) and showing orientation deviation of the grains from Ni(111) orientation in the angle interval from 0 to 20 degrees (see the scale at the bottom of the image) [I].

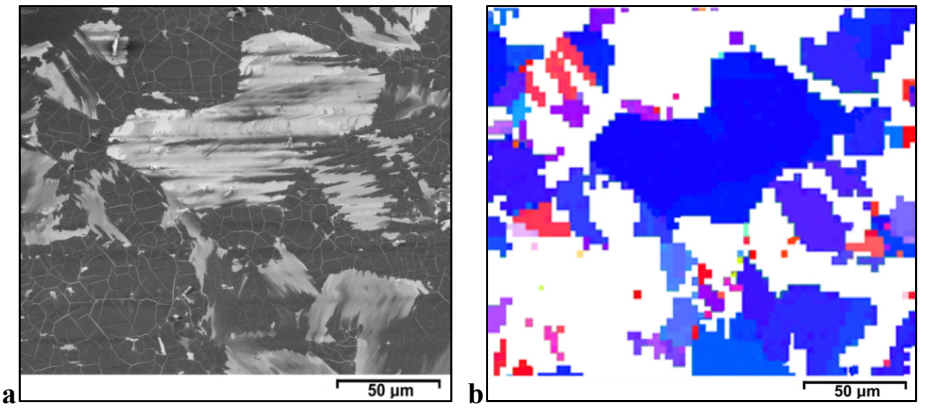

Figure 21. Comparison of the (a) SEM image and (b) EBSD orientation maps from the same area after the CVD growth with a "slow cooling process"; the white color on the EBSD map indicates areas where the EBSD signal was not obtained [I].

5.2.3. Transformation of the nickel substrate during MLG growth

The microstructure of the nickel foil before the exposure to methane has been explored by SEM and EBSD (Figure 22). As shown in the SEM micrograph in Figure 22a, the size of the grains in as-received nickel foil is approximately 5 µm. The striations resulting from the rolling process of the foil are visible on the surface. As shown in Figure 22b, the nickel surface has a wide range of crystallographic orientations. However, grains with an orientation close to the Ni(111) orientation are more common. The nickel crystal has a face-centered cubic unit cell, and the Ni(111) surface, which possesses the lowest surface energy, also has the smallest lattice mismatch with graphene and is considered to be the most suitable for graphene growth. After 1 hour of annealing in the Ar/H_2 flow, the SEM micrograph of the foil indicates a much smoother surface morphology (Figure 22c). The deepest rolling striations are still visible, but overall, they are less pronounced. The nickel foil is largely recrystallized, and the size of the crystallites has significantly increased. As shown in Figure 22d, annealing did not have a significant effect on the crystallographic orientation of the grains. In addition to the Ni(111) face, facets of higher surface energy remain on the nickel surface after annealing.

Morphology changes in the nickel surface were observed during graphene growth. In Figure 23a, the AFM image of the Ni foil after only the annealing step (performed at the same conditions as in case of graphene syntheses, and during cooling step the gases flow was the same as during the annealing) displays a smooth surface with flat terraces separated by steps of subnanometer height. Brief exposure to methane for 2 minutes led to the appearance of periodic surface modulations that are visible in the areas not covered with graphene (Figure 23b). These wavy surface modulations appear well ordered with a peak height of ≤ 1 to 10 nm, as shown in Figure 23c, and a period from 30 to more than 100 nm

depending on the particular place. However, areas between the graphene islands retained their smooth morphology. Apparently, graphene islands impede the motion of steps on the catalyst surface, which could be induced by surface energy anisotropy. Besides, chemisorbed molecules can facilitate surface diffusion of nickel atoms by weakening the bonds between neighboring substrate atoms [322,323]. As the step flow proceeds, the velocity of the step is affected by the graphene nucleation events on the terraces in front of the steps, which leads to different step velocities and bunching of the steps. The graphene covered areas also exhibit a rougher morphology (Figure 23c). In contrast to the bare nickel surface between the graphene islands, these areas lacked the ordered pattern or initial flat relief and exhibited an irregular bumpy surface. To determine if the observed corrugated morphology was caused by the difference in the heat expansion coefficient between graphene and nickel, the graphene was removed from the surface using argon plasma cleaning. As shown in Figure 23d, after graphene removal, the surface exhibits the same roughened morphology, which indicates that the graphene growth induces structural transformations in the nickel surface.

In order to determine the dependence of the nickel substrate morphology on the graphene growth period, two samples were studied with SEM after partial removal of graphene coating using the plasma treatment. In Figure 24a, the first sample with thick graphene coverage is shown, which was obtained after 5 minutes of growth followed by a "slow cooling process". The nickel exhibits pronounced surface changes characterized by the high steps with rough edges. The second sample was prepared with prolonged graphene growth (~1 hour), and the graphene layer was partially removed from it by 20 minutes of plasma treatment (Figure 24b). The SEM image reveals a surface covered in steps meandering by graphene islands. In some places, the moving steps were unable to overcome precipitates bent around the obstacle on both sides, forming nearly circular closed step loops. Thus wave-like structures (meandering steps) can be a result of the disturbances created by nucleation events on initially straight steps. In graphene covered areas, the surface diffusion, as well as sublimation and redeposition of substrate atoms, is inhibited, which hamper the advancement of the steps leading to decreased velocity compared to the steps on an open surface. Phase coherence of the steps develops later due to the effective step-step repulsion. A driving factor responsible for morphological instability is asymmetric step kinetics induced by carbon adsorption and nucleation of graphene islands. The step bunches seem to favor graphene nucleation and subsequent expanding graphene to the whole terrace. Thus, the surface changes increase as the graphene growth time increases. During graphene growth for a long duration of time at high temperatures, the reorientation of the metal grains accompanied by a restructuring of their surface may contribute to the changes in the surface morphology. Also, based on the strong bright contrast along the edges between graphene free areas and areas where graphene was not completely removed by plasma cleaning (Figure 24a), a height difference was observed between these areas. The areas where the graphene was not completely removed were most likely covered with

thicker graphene, and they appear to be somewhat lower compared to the areas, which had fewer graphene layers. This observation strengthens the previous suggestion that the nickel surface is intensely mobile during graphene growth. The constantly changing surface during graphene growth may result in incomplete coverage of the metal surface with graphene even during a prolonged growth process and the formation of rotational disorder in the synthesized graphene coatings.

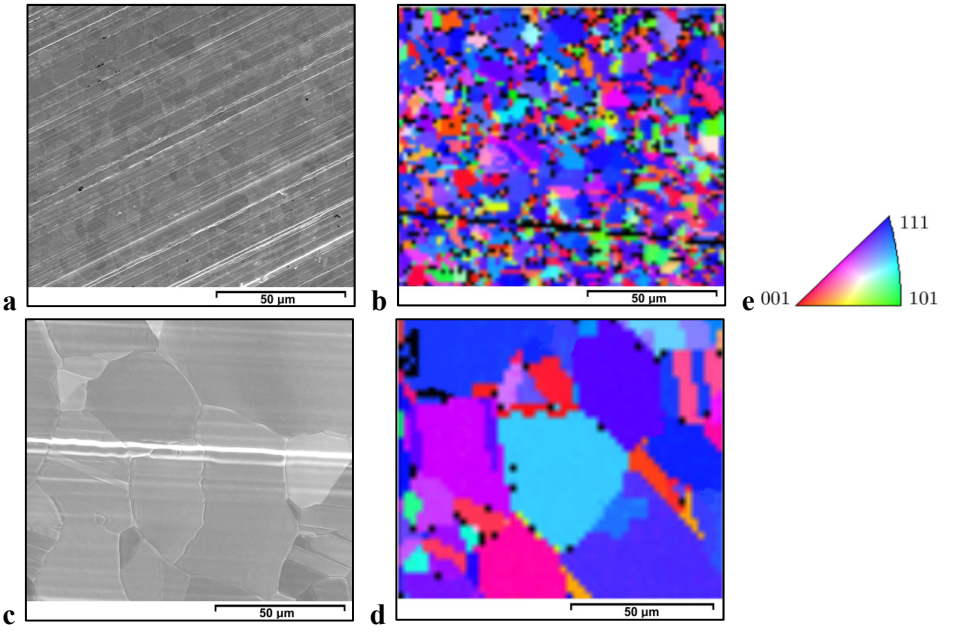

Figure 22. SEM images of nickel foil (a) before and (c) after annealing. EBSD orientation map of nickel foil (b) before and (d) after annealing as well as the (e) color key associated with different crystalline orientations [I].

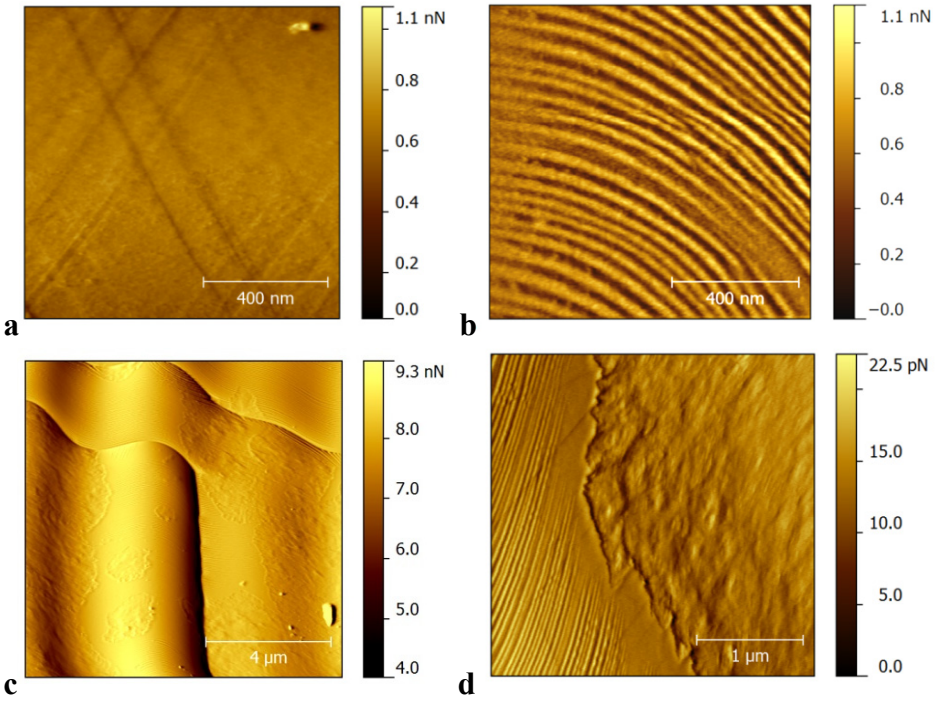

Figure 23. AFM images taken in error-signal mode of the surface of the nickel foil: (a) after annealing, (b) after CVD growth (2 min of methane exposure at 1000 °C) between the graphene islands, (c) after CVD growth (2 min of methane exposure at 1000 °C), and (d) after CVD graphene removal with plasma cleaning [I].

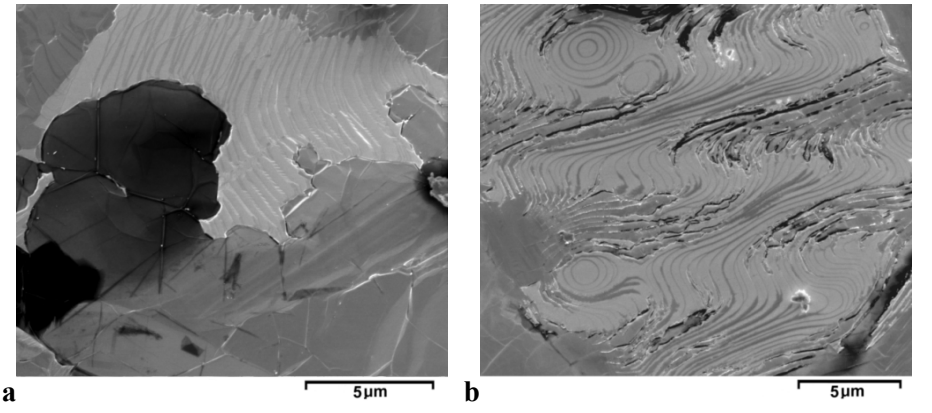

Figure 24. SEM images of the surface of the Ni foil with graphene partially removed by Ar plasma cleaning: (a) CVD growth with 5 min exposure to methane at 1000 °C and "slow cooling process" with methane flux and (b) CVD growth with 1 h of exposure to methane at 1000 °C [I].

5.3. Structure of graphene grown on nickel: Raman study

(Papers I–II)

Figure 25 presents typical Raman spectra of the graphene recorded on the nickel foil after 30 minutes of methane exposure at 1000 ºC, where a nearly continuous coverage was obtained. As shown in the overview spectrum in Figure 25a, the intensity value of the G band (1583 cm^{-1}) is higher than that of the 2D band (2715 cm^{-1}), and the last band has an asymmetric shape. This band can be divided into two Lorentzian curves with maxima at 2734 and 2703 cm^{-1} (not shown), and a band splitting of Δ_{2D}=31 cm^{-1}. Based on the relationship of Δ_{2D} to the number of graphene layers [244], in the AB-stack approximation, the number of graphene layers was estimated to be 10±1. This AB-stack approximation was confirmed by the existence of weak spectral bands between 1650–1800 cm^{-1} (right inset, Figure 25a), which correspond to the out-of-plane combination modes of the longitudinal optical (LO), out-of-plane acoustic (ZA), out-of-plane optical (ZO') and an overtone of another out-of-plane breathing vibration mode (ZO): (LO+ZA, LO+ZO', 2ZO). These modes are specific to the AB-stacked graphene [238,324,325]. In addition, the Raman features in the range of 80 to 130 cm^{-1} corresponding to the ZO' breathing modes, and facilitating by rotational disorder [257,326], are missing (left inset, Figure 25a). All of these Raman features indicate the presence of MLG that primarily consists of graphite-like AB stacked layers.

In certain regions over the sample, the spectra were similar to that shown in Figure 25b. In this case, the Raman spectrum consists of a very intense and narrow 2D band (2707 cm^{-1}) as well as a low-intensity G band (1582 cm^{-1}). The integral intensities ratio (A_{2D}/A_G) can reach a value as high as 15 or greater (e.g., in Figure 25b, A_{2D}/A_G = 6.7). Although the spectrum in Figure 25b is similar to the spectrum of SLG, no decrease in the carbon concentration was observed in these areas in the EDX maps compared to the neighboring grains (Figure 27b). The rotation of the adjacent graphene planes can result in the Raman spectra of thicker graphene being similar to that obtained for SLG. This behavior was primarily reported for misoriented (non-AB stack) bilayer systems [256,260,327]. However, this peculiarity was also predicted for misoriented multilayer graphene [22] and demonstrated on multilayer graphene grown on the C-face of SiC [23,328]. In contrast to the AB stack (Figure 25a) in the spectra obtained in these distinctive areas, the bands connected with the out-of-plane modes in the 1650–1800 cm^{-1} spectral range are missing, and the bands connected to the in-plane combination modes of the longitudinal optical (LO), transverse acoustic (TA), transverse optical (TO) and longitudinal acoustic (LA) vibration modes (LO+TA, TO+LA, LO+LA, TO+TA) between 1800–2250 cm^{-1} are well pronounced (right inset, Figure 25b). Along with the high value of the A_{2D}/A_G ratio, this effect is unique to weakly bonded layers inside the graphene system with stacking disorder between the layers [238,324]. Additional information on the stacking order can be obtained by the bands connected to the rotation modes (R) [257,258,329], which appear in the lower energy region of the spectrum between

defect band D at 1357 cm^{-1} and band G at 1582 cm^{-1} (right inset, Figure 25b). In this spectral range, at least two bands assigned to R modes were isolated at 1383 and 1483 cm^{-1}. The corresponding rotation angles (θ) were estimated to be approximately 26° and 13.5°, respectively, based on the $\omega_R = \omega_R(\theta)$ relationship [258]. In the spectral range of 80–130 cm^{-1} belonging to the ZO' breathing modes [257,326], several overlapping Lorentzian peaks were observed. The most intense peaks of them are located at 106, 115 and 121 cm^{-1}, which indicate the presence of several rotated graphene layers that have slightly different breathing frequencies. Based on the recent estimates [330,331], these peaks most likely correspond to a combination of vibrational modes, which involve both the ZO' breathing and shear (C) modes, (ZO'+C) in the misoriented portion of the multilayer graphene.

The most spread on the sample were the areas with mixed structure, which consist of AB-stacked layers along with rotationally faulted graphene layers. A typical set of Raman scattering spectra for this type of domain is presented in Figure 25c. The Raman spectrum displays two intense commonly symmetrical bands G and the 2D located at 1582 cm^{-1} and 2707 cm^{-1}, respectively. The intensity of the G band was less than the intensity of the 2D band. The A_{2D}/A_G integral intensity ratio was 5, which is quite similar to that for the Raman spectrum of exfoliated SLG. However, the widths of the bands were too large for single-layer graphene, and the broad the 2D band can be divided into two subbands at 2695 and 2716 cm^{-1} with an interval between the maxima (the 2D band splitting) of 21 cm^{-1}, giving in the AB-stack approximation for the number of graphene layers on Ni substrate approximately 3 [244]. Indeed, the AB stack was observed after the LO+ZO' peak at 1752 cm^{-1} (right upper inset, Figure 25c). However, the use of the AB stack approximation to estimate the number of layers is inadequate because additional details in the spectrum exist, which demonstrates the substantial role of the rotationally faulted graphene layers. In the same inset, other details of this Raman spectrum are shown. The in-plane vibration modes (i.e., LO+TA, TO+LA, LO+LA, TO+TA [238,324,332]) and two sharp lower energy peaks due to the rotation modes at 1421 and 1479 cm^{-1} were observed. Based on the given frequency values for the rotation modes, the corresponding twisting angles between the stacking graphene layers were determined to be approximately 20° and 14°, respectively.

The role of rotational stacking was further approved by Raman analysis of the breathing modes ZO' and ZO (left and lower right insets, Figure 25c). As in the previous case (Figure 25b), in the spectral region of the ZO' breathing modes, a structure exists, which can be divided into three Lorentzian-shape bands (at 107, 115 and 122 cm^{-1}) of several rotated graphene layers in MLG. The Raman peak at approximately 800 cm^{-1} [241] appears in the ZO breathing mode range, and its exact position has a tight relationship to the spectral position of the rotation mode R and, therefore, to the rotation angle θ [326]. On the high background, due to the Ni substrate, some very weak peculiarities in this region were detected, including a broadened structure below 800 cm^{-1} and peaks at 820 and 841 cm^{-1} (lower right inset, Figure 25c).

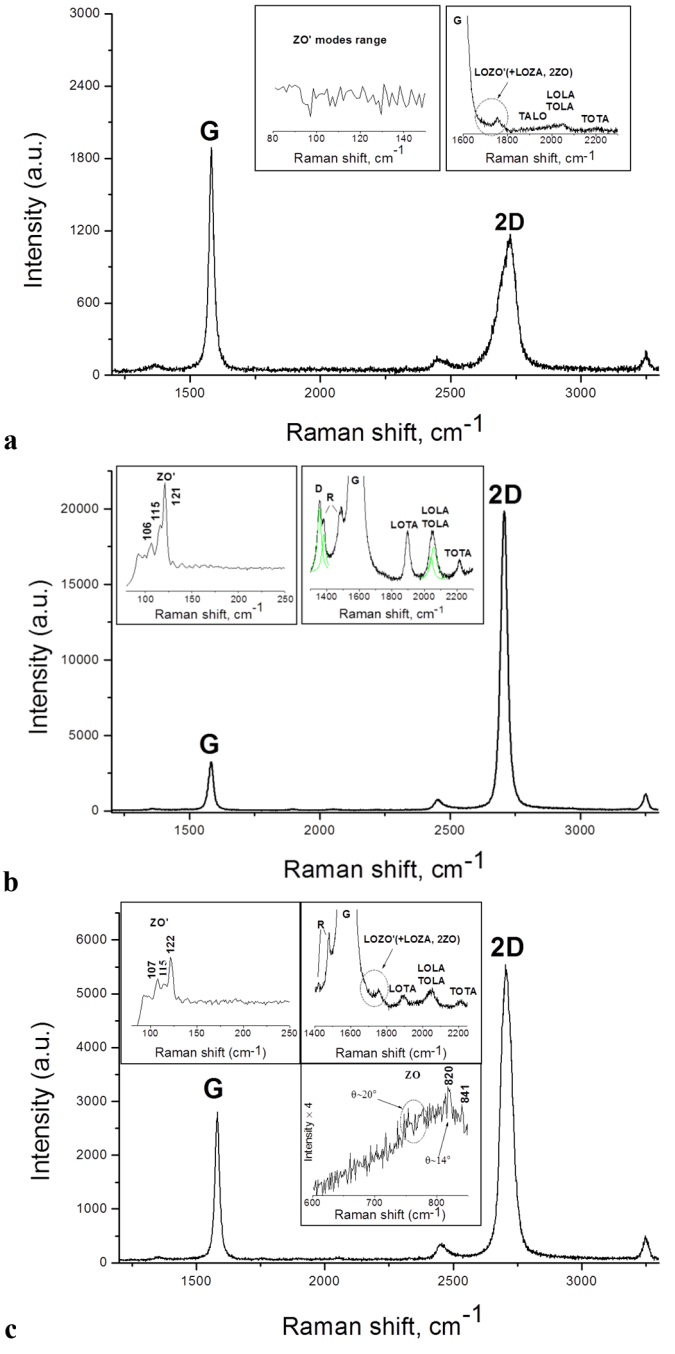

Figure 25. Raman spectra from different areas on the substrate: (a) MLG with AB stacking, (b) misoriented MLG, (c) MLG with a mixed structure of AB and rotationally faulted graphene layers stacking [I].

Two former peculiarities agree well with the results that in the spectrum, two R bands at 1421 and 1479 cm^{-1} exist and affirm the appearance of two rotation angles at 20° and 14° for multilayer graphene film. The peak at 841 cm^{-1} confirms the additional twisted graphene layer(s) with an angle of approximately 10°. The corresponding rotation mode was not observed in the Raman spectrum even though it should appear in the region above 1500 cm^{-1}, where it coincides with the intense G band.

Figure 26 shows the correlation between crystal orientation mapping and the obtained Raman spectra. The Raman signal with the unusually high 2D/G ratio was primarily observed on the grains with an orientation roughly in the middle between Ni(001) and Ni(111).The triangular, rhombic and circular symbols superimposed on the EBSD orientation map correspond to the spots locations where spectra similar to Figure 25a, Figure 25b and Figure 25c, respectively, were measured.

Therefore, the Raman characterization of CVD graphene on the Ni catalyst indicates that there is a great variety of multilayer graphene domains with very different stacking orders that distinguish the MLG from the graphite. The exact number of graphene layers cannot be precisely determined due to the presence of rotational disorder between the graphene layers. The results from the Raman scattering spectra of CVD grown graphene on Ni foil unambiguously indicate the existence of AB stacked and rotated layers that are located together as well as separately inside the multilayer graphene domains. The rotation of the graphene layers affects the electronic properties of the synthesized graphene sheets. As shown for the large rotation angles, the misoriented graphene system can exhibit apparent SLG behavior [21]. In particular, the rotation disorder induced electronic decoupling between layers can lead to high charge carrier mobilities even in multilayer structures [333].

Besides the graphene regions discussed above, there were small regions, the Raman spectra of which characteristically exhibited the increased intensity of the G band. One of the spectra obtained from this type of region is presented in Figure 28. The ratio of the G and 2D peak areas (A_G/A_{2D}) in the spectrum is higher than three. In addition, the spectrum shows a prominent rotation mode (R) peaking at 1485 cm^{-1} and a ZO mode of considerable intensity centered at 825 cm^{-1} (Figure 28, right inset). The positions of both bands correspond to the same rotation angle of 13° [256,258,329]. Remarkably, that identified angle is very close to the critical angle, θ_{cr}. Also, in contrast to the previously described spectra of misoriented MLG, in this spectrum, a new spectral feature consisting of several components emerges in the spectral range of 130–200 cm^{-1} (Figure 28, left inset). It can be noticed that this spectral feature is similar in shape and number of sub-components to the structure in the ZO' layer-breathing modes range. Therefore, it may be assumed that it corresponds to a combination of the ZO' layer-breathing modes with another vibrational mode appearing in the spectral range of approximately 50–60 cm^{-1}. Recently, a mode at 52 cm^{-1} has been observed in the misoriented bilayer graphene and assigned to the torsional mode, in which adjacent graphene layers rotate out of phase with each other [257]. Noteworthy, this mode

at 52 cm^{-1} has been observed in the bilayer graphene when the rotational angle between layers was close to the critical angle, as in the current case. Thus, the new feature in the spectral range of 130–200 cm^{-1} likely corresponds to the combination of vibrational modes involving both the ZO' layer-breathing and torsional mode. The appearance of this broad feature in the spectrum can, along with highly intensive G band, serve as an indicator of misoriented MLG, where the rotational angle between layers is close to the critical angle.

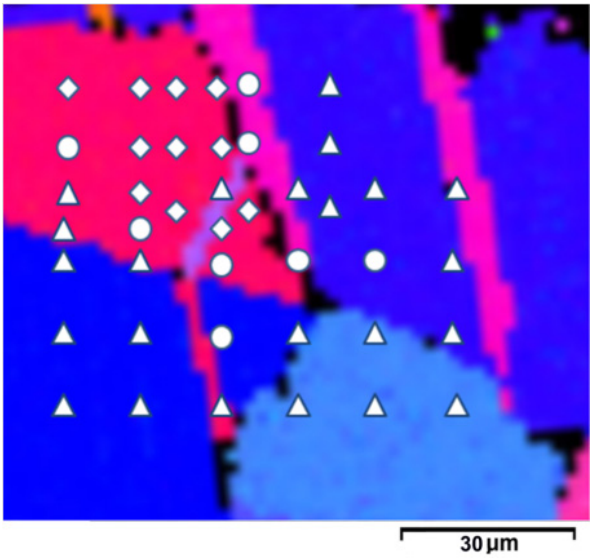

Figure 26. EBSD orientation map showing the orientation dependence of the measured Raman signal – symbol △ refers to the spectrum given in (a), ◇ refers to the spectrum given in (b), ○ refers to the spectrum given in (c) [I].

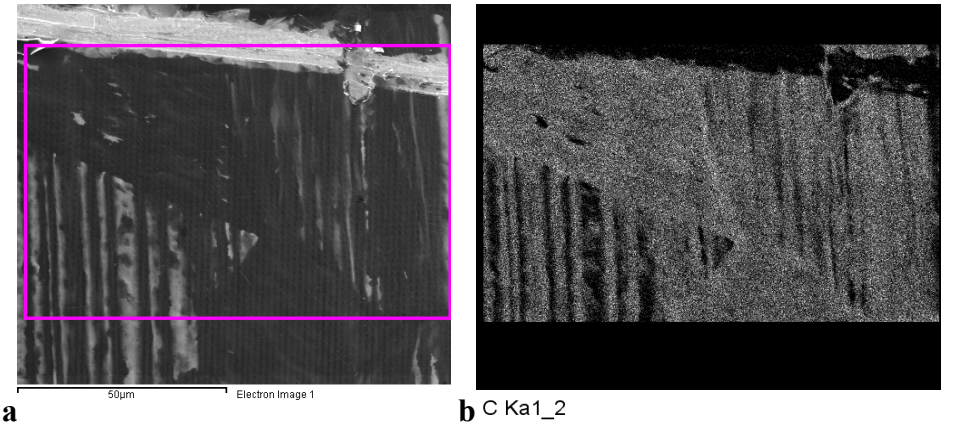

Figure 27. Local analysis of an area having very intense and narrow the 2D band in Raman spectrum: (a) SEM image from the area mapped in Figure 26 and (b) EDX mapping of carbon K_α line from the area marked by the rose frame in the (a).

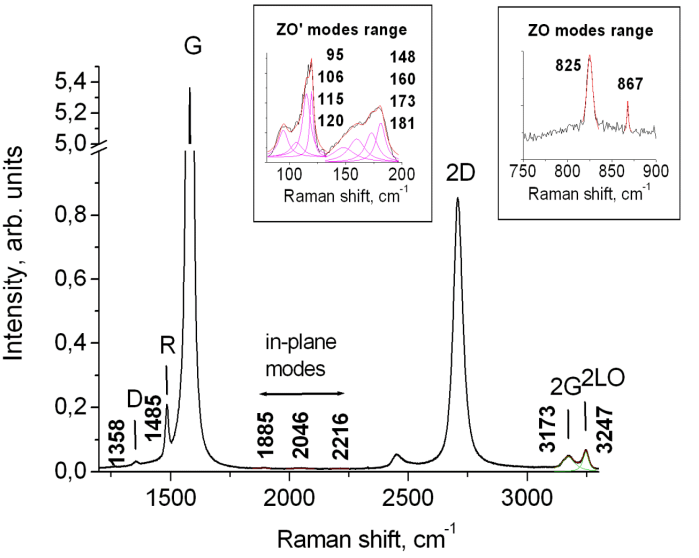

Figure 28. Raman spectrum recorded from the MLG regions with high intensity of the G band of multi-layer graphene on Ni [II].

Furthermore, a peak of unknown origin was present in the breathing (ZO) mode range at 867 cm^{-1}, in every spectrum, regardless of the stacking order of the graphene layers (Figure 28). To the extent of author's knowledge, the aforementioned peak has not been reported in the literature for graphene synthesized on nickel by the time this research was conducted. This peak showed no dispersion with a variation of the laser excitation energy (two excitation laser energies of 2.41 and 2.54 eV were examined). Notably, this peak was present also in the spectra of the MLG regions with AB-staking, where no other ZO phonon modes were observed. Still, the peak at 867 cm^{-1} was no longer visible after the transfer of MLG from the nickel to the Si/SiO_2 substrate. Therefore, it stands to reason, that this peak originates from the vibrations at or in the immediate vicinity of the graphene-nickel interface. Tentatively, the inequivalence in the adsorption sites of the carbon atoms on nickel surface may create favorable conditions [334] for activation of the layer-breathing (ZO) mode vibrations between the graphene layer bound to nickel and the subsequent graphene layer.

5.4. TEM studies of MLG graphene grown on nickel foils

The representative TEM images of graphene sheets transferred onto the TEM grid are demonstrated in Figure 29. The image shows a low-magnification bright-field (BF) image of the MLG sheet extending beyond the field of view of several hundreds of nanometers. Though, at this magnification, the lattice cannot be resolved, the sheet-like nature of the sample is apparent. The wrinkles within the graphene sheet can be seen in the upper-left part of the image. In the same part of

the image, it can be seen that one of the graphene layers is scrolled and folded back. As it is a bright-field image, the folded areas appear darker as the electron scattering probability increases with the thickness. The crack in graphene, which widens to the center of the shown area, can also be seen. The origin of the crack is the graphene domains that have not merged during the synthesis or damage introduced during the transfer process. The darker splotches visible in the multiple places are presumably contamination, most probably, PMMA residues. Nevertheless, clean areas can still be found between these contaminated areas, which appear at low magnification as featureless homogeneous regions.

More information can be obtained by analysis of electron diffraction pattern. The crystallinity of the MLG sheets was determined with selected area electron diffraction. Figure 29b shows normal-incidence selected area diffraction patterns for the sheet in Figure 29a. The well-defined diffraction spots confirm the crystalline structure of the imaged graphene samples. The electron diffraction from one graphene/graphite crystal would result in one set of six symmetric spots of reflection in the inner hexagon. Figure 29b shows two main groups of spots in the SAED pattern. In Figure 29b, the two sets of hexagonal patterns are relatively rotated by 5.8°. This is either due to differently oriented domains or rotational stacking faults between the layers within the field of view. Graphene has hexagonal symmetry, so from the SAED pattern, the angle up to 30° can be measured between different graphene domains/layers.

In order to identify the number of graphene layers in the sample, we found places that allowed a cross-sectional view of the graphene sheet. Figure 29c shows the BF-TEM image from an internal fold, and Figure 29d shows an image from the edge. At these places, the MLG sheet is locally parallel to the electron beam, and the number of graphene layers can be visualized. The number of dark lines in the images indicates the thickness of 8 to 11 layers in these areas.

Figure 29 e–f. show HRTEM images obtained by zooming into different regions in the suspended graphene sheet under study. The images were acquired with single, 5 seconds long exposures of CCD, and no image processing has been done to the acquired images. The images show lattice fringes of graphene, confirming the crystalline nature of the sample. The hexagonal arrangement of atoms in graphene crystal produces two diffraction planes with 0.213 nm and 0.123 nm spacing. Thus, in the fast Fourier transformation of the atomic resolution image of graphene, two sets of hexagons corresponding to these spacings should be visible. However, the lattice images can be already seen if the reflections corresponding to 0.213 nm spacing are transferred, but to be able to see individual carbon atoms, the reflection at 0.123 nm should also be present [335]. In the FFT of the image presented in Figure 29e, only reflection corresponding to 0.213 nm is well transferred, indicating that the 0.142 atom distances are not resolved in the image. The brightness variations visible in both images can be a result of the corrugations of the graphene surface as the phase contrast is sensitive to the focusing conditions. The changes in brightness can also be due to patchy surface contamination.

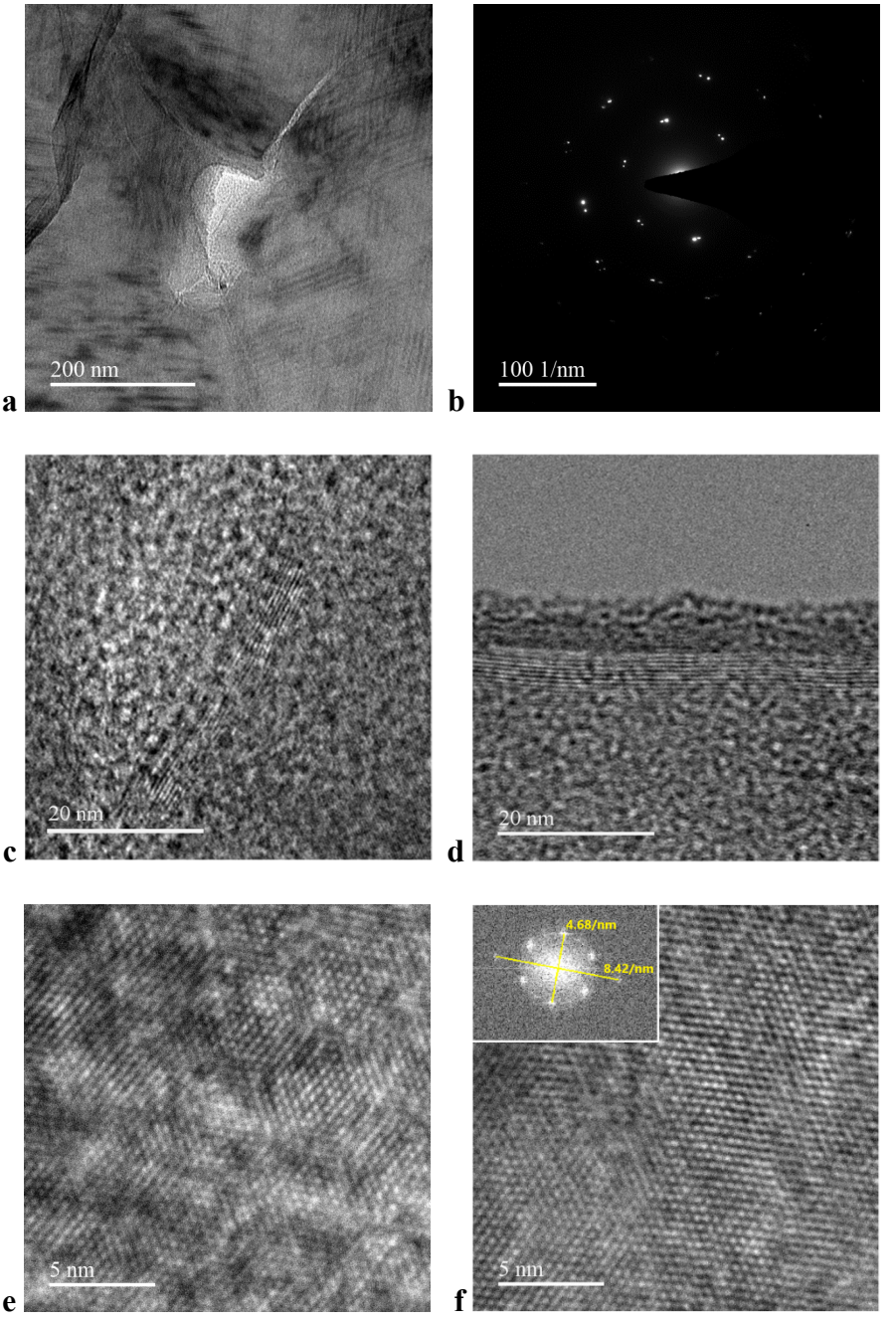

Figure 29. The TEM images of synthesized graphene sample: (a) Low – magnification BF-TEM image of a MLG sheet suspended over a hole in the TEM grid, (b) Electron diffraction pattern of the graphene sheet for close to normal incidence, (c, d) BF-TEM images from the regions, where the graphene sheet is locally parallel to the electron beam, (e, f) HR-TEM images of two different regions showing lattice fringes of graphene.

5.5. Graphene synthesized on thin nickel films

(Based on studies done to prepare FLG in the paper VI)

In order to obtain graphene sheets with fewer graphene layers, the Ni films were employed for graphene synthesis. Smaller thickness of the films compared to foils aimed to decrease the amount of the dissolved carbon and, thus, diminish the precipitation-induced graphene growth. Figure 30a shows the SEM image of the electron-beam evaporated Ni film on Si/SiO_2 substrate prior to the graphene synthesis, which exhibits uniform fine-grained morphology. After CVD process with 1 min of methane exposure at 900 °C, it can be seen (Figure 30b) that the Ni grains are significantly increased in size and now demonstrate variation in the brightness levels over the surface, which suggests the prominent non-uniformity in the graphene thickness over the observed area. Since the electron channeling contrast can also affect the brightness level of the particular grain, depending on its orientation relative to the e-beam, the synthesized graphene layer was transferred to the Si/SiO_2 substrate. Nevertheless, as can be seen, the variation of the brightness levels was still observed after the graphene transfer (Figure 30c), confirming the variation in the number of graphene layers on the μm-scale.

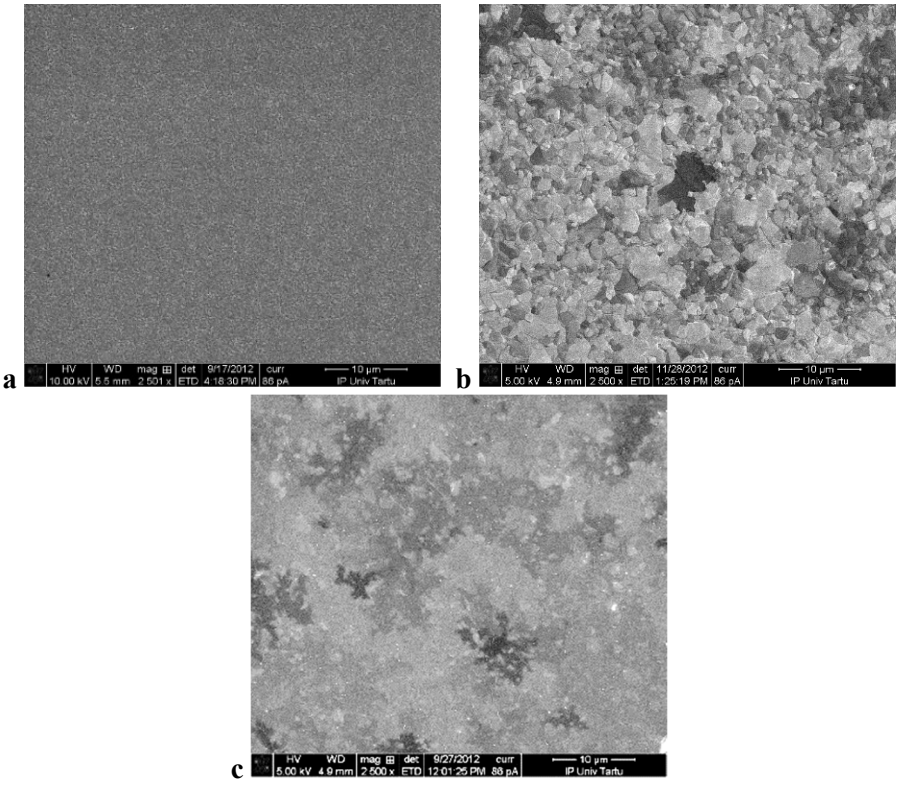

Figure 30. SEM images of the 140 nm-thick Ni film before (a) and after (b) graphene synthesis (1 min. of methane exposure at 900 °C); (c) the graphene sheet synthesized on 140 nm-thick Ni film after transfer to Si/SiO_2 substrate.

The uncovered areas on Ni film were hard to vizualize in the SEM and topographic AFM images due to the relatively rough topography of the nickel films. It was important, however, to investigate the continuity of the graphene sheets also before the graphene transfer to be sure that the observed discontinuities are not a result of the transfer procedure. The phase-contrast imaging in atomic force microscopy resulted in being a useful method to reveal the continuity of the coverage of nickel film with graphene. The uncovered areas can be clearly seen in phase-contrast images (bright areas in Figure 31b, d), which are not easily detected by topographic imaging (Figure 31a, c).

It should be pointed out that in contrast to the synthesis on nickel foil, on 140-nm thick Ni films, 1 min of methane exposure was sufficient to cover practically the entire surface. Apparently, due to smaller thickness, the nickel is faster saturated with dissolved carbon, and the local supersaturation of the carbon adatoms required for graphene nucleation is achieved within a smaller time interval.

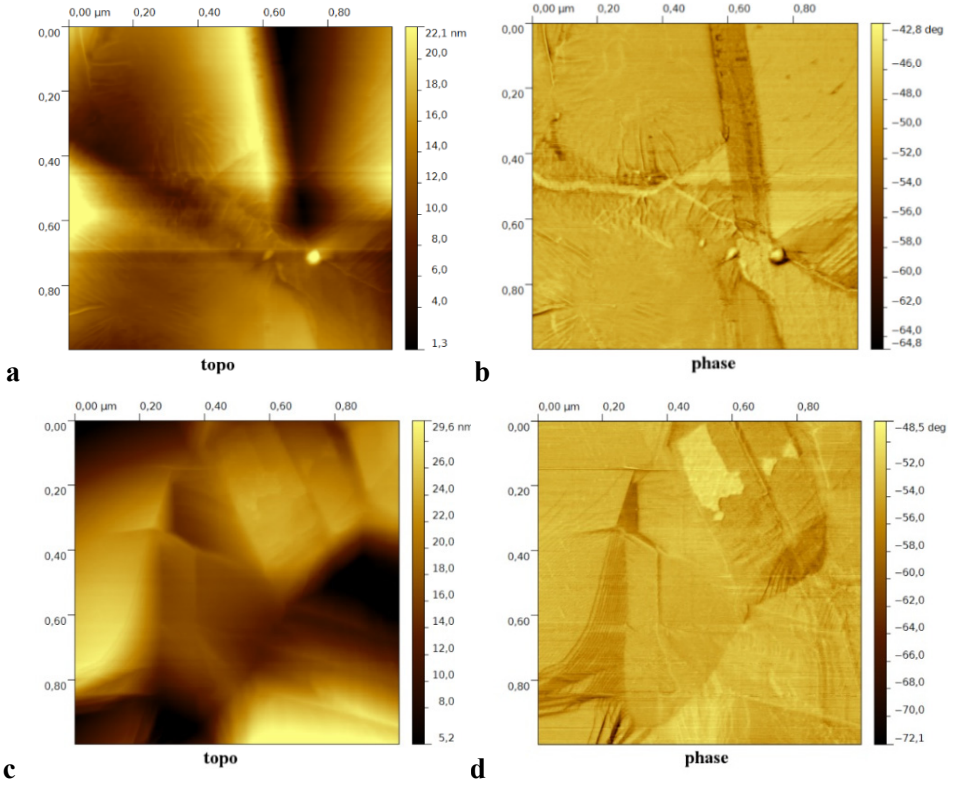

Figure 31. (a, c) Topographic AFM images and (b, d) phase-contrast AFM images of the 140 nm-thick Ni film after graphene synthesis.

The graphene sheets synthesized on Ni thin films were further examined using Raman spectroscopy. It should be noted that on contrary to the Raman studies of MLG, which were conducted directly on Ni foils, the graphene grown on Ni films prior to the Raman measurements was transferred to Si/SiO_2 substrate. The transfer of graphene was required because no or very faint Raman signal was detected if the measurements were conducted on as-synthesized graphene on Ni films. It has been demonstrated that the strong interaction between graphene and nickel substrate leads to loss of resonance condition for Raman scattering [334] and, therefore, on nickel, at least in the case of SLG, no Raman signal should be observed. The suppression of the Raman signal vanishes with the increase in the number of graphene layers, and the Raman spectra were successfully recorded in MLG synthesized on Ni foils.

The Raman spectra of graphene synthesized on Ni films with a thickness of 140 nm were characterized by a symmetric 2D band, the intensity of which was in most of the spectra higher than the intensity of the G band (Figure 32). Similar to MLG synthesized on Ni foils, the ratio of the intensity of 2D band to the intensity of G band (I_{2D}/I_G) as well as the FWHM of the 2D band noticeably varied on different locations of the sample. Table 1 presents a summary of mean Raman data collected from numerous locations over the sample. For comparison, the data obtained on the MLG synthesized on Ni foils and SLG synthesized on Cu foils (after transfer to Si/SiO_2 substrate) are also given in Table 1. As can be seen, the mean FWHM of the 2D band is significantly lower for graphene synthesized on Ni films compared to the Ni foils, being close to the mean value obtained on SLG. While the FWHM of the 2D band in the SLG samples prepared by micro-mechanical exfoliation did not exceed 31 cm^{-1}, the mean FWHM of the 2D band in CVD-grown SLG was broader, 34.8 cm^{-1}. The broadening of the 2D and G band in CVD graphene compared to the exfoliated graphene is in accordance with the literature [336]. An even higher increase in the linewidth of the 2D band in graphene grown on Ni films is apparently related to the increased number of graphene layers in the sample. The fact that the 2D band remains symmetric despite the increase of the number of the layers indicates the presence of the rotational disorder between graphene layers. In non-Bernal stacked graphene, the splitting of the 2D band cannot be used for the correct estimation of the number of graphene layers. The I_{2D}/I_G ratio, as has been previously shown on MLG synthesized on Ni foils, is also not a reliable indicator of the number of graphene layers, if the layers are misoriented with respect to each other. However, it is worth noting that the mean value of the I_{2D}/I_G ratio for graphene synthesized on Ni films was higher compared to that on Ni foils, approaching the mean value obtained on SLG synthesized on copper foil.

In several-layer-thick graphene samples, the position of the G band can be used to determine the number of the graphene layers in the sample [337,338]. It has been shown that the position of the G band downshifts with the number of graphene layers according to the relation as $1581.6+11/(1+n^{1.6})$ cm^{-1} [337], where n is a number of graphene layers. This relation can be used for graphene samples consisting of up to approximately 7 layers. For thicker samples, the position of

the G band becomes very similar to the position of the G band in graphite (1581.6 cm^{-1}). Even for FLG and several-layer thick graphene samples, the given relation should be used with caution, as the shift of the G band can also be a result of strain and doping. The position of the G band of SLG transferred from copper foil was, however, well in agreement with the relation-predicted value for SLG (1587 cm^{-1}). Based on the position of G band, the average number of graphene layers synthesized on Ni foils was estimated to be ≈ 3. The thickness of the graphene sample has also been shown to affect the position of the 2D band, which in contrast to G band upshifts with the number of graphene layers [339]. As can be seen from Table 1, the 2D band was only slightly upshifted compared to the SLG samples. Overall it can be concluded that the use of the nickel substrate with smaller thickness allowed decreasing the number of the graphene layers in the synthesized graphene sheet.

The second prominent difference of graphene synthesized on Ni films from graphene synthesized on Ni foils is the significant increase in the ratio of the intensity of D band to the intensity of the G band (I_D/I_G). The graphene synthesized on Ni foils was characterized by a low amount of structural defects, which is reflected in the low mean I_D/I_G ratio (0.05). For graphene synthesized on Ni films, the mean I_D/I_G ratio was 5 times higher. The higher amount of defects is graphene synthesized on Ni films might be related to the faster recrystallization of the nickel substrate during graphene growth.

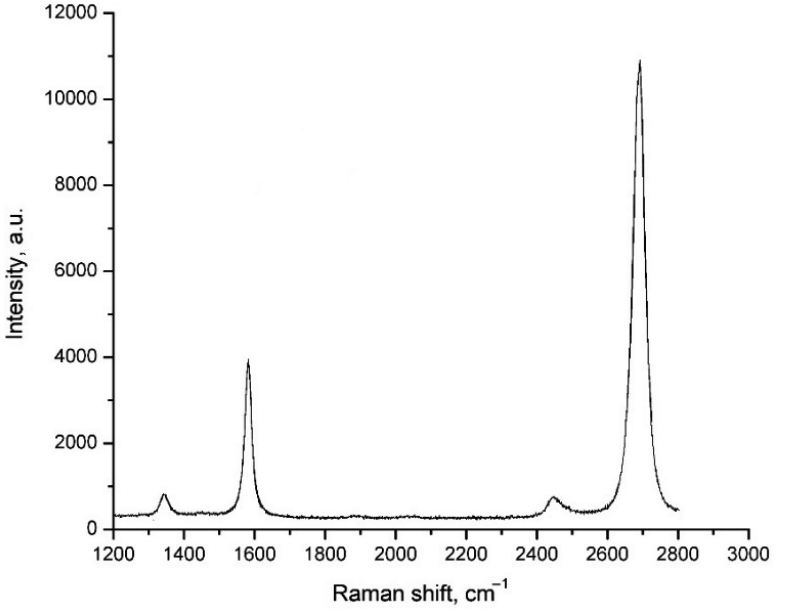

Figure 32. The representative Raman spectrum of graphene synthesized by CVD on 140 nm-thick Ni films.

Table 1. Mean values and single standard deviation from the mean of FWHM of the 2D band, spectral positions of the G and 2D bands, and the ratios of the intensity of the 2D band to the intensity of G band (I_{2D}/I_G), and the ratios of the intensity of D band to the G band (I_D/I_G) in graphene samples prepared by CVD on 140 nm-thick nickel films, nickel foils and copper foils. Mean values were calculated based on 50 spectra recorded on different locations on the sample.

Substrates	FWHM (2D), cm^{-1}	Position (G), cm^{-1}	Position (2D), cm^{-1}	I_{2D}/I_G	I_D/I_G
Ni films	38.1 ± 4.6	1583.7 ± 1.1	2688.7 ± 4.6	2.7 ± 1.5	0.25 ± 0.17
Ni foils	46.6 ± 8.6	1581.9 ± 1.0	2710.2 ± 3.9	2.2 ± 2.9	0.05 ± 0.02
Cu foils	34.8 ± 2.3	1586.5 ± 1.26	2687.9 ± 3.9	3.1 ± 0.6	0.02 ± 0.01

STM was used for atomic-scale observation of graphene growth on nickel films (Figure 33). The honeycomb lattice of graphene has been resolved in the STM image obtained on the sample. The observed six-fold symmetry is regarded to be a hallmark of SLG, whereas the areas with a larger number of graphene layers are expected to exhibit three-fold symmetry characteristic to the STM images obtained on graphite surface [340]. This assumption, however, might not be valid in the case of rotational disorder between graphene layers. It has been shown that in contrast to Bernal-stacked FLG, where only every second carbon atom on the surface is visible, all the atoms are imaged if the graphene layers are misoriented with respect to each other [22]. Therefore, the observation of the hexagonal symmetry might not be a reliable indicator of the presence of SLG. In addition, in some areas, stripe-like morphology with a period of ~1.3 nm has been observed (Figure 33b). In the higher magnification image obtained from this area (Figure 33c) again, the individual hexagons of carbon atoms are clearly visible and the FFT yields hexagonal symmetry of graphene. The distance measured between the nearest carbon atoms is ~0.14 nm and corresponds to the distance between the nearest carbon atoms in graphene. Similar stripe-like morphology has been previously reported on SLG on Ni (110) [341] Ni (100) [342] and Fe(110) [343] surfaces. It was found that the observed morphology is a result of a lattice mismatch between the graphene layer and the lattice of the underlying metal. It also has been noted that the strong interaction between graphene and metal is a prerequisite for the appearance of this type of morphology [343]. Therefore, it is likely that SLG areas were present in the graphene sheets synthesized on Ni films.

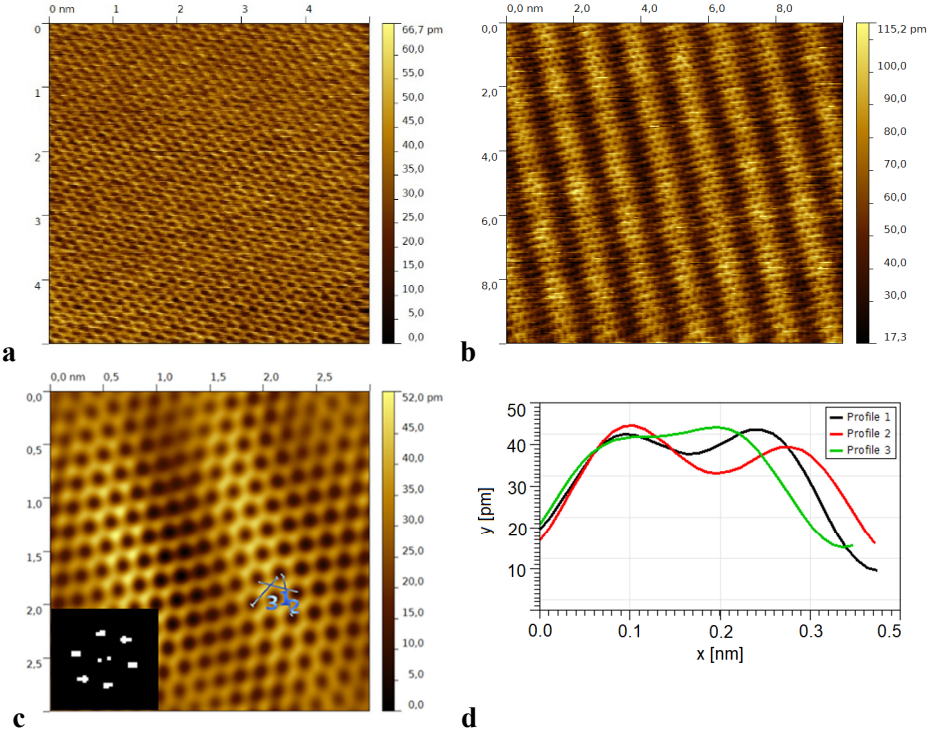

Figure 33. (a–b) STM images of graphene grown on nickel film exhibiting (a) flat and (b) periodically corrugated morphology, scanning area is 5×5 nm^2 and 10×10 nm^2, respectively; (c) magnified image of the area shown in (b), the inset is Fast Fourier transform of the corresponding image; (d) line profiles along the numbered lines in (c).

Since the number of graphene layers in graphene sheets synthesized on 140-thick Ni films was smaller compared to graphene on nickel foils, it was of interest to conduct the graphene synthesis on even thinner films. Unfortunately, nickel films thinner than 140 nm were subjected to solid-state dewetting, which led to the disintegration of the nickel films under the conditions used for graphene synthesis. Figure 34a shows the holes formed in the 80 nm-thick Ni film after graphene synthesis. Further reduction of the thickness of the film to 60 nm led to the formation of discrete Ni islands (Figure 34b) during graphene growth. As can be seen from the image Figure 34c the resulted graphene layer was also in the form of discrete islands.

Further studies are needed to find out whether could be found any other industrial high-temperature substrate material allowing to use thinner continuous Ni films, and thereby synthesize single/few-layer graphene sheets in more controllable way.

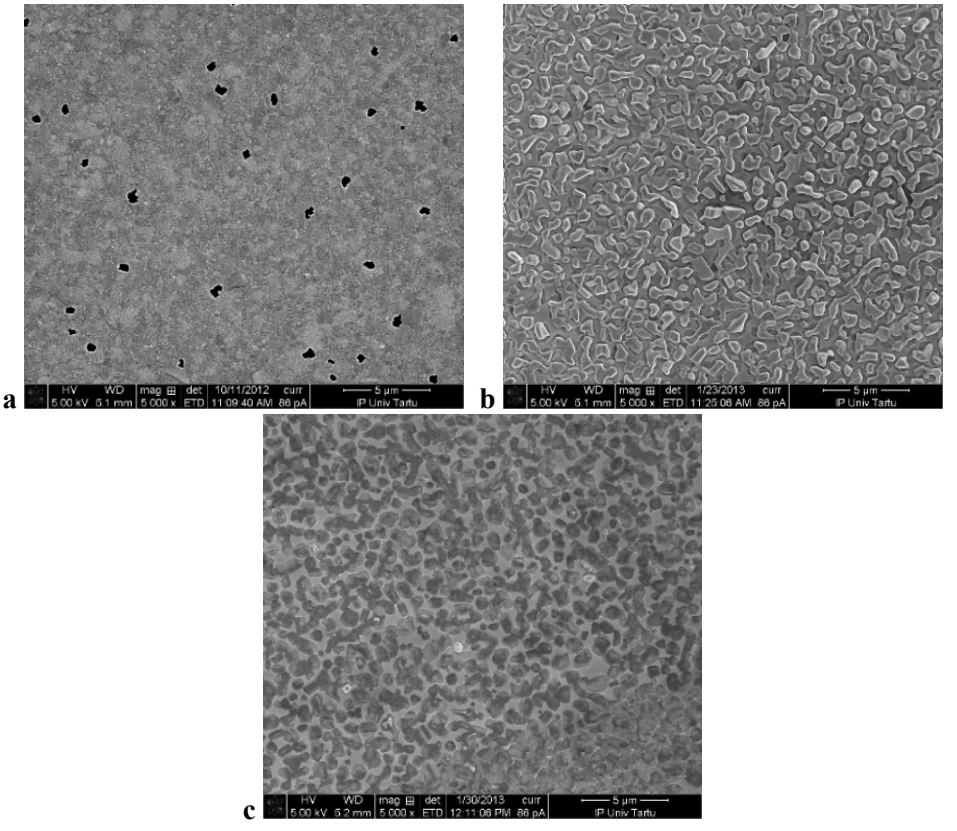

Figure 34. SEM images of (a) 80 nm and (b) 60 nm-thick Ni film after graphene synthesis; (c) the graphene sheet synthesized on 60 nm-thick Ni film after transfer to Si/SiO_2 substrate.

5.6. Performance of MLG deposited on nickel foils as electrodes for oxygen reduction

(Paper III)

5.6.1. Characterization of Nickel/CVD-grown MLG electrodes

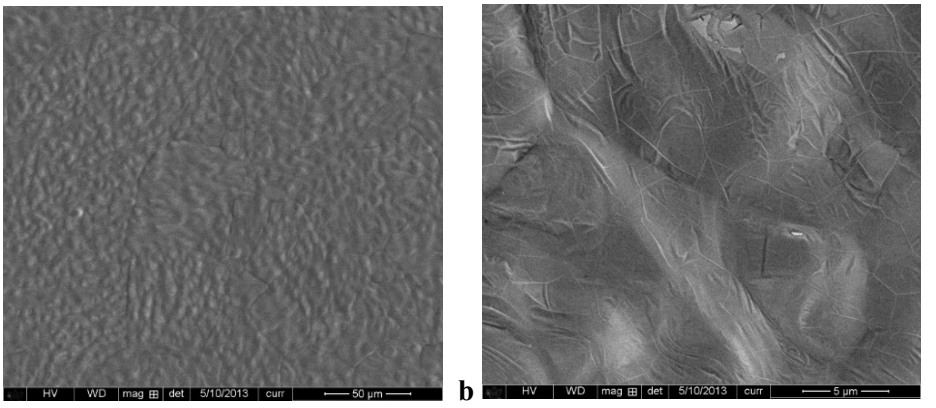

Figure 35. SEM images of the prepared nickel/MLG electrode surface. Scale bar: (a) 50 µm and (b) 5 µm.

To characterize the morphology of the CVD-grown MLG electrodes, SEM was used (Figure 35). For the synthesis of MLG to be utilized as the electrodes, the prolonged synthesis times were used to minimize discontinuities in the synthesized graphene film. As can be seen from Figure 35a, the surface shows mostly modest brightness variations, which are related to the grain boundaries and relief of the nickel grains. At a closer look (Figure 35b), the graphene wrinkles can be seen throughout the surface, making the coverage of the surface with graphene apparent. However, although small defects in MLG coverage can still be found, the vast majority of the surface appears to be covered. In order to compare the roughness of the Ni/MLG electrode with HOPG, the AFM measurements were also conducted (Figure 36). The 3D AFM images of compared electrodes show different surface morphology. The surface of HOPG is smooth, comprising of up to 2 µm wide terraces separated by steps of one to several graphene layer height. The surface of Ni/MLG electrodes is rougher (compare the dimensions of the z-scale) due to graphene wrinkles and the unevenness of the underlying nickel. The root-mean-square roughness calculated from the images shown in Figure 36 is 1.4 nm for HOPG and 81.1 nm for Ni/CVD-grown MLG electrode. The higher roughness results in the larger specific surface of the CVD-grown MLG electrode compared to the HOPG electrode with the same geometric area, which affects most electrochemical responses.

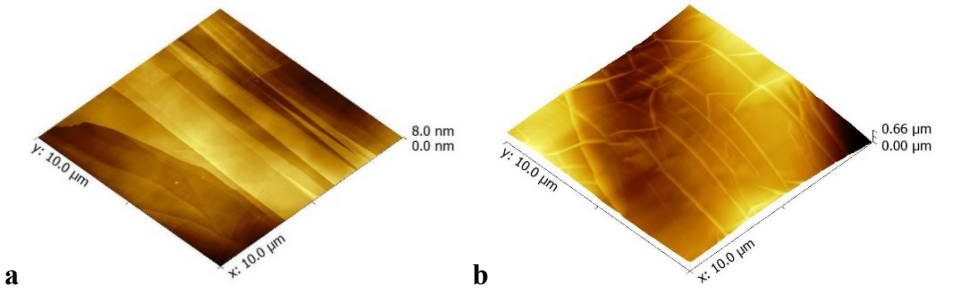

Figure 36. 3D AFM images (10 × 10 µm^2) show the surface morphology of HOPG (a) and the CVD Ni/MLG electrode (b).

The typical Raman spectra of a CVD-grown graphene film and HOPG are given for the comparison in Figure 37. Both spectra show G band and 2D band characteristic to all graphene-based materials. As expected, in both samples the intensity of the G band is higher than the intensity of the 2D band, which indicates the presence of more than one graphene layer. However, the shape of the 2D band, which is also sensitive to the number of graphene layers, differs between the HOPG and CVD-grown graphene samples. While in HOPG sample 2D band has typical graphite shoulder at a low-frequency side, the 2D band in CVD graphene sample is more symmetric. Taking into account the shape of 2D band and the value of the splitting between its most intense sub-components (Δ_{2D}=31 cm^{-1}) we concluded that the number of graphene layers in the sample is about 10, see also Figure 25 and the text describing it. The D peak was practically absent in both spectra, indicating a low amount of defects on the surface of both samples.

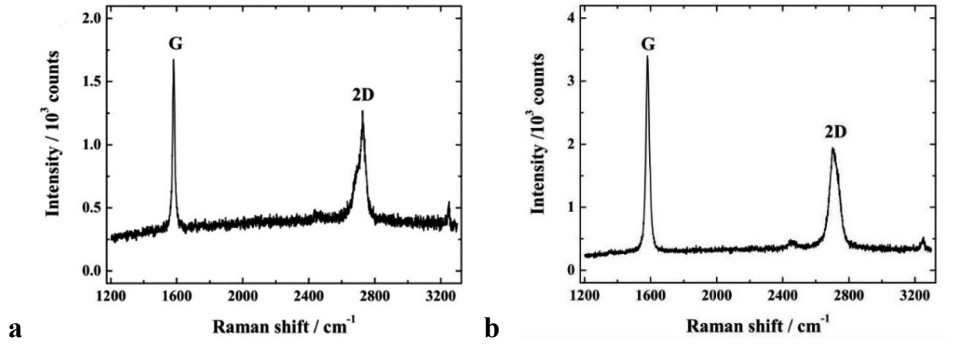

Figure 37. The Raman spectra of (a) HOPG and (b) CVD-grown MLG [III].

To evaluate the graphene coverage on the nickel foil on macro-scale, we implemented the electrochemical method proposed by Ambrosi et al. [344]. This method is based on measuring the inherent redox signals of the underlying metal catalyst. Graphene prevents the metal interaction with the external environment, thus no signal should be generated by fully covered metal. In case of partial

coverage, the electrochemical signal is dependent on the area ratio of the uncovered and covered places, reaching minimum in case of the completely covered metal electrode. The results of the cyclic voltammetry in alkaline solution for bare nickel and the Ni/MLG are presented in Figure 38 (the electrochemical measurements discussed in this and next subdivisions were done by Elo Kibena-Põldsepp). As can be seen, the redox signal generated by $Ni(OH)_2$ is greatly suppressed on Ni/MLG electrode compared to the bare nickel. This confirms that the nickel is mostly covered with graphene, however, some discontinuities are still remaining in the graphene coverage, which is in accordance with the results of our microscopy studies. The XPS measurements [IV] of Ni foil before and after the synthesis of MLG revealed that after CVD (40 min of methane exposure at 1000 °C) only the peak with a binding energy of 284.5 eV corresponding to sp^2 carbon was present in the spectrum indicating that the predominant majority of the surface was covered with graphene.

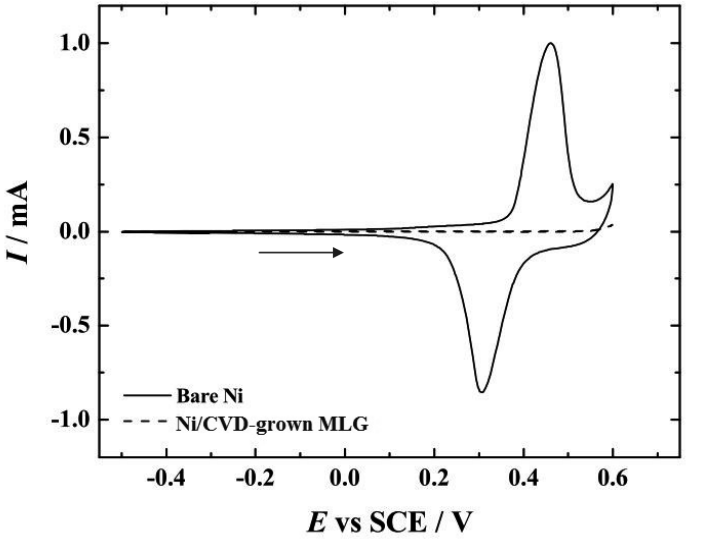

Figure 38. Cyclic voltammograms for the bare Ni and Ni/MLG graphene electrodes recorded in Ar-saturated 0.1 M KOH between –0.5 and 0.6 V (the 10th cycle is displayed). The arrow indicates the direction of the scan [III].

5.7. Electrochemical properties of CVD nickel/MLG electrodes

In order to investigate the heterogeneous electron transfer properties of the CVD-grown MLG, the cyclic voltammetric measurements were performed. The measurements were conducted in Ar-saturated 0.1 M K_2SO_4 solution in the presence of 1 mM $K_3Fe(CN)_6$ at a scan rate of 100 mV s^{-1}. Cyclic voltammetry using HOPG and GC were also performed for comparison at the same conditions.

It can be seen from the obtained cyclic voltammograms (Figure 39) that the CVD-grown MLG shows much larger peak-to-peak separation compared to GC, which is a hallmark of slow electron transfer kinetics [345]. The cyclic voltammetric response of CVD-grown MLG towards ferricyanide reduction was very similar to that of HOPG electrode. This result is following the data obtained by Ambrosi and Pumera [346] who compared electron transfer rate of MLG transferred to the polyethylene terephthalate substrate with both basal plane and edge plane pyrolytic graphite and found that the electron transfer kinetics of transferred MLG resembles that of basal plane pyrolytic graphite.

Further, the electrocatalytic activity of the CVD-grown MLG on nickel for ORR in the alkaline electrolyte was evaluated by linear sweep voltammetry (LSV). Figure 40 shows the LSVs for GC, HOPG and CVD-grown MLG in an O_2 saturated 0.1 M KOH electrolyte. As can be seen, the LSV curves of CVD-grown MLG on nickel and HOPG are somewhat similar: both show the oxygen reduction peaks at –0.8 and –1.1 V. The main difference between them is the presence of a small current peak on HOPG at ca –0.5 V. This peak is apparently due to the reduction of oxygen by oxygen containing-groups at defects and the edge sites of HOPG surface [347,348]. The peak is small since the HOPG has low-defect surface and the number of adsorption places is small. The absence of this peak on CVD-grown MLG indicates an even smaller amount of defects/graphitic edges on its surface compared to HOPG. In case of GC electrode, the reduction peaks appear at lower potentials: the first sharp, high current peak appears at –0.45 V and the second one at –0.9 V. As can be seen compared to GC both HOPG and CVD-grown MLG show rather low activity towards oxygen reduction.

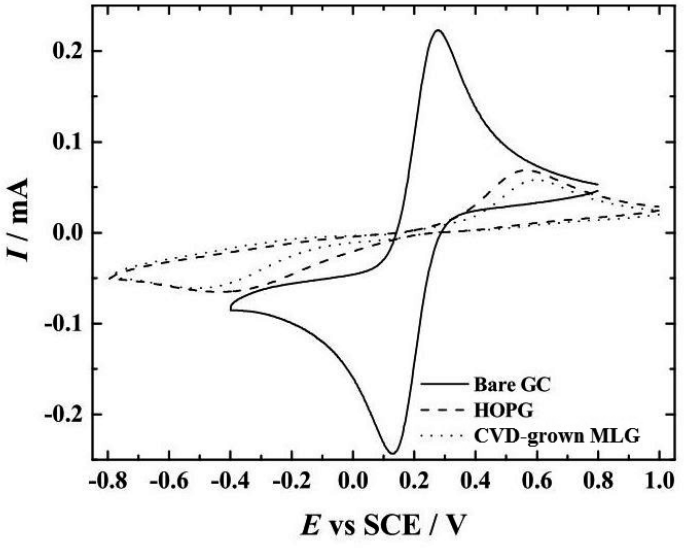

Figure 39. CV response towards the $Fe(CN)_6^{3-/4-}$ redox couple on bare GC, HOPG and CVD-grown MLG in Ar-saturated 0.1 M K_2SO_4 solution containing 1 mM $K_3Fe(CN)_6$ [III].

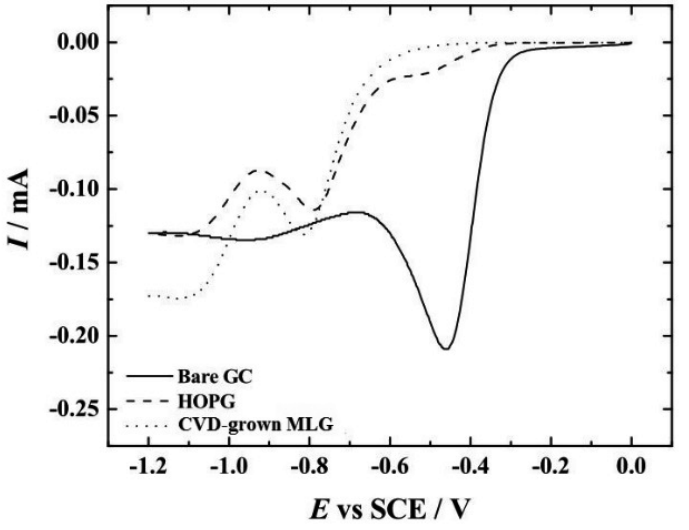

Figure 40. LSV curves of ORR at bare GC, HOPG and CVD nickel/MLG electrodes in O_2-saturated 0.1 M KOH solution (scan rate: ν = 100 mV s^{-1}) [III].

5.8. Characterization of Nickel/CVD-grown MLG modified by electroreduction of aryldiazonium salts

(Paper IV)

The changes in the morphology of nickel/MLG structures/electrodes after the electrografting process (done by Marek Mooste) were studied using atomic force microscopy in the non-contact mode (Figure 41). As can be seen, after modification, the surface exhibits fine-granular morphology, which was absent on a bare nickel/graphene electrode. The discernible increase in the diameter of the graphene wrinkles also points out on the presence of an extra layer on top of the graphene. The size of the granular formations varied depending on the modifier, which might depict the difference in the density of the primary reaction centers as well as the thickness of the deposits. The thickness of the layers was measured by AFM using nanoscratching mode of nanolithography package, i.e., removing the modification layer by repeated scanning of the chosen area in contact mode with subsequent imaging in non-contact mode. The topography profile was then extracted from the image, as demonstrated in Figure 43 on the example of Ni/MLG/NP sample. The measured thicknesses of deposits in narrow potential range varied from few (GBC) to about 12 nm (ABD). However, it was difficult to measure the thickness very precisely due to the unevenness of the underlying Ni/MLG substrate, it was apparent, that the thickness of the deposits exceeded the thickness expected for the monolayer of attached molecules. For example, whereas the height of the PhBr monolayer is 0.67 nm, the measured thickness was around 6 nm. More than eight-fold exceeding of the expected value indicates

the formation of polyaryl layer on graphene, which takes place when aryl radicals instead of attacking graphene surface, react with aryl groups already attached to graphene [349]. Alternatively, the multilayer can also form through azo linkages (in this case aryldiazonium groups attach to the aryl groups already grafted to graphene). The presence of azo linkages can be revealed by XPS due to the appearance of a characteristic peak at 400 eV in the spectrum. A 400 eV-peak was indeed present [IV] not only in the Ni/MLG/AB, Ni/MLG/GBC and Ni/MLG/FBK samples, in which attached aryl moieties contain azo group but also in the Ni/MLG/PhBr sample. The presence of a peak at 400 eV in NP-modified samples is not a reliable indicator of the azo linkage formation, because, it has been shown [350] that under the x-ray irradiation nitro groups can be converted into amino groups, the binding energy (399.6 eV) of which is very close to that of azo groups. Still, the appearance of 400 eV-peak also in the Ni/MLG/PhBr sample supports the assumption that multilayer on the Ni/MLG surface might at least partially be formed through the azo linkages.

The modification of the graphene surface with nitrophenyl groups was of particular interest because these groups are electroactive. As can be seen in Figure 42, already after one cycle the surface is covered with a continuous layer of modifiers. The AFM-measured thickness of the layer is around 5 nm (Figure 43), which translates into 7–8 nitrophenyl monolayers. Since NP groups are electroactive, it was possible to estimate the number of the attached groups from cyclic voltammetry (measured by Marek Mooste). For Ni/MLG/NP1 sample, the surface concentration was 2.3×10^{-10} mol cm^{-2}. The calculated maximum concentration of the nitrophenyl groups in a monolayer is about 7.2×10^{-10} [351], consequently, after ten cycles roughly one-third of the maximum concentration was achieved. After ten electrografting cycles with additional holding at –0.2 V for ten minutes (Ni/MLG/NP2), the granular morphology of the surface becomes even more pronounced, however, the graphene wrinkles are still can be seen underneath the organic layer (Figure 42a). The thickness measurement confirmed an increase in the layer thickness, which was estimated to be 20 nm. The estimated concentration of the NP groups, however, showed only 26%-increase compared to the grafting process without additional holding at a fixed potential sample. The thickest NP layer was obtained on the Ni/MLG surface after grafting in wider potential range (from 0.6 to –1.4 V, 1 Vs^{-1}). As can be seen in Figure 42, the graphene wrinkles are hardly discerned under the thick polyaryl layer, the thickness of which, according to AFM nanolithography results, reached 30 nm. Surprisingly, the surface concentration of NP molecules did not change compared to Ni/MLG/NP2. This may indicate the formation of the NP-layer with lower density. However, there is a possibility that some nitrophenyl groups in the film are not electroactive, possibly because in the thick film, the most inner groups are hard to reach for the electrolyte [352].

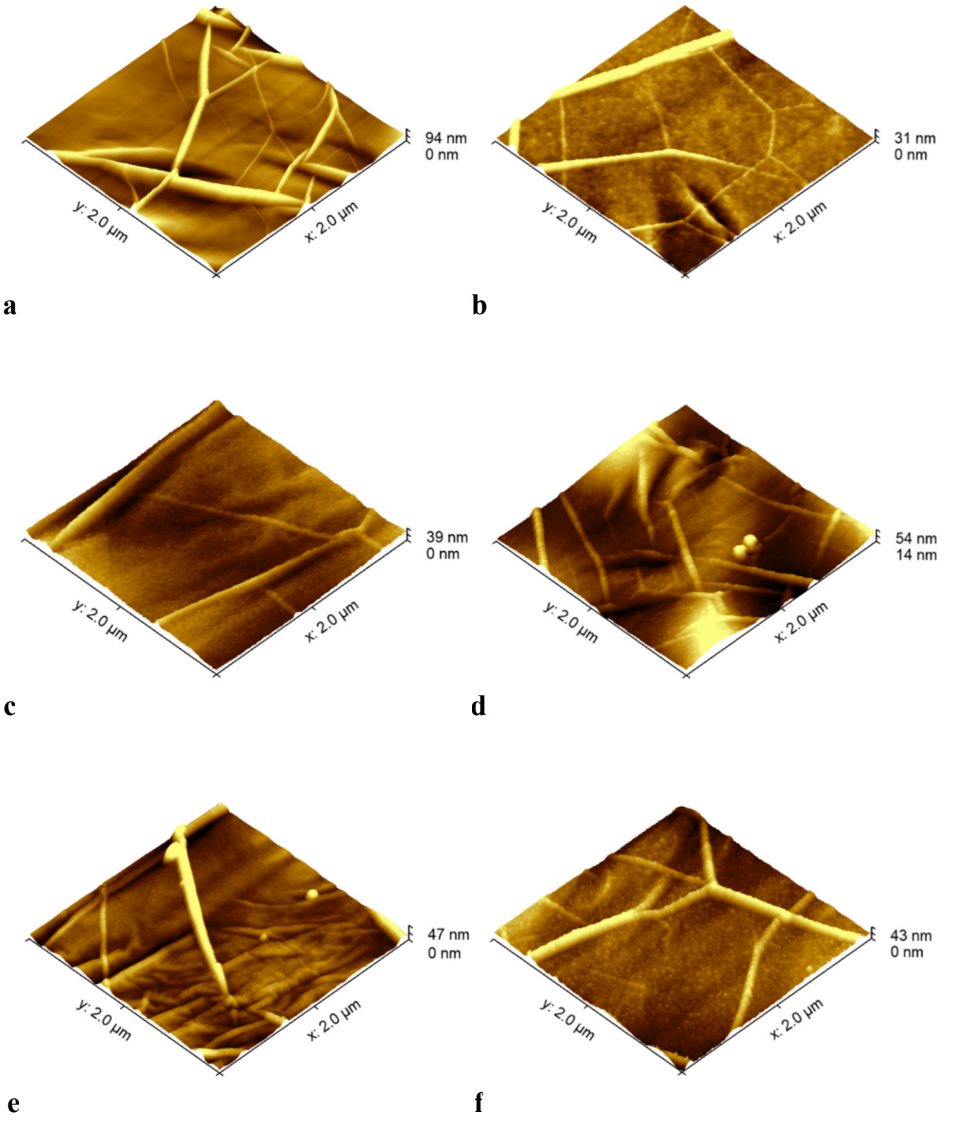

Figure 41. AFM images of bare Ni/MLG (a) and Ni/MLG/AB (b), Ni/MLG/GBC (c), Ni/MLG/FBK (d), Ni/MLG/PhBr (e) and Ni/MLG/NP1 (f) groups.

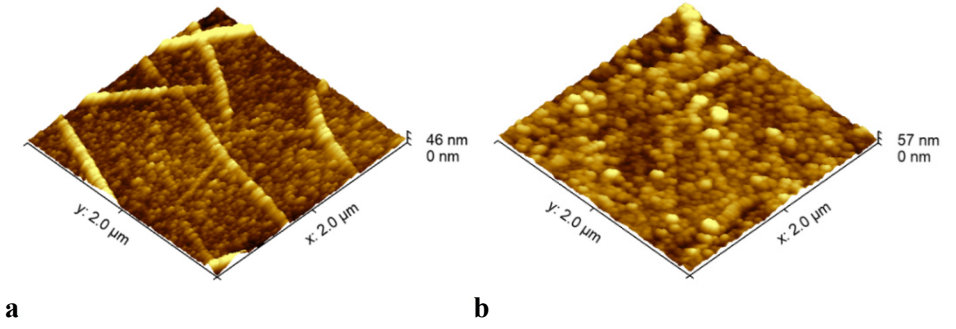

Figure 42. AFM images of Ni/MLG/NP2 (a) and Ni/MLG/NP3 (b).

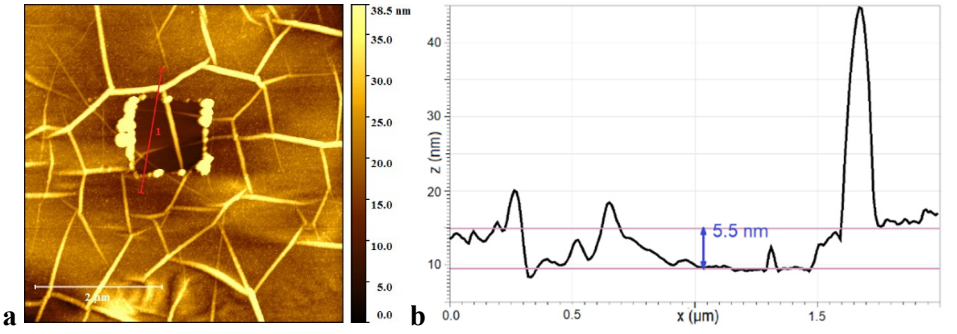

Figure 43. NCAFM image showing the cavity in the arylmodified film, obtained by the repeated scanning in the contact mode (b). A topographic line profile acquired at the location shown in (a).

According to the proposed mechanism (Figure 10) aryl radical attaches to graphene and a covalent bond is formed between carbon in the graphene lattice and the aryl group. A formation of a covalent bond requires a change in the hybridization of a carbon atom from sp^2 to sp^3 and should thus be reflected in the Raman spectrum of functionalized graphene samples. Figure 44 shows the Raman spectra of CVD-grown MLG after electrochemical grafting with aryl diazonium salts. As can be seen, after the grafting process the G and 2D band are still present in the spectra without significant changes in their widths or spectral positions. Small variations in the shape and intensity of the 2D band are related to the fact that spectra before and after electrochemical modification have been performed on the MLG areas with slightly different amount of stacking disorder (as it was challenging to measure on precisely the same area), and should not be taken into account. Some minor increase in the intensity of the Raman signal can be discerned at ca 1400 cm^{-1} and 1440 cm^{-1}, which corresponds to N=N bond stretch in aryl-substituted azo compounds, as well as around 1332 cm^{-1}, which is likely due to C-NO_2 bond stretch [353]. The most noteworthy changes, however,

can be discerned in the spectral range of D band. The most intense D band is observed in the Ni/MLG/PhBr spectrum, while the only slight increase is visible after electrografting with other diazonium salts. The appearance of D band has already been reported in the literature after spontaneous grafting of micro-mechanically exfoliated [354] and CVD-grown [355] single-layer graphene as well as after electrochemical functionalization of micromechanically exfoliated graphene [27] with aryldiazonium salts. The appearance of the D band is well coherent with the expected increase in the number of sp^3-hybridized carbon atoms. The highest number of sp^3-hybridized carbon atoms obtained in Ni/MLG/PhBr sample could indicate that towards graphene, the bromophenyl radical was the most reactive. However, it should be noted, that even for PhBr-modified graphene the D band intensity was rather low, not exceeding the 20% of the G band intensity. This can be explained by a higher number of graphene layers in the studied sample. During electrochemical grafting, only top graphene layer is exposed and subjected to modification by aryldiazonium moieties, whereas lower layers remain intact and do not add to the intensity of the defect peak. Moreover, it has been shown [356] that SLG regions of micromechanically exfoliated graphene showed an increased reactivity compared to the bilayer and MLG regions. This by the authors' opinion is due to the fact the top layer in bilayer and MLG is not in contact with the charged impurities in the substrate and thus does not encounter the charge fluctuations that might lead to increased reactivity. Therefore, it might be reasonable to compare the modification of MLG with the modification of the HOPG that has been a subject of research interest even before graphene came into play. The reported Raman spectra of HOPG after modification also show a D band, but its intensity is usually low [357–359]. For example, after the modification of HOPG using 4-carboxybenzenediazonium tetrafluoroborat [357] the ratio of intensities of the D and G bands, I_D/I_G did not exceed 0.07. An even smaller value of (I_D/I_G=0.006) was obtained after grafting of NBD on HOPG from a 1 mM solution of 4-NBD [359]. In comparison, after the modification of CVD-grown SLG under the same modification conditions, the D band intensity was markedly higher (I_D/I_G= 1.14) [359]. Thus, relatively small increase in the D band intensity in case of MLG is explicable.

Some researches, however, hold the opinion, that there is not enough evidence for the covalent bond formation between aryl layer and the basal plane of HOPG. Ma et al. [358] obtained the atomic resolution images on the surface of the HOPG after removal of the electrografted aryl layer and found that it is rather undistinctive from pristine graphite. Based on this observation as well as that, aryl layer is relatively easy disrupted by STM tip, they concluded that the aryl layer is only physisorbed on the HOPG. In order to clarify, whether the reaction between aryl radical and a basal plane of graphene might or might not take place, Jiang et al. conducted the first-principle density functional theory calculations [360]. They showed that the energy gain of the attachment of the aryl group to the defect-free basal plane of graphene is very small and that the physisorption is most likely. However, the attachment of the second group to the same graphene hexagon is already much more energetically favorable. Thus, the covalent

attachment of aryl radicals to graphene/graphite is possible if there occur some defect sites or edges (what is the case of real surfaces), where the first aryl radicals can bond.

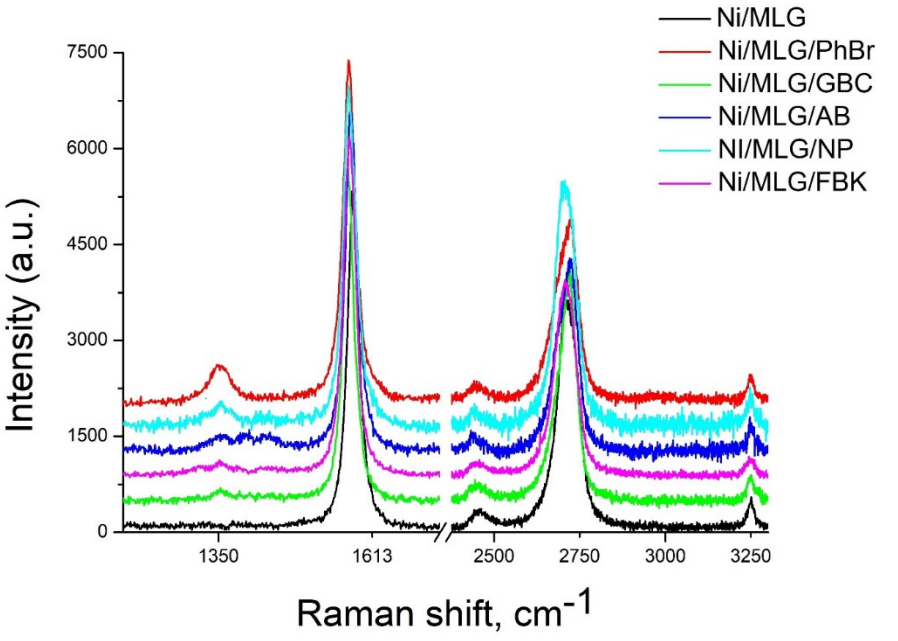

Figure 44. The Raman spectra of Ni/MLG after modification via electrochemical reduction of various aryldiazonium salts. For better comparison, the spectra are normalized by the intensity of G band.

However, the AFM and Raman measurements demonstrated that modification of the graphene surface after electrografting took place, it cannot be clearly stated whether the aryl layer is physisorbed or covalently attached to the graphene layer. In one respect, the formation of a covalent bond between graphene and aryl groups is desirable, because it ensures stable attachment of the functionalization layer, but, on the other hand, disruption of sp^2-conjugated graphene network inevitably affects graphene electronic properties. If the preservation of graphene electronic properties is of the uppermost importance than the noncovalent functionalization would be preferential.

5.9. Atomic layer deposition on graphene

5.9.1. Atomic layer deposition on graphene prepared by micromechanical exfoliation method

(Paper V)

For the deposition of the HfO_2 layers on graphene three different regimes were used. The most uniform oxide layers were obtained when the ALD process was carried out at a low temperature of 180 ºC, and the measured Root Mean Squared (RMS) roughness was about 0.5 nm (Figure 45). This value is only slightly higher than the RMS roughness of the oxide on the surrounding SiO_2. The HfO_2 layers grown at low temperature were amorphous. As the previous studies have shown that HfO_2 deposited at low temperature has a relatively low dielectric constant [361] and a high concentration of hydrogen and chlorine impurities [318,361], it was desirable to increase the deposition temperature. The HfO_2 layers grown at the higher temperature of 300 ºC had monoclinic structure, but the growth was nonuniform, and the surface of these layers was rough, with an RMS value of about 5 nm (Figure 46). The HfO_2 grown on SiO_2 exhibited much smoother morphology, and its RMS roughness was roughly two times lower. Initiating the growth of the oxide layer at low temperature and continuing at higher temperature yielded the HfO_2 layers with more uniform morphology in comparison to layers deposited at only at 300 ºC, but their roughness was considerably higher compared to the HfO_2 layers grown at low temperature, being about 2.5 nm (Figure 47).

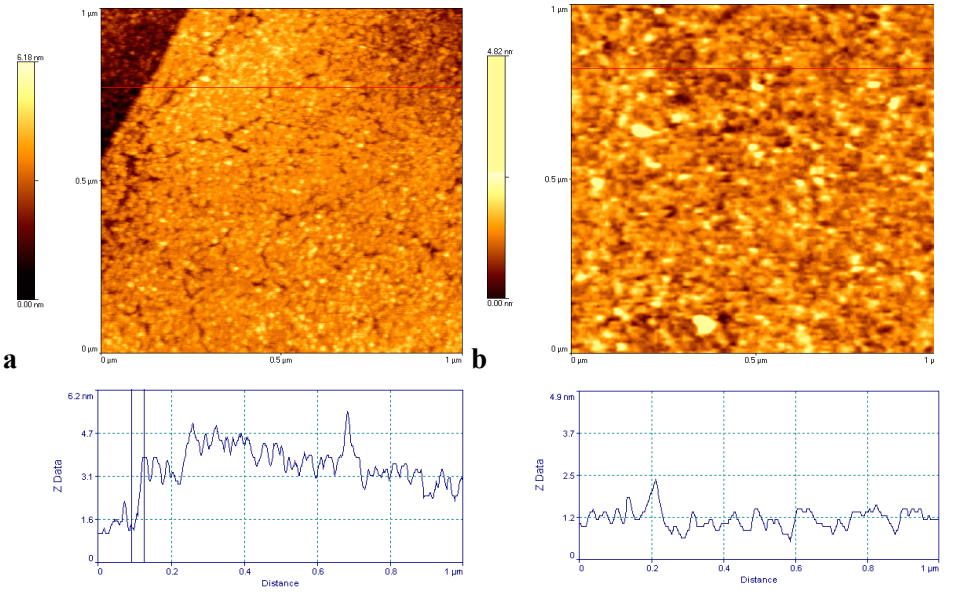

Figure 45. HfO_2 films deposited at 180 °C on: (a) graphene (RMS-r = 0.5 nm), (b) on SiO_2 (RMS-r = 0.3 nm); scanning area 1×1 μm^2.

The RMS roughness of the oxide on the surrounding SiO_2 was, however, also higher, about 2 nm, which indicates that the higher roughness of HfO_2 deposited on graphene at the two-temperature process was primarily due to crystalline structure [V] of the oxide layer, not the nucleation problems.

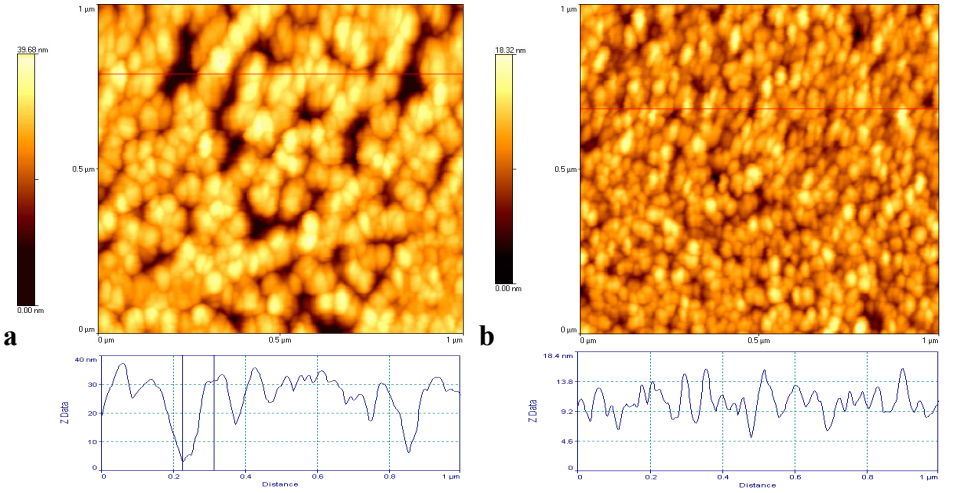

Figure 46. AFM images of of HfO_2 films deposited on (a) graphene (RMS-r = 5.4 nm) and (b) silicon dioxide (RMS-r = 2.6 nm) at 300 °C and height profile, scanning area 1 × 1μm^2.

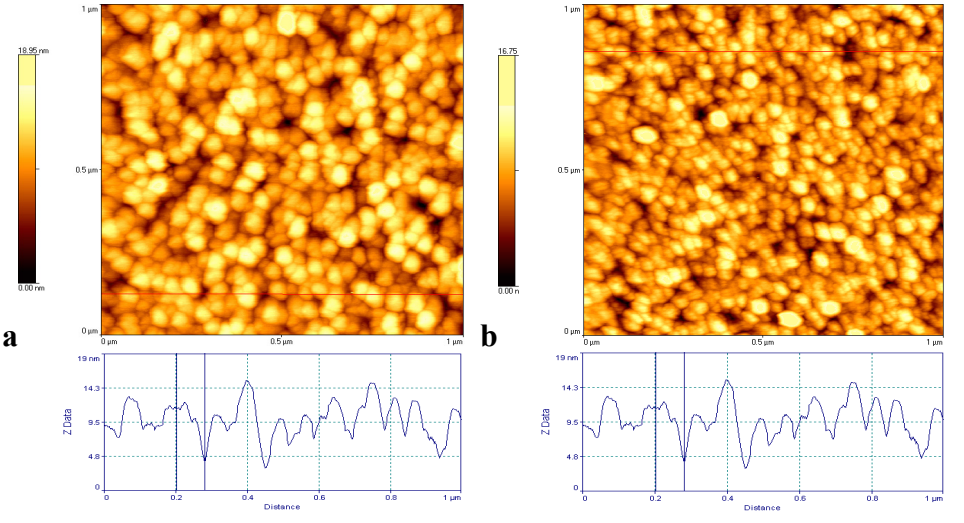

Figure 47. AFM images and height profiles of of HfO_2 films deposited in the two-temperature (170/300 ºC) growth process on (a) graphene (RMS-r = 2.5 nm) and (b) silicon dioxide (RMS-r = 1.96 nm), scanning area 1 × 1μm^2.

The Raman spectroscopy studies (Figure 48) indicated that the ALD of HfO_2 did not generate defects in graphene as there was no visible increase in the intensity of D the band. While the modification of the graphene did not cause any structural changes in the graphene layers, the noticeable lattice strains were induced. The compressive straining of the lattice is indicated by the blueshift of the 2D band and the G band relative to the positions of the bands before the deposition of HfO_2 by 22 and 9 cm^{-1}, respectively. The conclusion that the compressive strain and not the doping was responsible for the blueshift of the bands was made based on the characteristic to the compressive strain two-times greater shift of the 2D band compared to the shift of G band [236] as well as the absence of the doping-related narrowing of the G band [237].

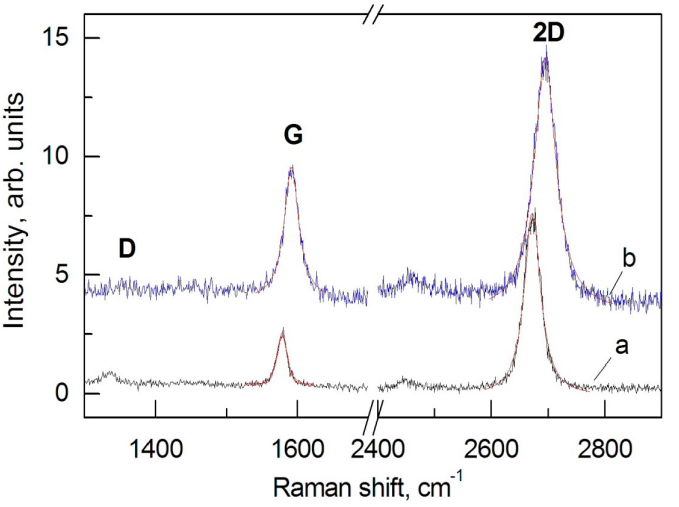

Figure 48. Raman spectra of graphene: (a) before and (b) after ALD of HfO_2 thin film in the two-temperature (170/300 ºC) growth process.

5.9.2. Atomic layer deposition on graphene prepared by CVD method (Paper VI)

Graphene prepared by micromechanical exfoliation provided only a very limited area for observation of the growth of the dielectric film. Besides, it was required to study ALD on graphene prepared by the method, which has a potential for graphene production on the industrial-scale. Due to the large area of graphene synthesized by CVD, it also became possible to cover the QCM mass sensor with graphene and conduct in situ QCM measurements. The change in the resonant frequency of the QCM crystal is directly related to the change in the crystal mass, and thus, monitoring it during the ALD process allows gaining deeper insight into film growth. The deposition parameters were chosen based on previous QCM studies [319] of ALD of ZrO_2 conducted in the same reactor. Prior to the ALD on graphene covered surfaces the appropriate doses of $ZrCl_4$ and H_2O were

determined by recording the QCM sensor signal as a function $ZrCl_4$ pulse duration and then, as a function of H_2O pulse duration [VI].

The surface morphology after deposition of ZrO_2 by ALD at 190 °C was characterized by SEM, as illustrated in Figure 49. Figure 49a shows a surface of graphene-covered QCM sensor after deposition of ZrO_2. It can be seen, that the deposited layer is not completely uniform, however, the relatively uneven surface of the mass sensor creates rather strong topographical contrast, that obscures the surface topology of the deposited layer. The deposited layer of ZrO_2 can be discerned more clearly on the bare (Figure 49b) and graphene-covered (Figure 49c,d) Si/SiO_2 substrates. In contrast to the continuous and compact layer of ZrO_2 grains on bare Si/SiO_2, the layer deposited on graphene presents rougher and non-uniform morphology. It can be clearly seen that on graphene covered substrates, the continuous layer is not achieved regardless of the precursors' pulse lengths used. After ALD with shorter pulses on graphene transferred from nickel film, the uncovered areas reached few hundreds of nm in some places. Conversely, some neighboring areas on the same substrate were more densely covered, but even in these areas complete coalescence of the islands grown from individual nucleation centers has not occurred as some trenches in the ALD film were clearly seen. The images visualize directly that nucleation sites are significantly less abundant on graphene compared to Si/SiO_2 surface and that their number varies on the surface significantly. The difficulty in nucleation has been unambiguously demonstrated by real-time QCM technique, which showed a nucleation delay period of 5–10 cycles at shorter precursor pulses [VI]. The sparseness of the nucleation centers manifests itself also in the visibly larger crystalline sizes on graphene covered areas, as the reaction of precursors with nucleated ZrO_2 is more favorable compared to the reaction with a graphene surface. Consequently, as the regions of ZrO_2 are very limited at initial growth periods, one might expect a very small recorded mass increase on graphene-covered QCM sensor compared to the uncovered one. After 10 cycles, the QCM frequency change per cycle of graphene covered sensor was less than 1 Hz, compared to 13 Hz-change on the surface without graphene. Even after 100 cycles the frequency change per cycle for 2-2-2-5 s cycle on graphene covered surface reached only 65% of the frequency change per cycle on QCM surface without graphene. The nucleation delay was reduced when longer (5-2-5-10) pulse lengths were used [VI], which resulted in more than 30%-increase in the frequency change per cycle compared to the process with shorter pulse lengths. However, as can be seen from the SEM image (Figure 49d), the deposited layer is obviously still discontinuous.

From a cross-section of the sample it can be seen (Figure 50c), that the thickness of the ZrO_2 deposited using longer cycles is overall larger compared to the film deposited on graphene using shorter cycle times (Figure 50b), reaching in some places the thickness of the film deposited on the bare Si/SiO_2 substrate (Figure 50a), which was estimated to be ≈24 nm. The uniformity of the thickness of the film deposited on graphene was however significantly inferior compared to the film on bare Si/SiO_2 substrate. Noteworthy, the continuous layer of HfO_2 deposited on mechanically exfoliated graphene [V] was achieved already for 11

nm-thick films. It is known, however, that in terms of structural quality the exfoliated graphene is superior to CVD-synthesized graphene, and thus the opposite behavior would be expected. The reason for the better coverage achieved on the exfoliated graphene could be due to lower purity of the surface of the exfoliated graphene. Whereas efforts were undertaken to ensure that the transferred graphene is free from PMMA residues, the exfoliated graphene was used in the as-cleaved state, and could possibly be contaminated by the glue from the Scotch tape. Another reason could be the slightly higher temperature used to deposit ZrO_2 (190 °C) compared to the temperature used to initiate the growth of HfO_2 layer on the exfoliated graphene (170 °C).

It can also be assumed that the high nonuniformity of the ZrO_2 growth is a result of the graphene transfer procedure. For example, the areas covered with PMMA residues, contaminated from etchant or received some structural damage are expected to have a higher number of nucleation sites, which will result in better coverage compared to pristine graphene sheet. For that reason, the ZrO_2 deposition was also carried out on the "as-synthesized" graphene on copper foil and nickel film substrates. For a valid comparison, the ALD was conducted on the same graphene-covered foil/film, parts of which were used for obtaining transferred graphene samples mentioned above. The resulting ZrO_2 films on non-transferred graphene (Figure 51) show similar trend as the ZrO_2 films on graphene before transfer, i.e., the film is discontinuous, and the coverage density varies significantly over the substrate, which indicates that the considerable variation of the nucleation density on the graphene is not a result of the transfer procedure. It can be speculated that the observed behavior is related to the variation of the graphene physisorption strain. It has been shown that the applied strain to graphene enhances its reactivity [355]. The strain levels can differ depending on the crystallographic orientation of the underlying metal surface [362] or conformity of the transferred graphene to Si/SiO_2 substrate. Considering that graphene synthesized on nickel compared to copper is significantly stronger bound to the catalyst [II], the effect of the substrate on the ALD for nickel is expected to be more pronounced. In addition, in case of graphene synthesized on nickel films, the variation in the film density over a graphene sheet might be a result of variation in the number of graphene layers as the thicker areas might be less affected from the substrate and as a result, be less reactive. Furthermore, as the growth of graphene layers also strongly depends on the orientation of the nickel grains [I], the grains with deficient graphene coverage would be better covered with ZrO_2 layer.

The Raman spectroscopy measurements were performed to determine the effect of the ZrO_2 deposition on graphene. As has been demonstrated in [VI] the graphene's characteristic bands were present in Raman spectra after graphene transfer from both nickel films and copper foils confirming, that graphene transfer was successful. The 2D and G bands were well discerned in the spectra also after ALD deposition with both shorter and longer cycle times, indicating that no dramatic changes were introduced to the graphene structure. The strong scattering from the mass sensor electrodes, however, hindered in-depth analysis of Raman

spectra of graphene before and after ALD deposition. To gain a more detailed insight on the changes introduced to graphene by ALD, the Raman spectra were also recorded from graphene transferred to the Si/SiO_2 substrates, which were covered with ZrO_2 layer simultaneously with the mass sensors.

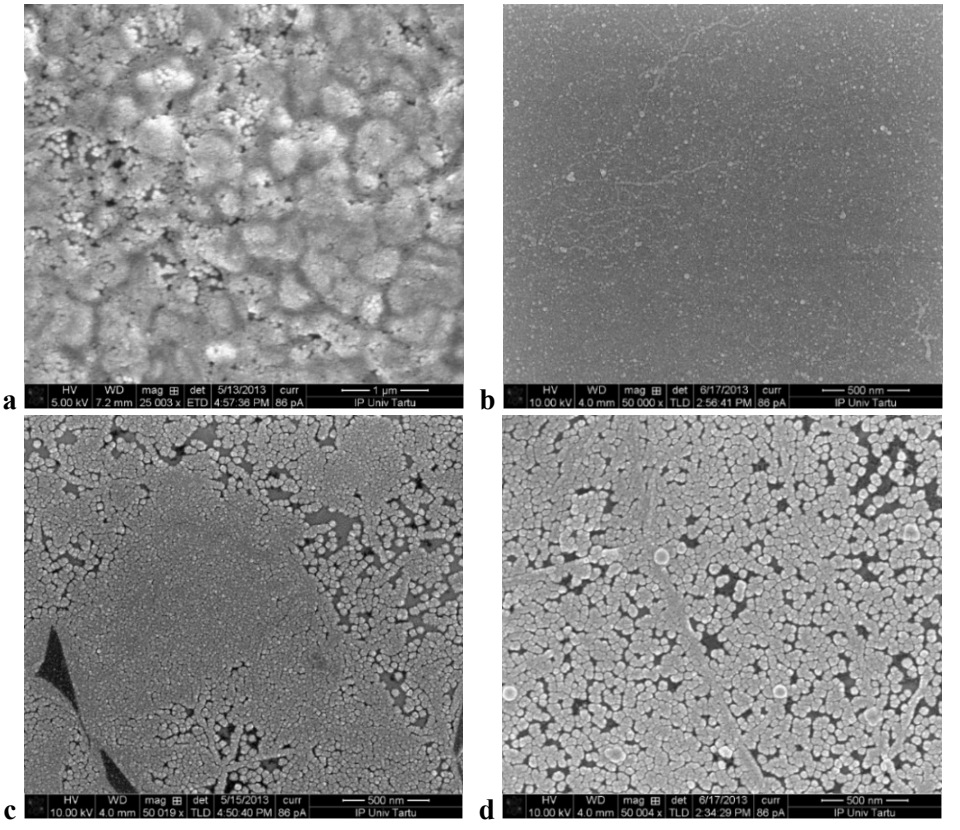

Figure 49. SEM images of (a) the QCM sensor, (b) Si/SiO_2 substrate, (c) graphene transferred from Ni-film to Si/SiO_2, (d) graphene transferred from copper-foil to Si/SiO_2 substrate after deposition of ZrO_2 using 100 ALD cycles. The cycle times were (a–c) 2-2-2-5 s, and (d) 5-2-5-10 s.

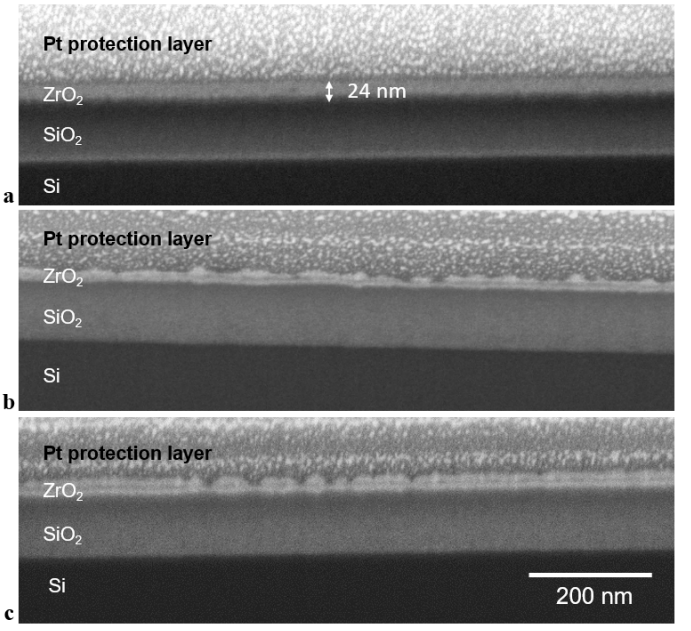

Figure 50. Cross-sectional SEM images obtained after ALD of ZrO_2 on (a) a bare Si/SiO_2 substrate, (b) Si/SiO_2 substrate covered with graphene transferred from nickel films, (c) Si/SiO_2 substrate transferred from copper. The cycle times were (a–b) 2-2-2-5 s, and (c) 5-2-5-10 s.

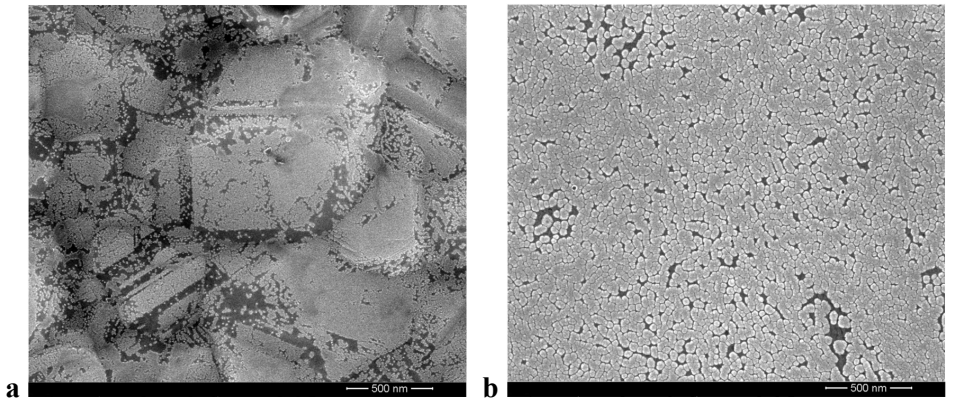

Figure 51. SEM images of ZrO_2 deposition after 100 ALD cycles on (a) FLG on Ni film (cycle times 2-2-2-5 s), and (b) SLG on copper foil (cycle times 5-2-5-10 s).

Figure 52 presents Raman spectra before and after ZrO_2 deposition with cycle times 5-2-5-10 s, on graphene transferred from copper foil. The spectrum before deposition features the G band at 1587 cm^{-1} and the 2D band at 2684.9 cm^{-1}. The 2D band has a single Lorentzian profile and is roughly 3.6 times more intense than the G band– both are hallmarks of SLG. As has been shown above, the high I_{2D}/I_G ratio as well as single-Lorentzian profile of 2D band can be present even in multilayer graphene, if the layers are misoriented with respect to one another, but in this case the G band is redshifted and the 2D band is blueshifted compared to the position of these bands in SLG. The positions of the bands are well in accordance with the position of the bands reported for CVD synthesized SLG transferred to Si/SiO_2 substrate [336]. It should be noted, that positions of the G and 2D bands are upshifted in comparison with mechanically exfoliated SLG, which is believed is due to be due to p-doping from the contact with water as well as PMMA during transfer process [336]. The widths of the G and 2D bands were 19.8 cm^{-1} and 36.2 cm^{-1}, respectively, somewhat higher than the values reported for SLG (≈15 cm^{-1} and ≈30 cm^{-1}, respectively). The small increase of the linewidth of the bands can be a sign of the slightly increased disorder. This was partially confirmed by the presence of low-intensity D band. The broadened linewidth of the bands can be due to strain variation in graphene within the laser spot area [363] as well as due to contaminants from the transfer process [364].

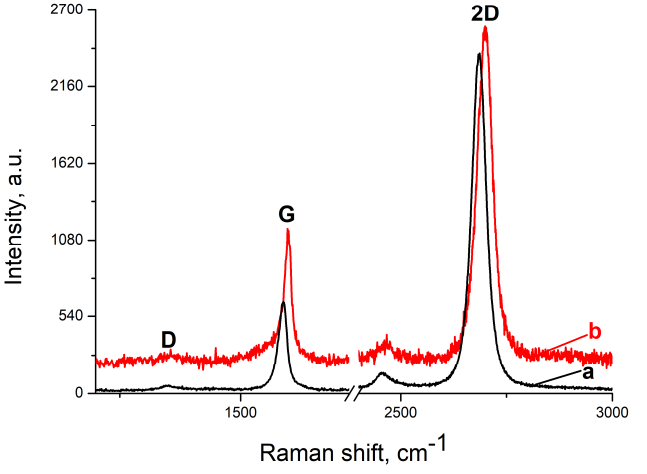

Figure 52. Raman spectra of graphene transferred from copper: (a) before and (b) after ALD deposition of ZrO_2. The spectra were normalized by the intensity of the 2D band.

After deposition of ZrO_2, the most noticeable change in the spectrum is the blueshift of the G and 2D bands by 10.1 cm^{-1} and 14 cm^{-1}, respectively. The blueshift of both the G and 2D bands indicates p-doping and/or compressive strain of a graphene sheet. It has been shown that the G band is more sensitive to doping [245], and the 2D band is more sensitive to strain [236]. By taking into account the significantly larger shift of the 2D band compared to the G band, it can be concluded that the shift of the bands is mainly a result of compressive strain. This is in accordance with the results obtained after deposition of HfO_2 on mechanically exfoliated graphene [V]. It should be noted, that with the increasing strain the upshift of the 2D band is roughly two times the upshift of the G band [236]. Here, the $\Delta\omega_{2D}/\Delta\omega_G$ of 1.4 could indicate that though the strain contribution is more significant, the smaller contribution from p-doping could also be present. The increase of charge carrier concentration should also manifest in the change of relative intensity of the G and 2D bands, as the intensity of the 2D band decreases with both hole and electron doping. Indeed, the intensity ratio of the 2D band to G band dropped to ≈ 2.5, indicating an increase in hole doping. However, no significant decrease of the G band linewidth, which usually accompanies the shift of G band in the case of doping, was observed in the sample. This can be attributed to the fact, that doping-related narrowing of the band competed with the disorder-induced band broadening. On the increased amount of disorder denotes a slight (1.8 cm^{-1}) broadening of the 2D band after ALD process. Most probably, the small increase in a disorder is a result of the increased local strain variation in graphene due to the reduction of the distance between graphene and substrate as the water molecules trapped there during transfer procedure are removed after heat treatment accompanied the ALD process.

Most importantly, the D band intensity is not increased after the ALD process, confirming the results obtained on mechanically exfoliated graphene, namely, the water-based ALD process does not create defects in the graphene lattice. A similar trend was also observed after ZrO_2 deposition on graphene transferred from nickel film (Figure 53). The effect of the deposition on the doping and strain levels of graphene grown on nickel film was more difficult to evaluate because of inhomogeneity of the graphene thickness, which varied principally between 1–3 layers over the sample. The variation in the number of layers affected the position of the G and 2D bands considerably obscuring strain and doping-related frequency shifts. The graphene synthesized on nickel film initially had higher I_D/I_G ratio indicating a higher number of structural defects compared to the graphene synthesized on copper, but again no additional defects were formed during the deposition process. The more abundant defects in graphene synthesized on nickel films is apparently a reason why the zirconia crystallites are smaller in size compared to graphene synthesized on copper foils, where due to lower defect density, the nucleation density is also lower allowing the crystallites to grow wider.

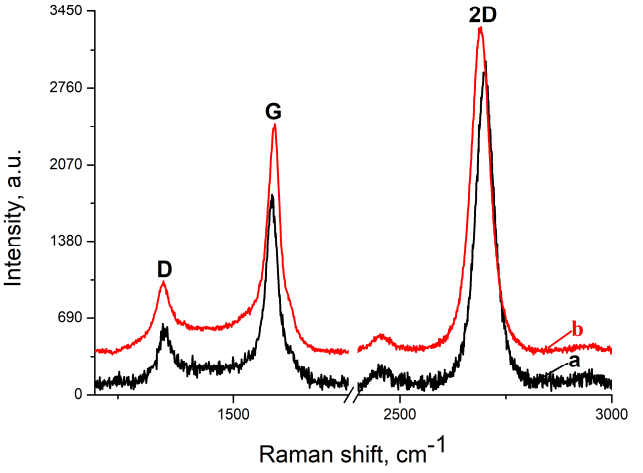

Figure 53. Raman spectra of graphene transferred from nickel film: (a) before and (b) after ALD deposition of ZrO_2. The spectra were normalized by the intensity of the 2D band.

CONCLUSIONS

In this study pristine and functionalized FLG- and MLG-based structures were prepared and characterized using various spectroscopy (EDX, EBSD, XPS, μRaman) and high-resolution microscopy (HR-SEM and FIB, HR-TEM, STM) methods.

First, the synthesis of FLG and MLG by CVD on Ni catalyst has been introduced. The synthesis has been conducted on both Ni-foils and thin Ni-films and the properties of the prepared graphene sheets have been compared with the SLG obtained by either CVD or micromechanical exfoliation of natural graphite. The peculiarities of graphene synthesized on Ni by CVD are as follows:

- Decreasing the thickness of nickel films allows reducing the amount of dissolved carbon in them and through this the number of obtained graphene layers.
- The growth of graphene on polycrystalline nickel substrates is dependent on the surface orientation of the nickel grains. As a result, areas uncovered by graphene might still be present on the nickel substrate while the majority of the substrate is already covered with MLG.
- MLG synthesized on polycrystalline nickel is characterized by a variety of stacking order between the graphene layers presented in the sheets. Moreover, the Bernal-stacked and rotationally faulted graphene layers could coexist in the same domain.
- If the rotation angles in synthesized MLG are larger than the critical angle (~13°), the Raman spectrum even of MLG becomes similar to the spectrum of SLG, showing narrow symmetrical 2D band, the intensity of which is noticeably higher than that of G band. This demonstrates that the conclusion on the number of graphene layers in the synthesized graphene samples cannot be made only based on these spectral features alone.
- There is a relationship between the rotational disorder of graphene layers and the surface orientation of the nickel substrate. This holds promise by using a substrate with favorable orientation (roughly between (001) and (111)) for synthesizing MLG with rotational disorder over a whole substrate, which is of great interest because it might exhibit charge transfer properties similar to SLG.
- MLG growth on polycrystalline nickel substrate is accompanied by pronounced morphological changes of the nickel substrate, which should be taken into account while elaborating graphene synthesis on nickel.

Further, the electrochemical properties of the synthesized MLG sheets on nickel have been tested and the possibility of their subsequent functionalization using electroreduction of various diazonium salts has been examined:

- The CVD-grown graphene on nickel can be used as electrochemically passive supporting material for exploring new electro-catalytically active materials. The use of the CVD-grown MLG for this purpose is advantageous because significantly larger samples can be obtained, and the manufacturing costs are much lower than for high-grade HOPG crystals with the same surface area.
- The surface of the CVD-grown graphene can be modified with aryl groups using electrochemical reduction of diazonium salts without the need to transfer graphene sample to another substrate.

Finally, the feasibility of the chloride-water ALD of gate dielectric of a transistor structure on top of non-functionalized graphene has been studied:

- The two-temperature process, where the growth is initiated at low temperature and proceeded at the higher temperature has been demonstrated to be advantageous for the obtaining the dielectric film of higher quality. Still, as has been demonstrated by in situ QCM measurements even at low temperature (190 °C) there is a delay in the nucleation of the oxide layer on graphene, making it much more challenging to achieve growth of continuous oxide layer.
- The latter is caused by the facts that the nucleation sites are not only at deficit on graphene but their density varies on the surface considerably as well.
- The deposition of dielectric films with the chloride-water ALD processes leads to a compressive strain of graphene but does not generate structural defects in the honeycomb lattice.

SUMMARY IN ESTONIAN

Grafeenil põhinevate struktuuride kompleksne nanoskoopiline karakteriseerimine

Antud doktoritöö raames valmistati ja karakteriseeriti puhtal ja funktsionaliseeritud kujul mõne- ja mitmekihilisel grafeenil põhinevaid struktuure, kasutades erinevaid spektroskoopia (EDX, EBSD, XPS, μRaman) ja kõrglahutusmikroskoopia (HR-SEM pluss FIB, HR-TEM, STM) meetodeid.

Esiteks, juurutati mõnekihilise ja mitmekihilise grafeeni süntees keemilise gaasifaasis sadestamise (CVD) meetodil nikkelkatalüsaatoril. Süntees viidi läbi nii nikli fooliumitel kui ka õhukestel sadestatud kiledel, ning valmistatud grafeenikihtide omadusi võrreldi grafiidi mikromehhaanilise lõhestamise teel või CVD meetodil saadud ühekihilise grafeeni omadustega. Nikkelkatalüsaatoril CVD meetodil sünteesitud grafeeni eriomadused on järgmised:

- Nikkelkilede paksuse vähendamine võimaldab vähendada neis lahustunud süsiniku kogust ja selle kaudu vähendada sünteesitavate grafeenikihtide arvu.
- Polükristallilistel nikkelalustel sõltub grafeeni kasv nikli kristalliitide orientatsioonist. Selle tagajärjel võivad mõned aluse alad jääda katmata isegi siis, kui suurem osa sellest on juba kaetud mitmekihilise grafeeniga.
- Polükristallilise nikli pinnal sünteesitud mitmekihilise grafeeni kiles esinevad grafeeni monokihtide erinevate pakmetega alad. Seejuures saavad ühes mitmekihilise grafeeni domeenis eksisteerida koos nii korrapärase Bernal'i, kui rotatsioonilise korrapäratu pakmega kihtide alad. Need viimati mainitud alad olidki enamlevinumad.
- Kui pöördenurk grafeenikihtide vahel on suurem kui kriitiline nurk (~13°), siis ilmneb mitmekihilise grafeeni ramanhajumise spektris kitsas ja sümmeetriline 2D riba, mille intensiivsus ületab märgatavalt G riba intensiivsuse. Sellised G ja 2D ribad on teatavasti iseloomulikud ühekihilise grafeeni spektrile. Seega ei tohiks hinnata grafeeni näidistes monokihtide arvu üksnes G ja 2D ribade põhjal.
- Kihtide rotatsioonilise korrapäratuse ja nikli kristalliitide orientatsiooni vahel on olemas seos. See lubab sobiva orientatsiooniga (ligikaudu (001) ja (111) vahel) aluse kasutamisel sünteesida laiapinnalist mitmekihilist grafeeni, milles valdavalt esineb kihtidevaheline rotatsiooniline korrapäratus. Kihtidevahelise rotatsioonilise korrapäratusega grafeeni süntees pakub suurt praktilist huvi, kuna selline mitmekihiline grafeen võiks evida ühekihilisele grafeenile sarnaseid laenguülekande omadusi.
- Mitmekihilise grafeeni kasvuga polükristallilisel nikkelalusel kaasneb märgatav aluspinna morfoloogia muutus – seda peab grafeeni sünteesi väljatöötamisel Ni-alustel kindlasti silmas pidama.

Edasi testiti Ni-alusel sünteesitud mitmekihilise grafeeni elektrokeemilisi omadusi ning uuriti selle pinna kasvujärgse funktsionaliseerimise võimalusi, kasutades erinevate diasooniumsoolade elektroredutseerimist. Neis uuringutes selgus:

- Nikkelkatalüsaatoril CVD-kasvatatud mitmekihilist grafeeni saab kasutada elektrokeemiliselt passiivse alusmaterjalina elektroodide elektrokatalüütiliselt aktiivsete materjalide uurimiseks. CVD-kasvatatud mitmekihilise grafeeni eeliseks on suhteliselt lihtne suurepinnaliste objektide valmistamise võimalus ning tunduvalt madalamad tootmiskulud, kui sama pindalaga kvaliteetsete HOPG-aluste valmistamisel.
- Nikkelalusel CVD-sünteesitud grafeeni pinda saab modifitseerida arüülrühmadega, kasutades arüüldiasooniumsoolade elektrokeemilist redutseerimist, ning sellise elektroodi valmistamiseks pole grafeeni vaja üle kanda uuele alusele.

Viimases osas uuriti transistorstruktuuri paisudielektrikkile kasvatamise võimalust funktsionaliseerimata grafeeni pinnale ALD meetodi abil, mille raames selgus järgnev:

- Kahetemperatuurne ALD protsess, mille puhul metalloksiidi kasvu initsieeritakse madalamal ja jätkatakse kõrgemal temperatuuril, võimaldab saada kõrgema kvaliteediga dielektrikkilet, kui seda võimaldab kumbki üheastmeline protsess. Siiski, nagu näitasid *in situ* kvartskristallmikrokaalumise (QCM) meetodil tehtud mõõtmised, siis isegi madalal temperatuuril (190 °C) esineb grafeeni pinnal oksiidkile nukleatsiooni viivitus, mis teeb keeruliseks pidevate õhukeste oksiidkihtide kasvatamise.
- Viimane on tingitud asjaolust, et grafeenile on iseloomulik mitte ainult nukleatsioonitsentrite vähesus, vaid ka nende tiheduse tugevalt ebaühtlane jaotus üle grafeeni pinna.
- Dielektrikkilede sadestamine grafeenile, kasutades metallkloriid-vesi ALD protsessi, põhjustab küll lateraalsete pingete tekkimist grafeenis, kuid ei genereeri struktuuridefekte selle heksagonaalses võres.

ACKNOWLEDGEMENTS

I would like to express my heartfelt gratitude to my supervisors Prof. Väino Sammelselg and Dr. Harry Alles, for their inspiring guidance, professional assistance and patience. I would like to express my appreciation to Dr. Ahti Niilisk, for sharing her valuable expertise, knowledge about Raman spectroscopy. I am also very thankful to Dr. Aile Tamm for her help and constant encouragement. I would like to thank all the co-authors for their contribution to the publications. Also, I am very thankful to all the colleagues from the Laboratory of Thin-Film Technology for their help and assistance.

I am grateful to my family for their continuous support throughout my studies.

This work has been supported by Graduate School of Doctorial Studies in Estonia: "Functional materials and technologies" (project 1.2.0401.09-0079), the Estonian Ministry of Education and Research (Target Financed Project No SF0180046s07 and Institutional Research Support Project IUT2-24), by Estonian Science Foundation (Grant ETF8666), the European Union through its European Regional Development Funds and though Estonian Ministry of Education and Research and SA Archimedes: Program of Centre of Excellence "High-technology Materials for Sustainable Development", TK117 (project no 3.2.0101.11-0030), and SA Archimedes (Project "Thin nanomaterial coating for functionalising and protection of metal surfaces" 12164T, no 3.2.1101.12-0026).

REFERENCES

[1] M. Choe, B.H. Lee, G. Jo, J. Park, W. Park, S. Lee, W.K. Hong, M.J. Seong, Y.H. Kahng, K. Lee, T. Lee, *Organic Electronics* 11 (2010) 1864–1869.

[2] S. Lee, G. Jo, S.J. Kang, G. Wang, M. Choe, W. Park, D.Y. Kim, Y.H. Kahng, T. Lee, *Adv. Mater.* 23 (2011) 100–105.

[3] B.-J. Kim, M.A. Mastro, J. Hite, C.R. Eddy, J. Kim, *Opt. Express* 18 (2010) 23030–23034.

[4] G. Jo, M. Choe, C.-Y. Cho, J.H. Kim, W. Park, S. Lee, W.-K. Hong, T.-W. Kim, S.-J. Park, B.H. Hong, Y.H. Kahng, T. Lee, *Nanotechnology* 21 (2010) 175201.

[5] G. Wang, Y. Kim, M. Choe, T.-W. Kim, T. Lee, *Adv. Mater.* 23 (2011) 755–760.

[6] Y.Y. Choi, S.J. Kang, H.K. Kim, W.M. Choi, S.I. Na, *Sol. Energy Mater. Sol. Cells* 96 (2012) 281–285.

[7] DianaBermana, V. Anirudha, A. Sumant, *Carbon* 59 (2013) 167–175.

[8] Z. Wenzheng, B. Srikant, K.K. Zhou, *Cabon* 119 (2017) 150–171.

[9] J. Ma, H. Xuan, H.L. Ho, W. Jin, Y. Yang, S. Fan, *IEEE Photonics Technol. Lett.* 25 (2013) 932–935.

[10] S.-E. Zhu, M. Krishna Ghatkesar, C. Zhang, G.C.A.M. Janssen, *Appl. Phys. Lett.* 102 (2013) 161904.

[11] M.S. Goh, M. Pumera, *Anal. Bioanal. Chem.* 399 (2011) 127–131.

[12] S. Jiang, X. Wang, S. Shi, J. Yuan, J. Fang, C. Gao, S. Liu, *14th ICEPT Proc.* (2013) 462–466.

[13] M.S. Goh, M. Pumera, *Chem. - An Asian J.* 5 (2010) 2355–2357.

[14] I. V Antonova, S. V Mutilin, V.A. Seleznev, R.A. Soots, V.A. Volodin, V. Ya Prinz, *Nanotechnology* 22 (2011) 285502.

[15] H. Choi, H.Y. Jeong, D.-S. Lee, C.-G. Choi, S.-Y. Choi, *Carbon Lett.* 14 (2013) 186–189.

[16] Y. Huang, X. Dong, Y. Liu, L.-J. Li, P. Chen, *J. Mater. Chem.* 21 (2011) 12358.

[17] B. Dlubak, M.B. Martin, R.S. Weatherup, H. Yang, C. Deranlot, R. Blume, R. Schloegl, A. Fert, A. Anane, S. Hofmann, P. Seneor, J. Robertson, *ACS Nano* 6 (2012) 10930–10934.

[18] M. Shiraishi, M. Ohishi, R. Nouchi, N. Mitoma, T. Nozaki, T. Shinjo, Y. Suzuki, *Adv. Funct. Mater.* 19 (2009) 3711–3716.

[19] H. Goto, A. Kanda, T. Sato, S. Tanaka, Y. Ootuka, S. Odaka, H. Miyazaki, K. Tsukagoshi, Y. Aoyagi, *Appl. Phys. Lett.* 92 (2008) 212110.

[20] D. Zhan, L. Sun, Z.H. Ni, L. Liu, X.F. Fan, Y. Wang, T. Yu, Y.M. Lam, W. Huang, Z.X. Shen, *Adv. Funct. Mater.* 20 (2010) 3504–3509.

[21] A. Luican, G. Li, A. Reina, J. Kong, R.R. Nair, K.S. Novoselov, A.K. Geim, E.Y. Andrei, *Phys. Rev. Lett.* 106 (2011) 126802.

[22] S. Latil, V. Meunier, L. Henrard, *Phys. Rev. B - Condens. Matter Mater. Phys.* 76 (2007) 201402.

[23] J. Hass, F. Varchon, J.E. Millán-Otoya, M. Sprinkle, N. Sharma, W.A. de Heer, C. Berger, P.N. First, L. Magaud, E.H. Conrad, *Phys. Rev. Lett.* 100 (2008) 125504.

[24] D. Chen, J. Li, D. Chen, *Chem. Soc. Rev.* 39 (2010) 3157–3180.

[25] M. Liu, R. Zhang, W. Chen, *Chem. Rev.* 114 (2014) 5117–5160.

[26] J. Hou, Y. Shao, M.W. Ellis, R.B. Moore, B. Yi, *Phys. Chem. Chem. Phys.* 13 (2011) 15384–15402.
[27] Q.H. Wang, C.J. Shih, G.L.C. Paulus, M.S. Strano, *J. Am. Chem. Soc.* 135 (2013) 18866–18875.
[28] W. Li, C. Tan, M.A. Lowe, H.D. Abruña, D.C. Ralph, *ACS Nano* 5 (2011) 2264–2270.
[29] A.T. Valota, I.A. Kinloch, K.S. Novoselov, C. Casiraghi, A. Eckmann, E.W. Hill, R.A. Dryfe, *ACS Nano* 5 (2011) 8809–15.
[30] X. Li, X. Yang, L. Jia, X. Ma, L. Zhu, *Electrochem. Commun.* 23 (2012) 94–97.
[31] A. Wong, M. Pumera, *Electrochem. Commun.* 22 (2012) 105–108.
[32] A. Ambrosi, S.Y. Chee, B. Khezri, R.D. Webster, Z. Sofer, M. Pumera, *Angew. Chemie - Int. Ed.* 51 (2012) 500–503.
[33] D.A. Brownson, C.E. Banks, *Phys. Chem. Chem. Phys.* 14 (2012) 8264–81.
[34] D.A.C. Brownson, C.E. Banks, *The Handbook of Graphene Electrochemistry*, Springer, London, 2014.
[35] R.L. Puurunen, *J. Appl. Phys.* 97 (2005) 121301.
[36] V. Georgakilas, M. Otyepka, A.B.A. Bourlinos, V. Chandra, N. Kim, K.C. Kemp, P. Hobza, R. Zboril, K.S. Kim, *Chem. Rev.* 112 (2012) 6156–6214.
[37] W.C. Shin, T.Y. Kim, O. Sul, B.J. Cho, *Appl. Phys. Lett.* 101 (2012) 1063.
[38] R.H.J. Vervuurt, B. Karasulu, M.A. Verheijen, W.M.M. Kessels, A.A. Bol, *Chem. Mater.* 29 (2017) 2090–2100.
[39] K.S. Novoselov, A.K. Geim, S.V. Morozov, D. Jiang, M.I. Katsnelson, I.V. Grigorieva, S.V. Dubonos, A.A. Firsov, *Nature* 438 (2005) 197–200.
[40] E.L. Wolf, *Graphene. A New Paradigm in Condensed Matter and Device Physics*, Oxford University Press, Oxford, 2014.
[41] I. Suarez-Martinez, N. Grobert, C.P. Ewels, *Carbon* 50 (2012) 741–747.
[42] A.K. Geim, K.S. Novoselov, *Nat. Mater.* 6 (2007) 183–191.
[43] Y. Wu, in:, Y. Wu, Z. Shen, T. Yu (Eds.), CRS Press, Boca Raton, 2014, p. 13.
[44] A.K. Geim, A.H. MacDonald, *Phys. Today* 60 (2007) 35–41.
[45] D.R. Cooper, B. D'Anjou, N. Ghattamaneni, B. Harack, M. Hilke, A. Horth, N. Majlis, M. Massicotte, L. Vandsburger, E. Whiteway, V. Yu, *ISRN Condens. Matter Phys.* 2012 (2012) 1–56.
[46] M.I. Katsnelson, *Mater. Today* 10 (2007) 20–27.
[47] S.V. Morozov, K.S. Novoselov, M.I. Katsnelson, F. Schedin, D.C. Elias, J.A. Jaszczak, A.K. Geim, *Phys. Rev. Lett.* 100 (2008) 016602.
[48] Z. Yuanbo, T. Yan-Wen, H.L. Stormer, P. Kim, *Nature* 438 (2005) 201–204.
[49] C. Soldano, A. Mahmood, E. Dujardin, *Carbon* 48 (2010) 2127–2150.
[50] R.R. Nair, P. Blake, A.N. Grigorenko, K.S. Novoselov, T.J. Booth, T. Stauber, N.M.R. Peres, A.K. Geim, *Science* 320 (2008) 1308.
[51] C. Lee, X. Wei, J.W. Kysar, J. Hone, *Science* 321 (2008) 385–388.
[52] N.D. Mermin, *Phys. Rev.* 176 (1968) 250–254.
[53] J. C. Meyer, A. K. Geim, M. I. Katsnelson, K.S. Novoselov, T. J. Booth, S. Roth, *Nature* 446 (2007) 60–63.
[54] A.O. Hare, F.V. Kusmartsev, K.I. Kugel, *Nano Lett.* 12 (2012) 1045–1052.
[55] A. Fasolino, J.H. Los, M.I. Katsnelson, *Nat. Mater.* 6 (2007) 858–861.
[56] K. Novoselov, A. Geim, S. Morozov, D. Jiang, Y. Zhang, S.V. Dubonos, I.V. Grigorieva, A.A. Firsov, *Science* 306 (2004) 666–669.
[57] P. Blake, E.W. Hill, A.H. Castro Neto, K.S. Novoselov, D. Jiang, R. Yang, T.J. Booth, A.K. Geim, *Appl. Phys. Lett.* 91 (2007) 13–15.

[58] F. Bonaccorso, Z. Sun, T. Hasan, A.C. Ferrari, *Nat. Photonics* 4 (2010) 611–622.
[59] K. Novoselov, Z. Jiang, Y. Zhang, S. Morozov, H.L. Stormer, U. Zeitler, J.C. Maan, G.S. Boebinger, P. Kim, A.K. Geim, *Solid State Commun.* 143 (2007) 14–19.
[60] A.H. Castro Neto, F. Guinea, N.M.R. Peres, K.S. Novoselov, A.K. Geim, *Rev. Mod. Phys.* 81 (2009) 109–162.
[61] Y. Huang, E. Sutter, N.N. Shi, J. Zheng, T. Yang, D. Englund, H.J. Gao, P. Sutter, *ACS Nano* 9 (2015) 10612–10620.
[62] M. Yi, Z. Shen, *J. Mater. Chem. A* 3 (2015) 11700–11715.
[63] Y. Hernandez, V. Nicolosi, M. Lotya, F. Blighe, Z. Sun, S. De, I.T. McGovern, B. Holland, M. Byrne, Y. Gunko, J. Boland, P. Niraj, G. Duesberg, S. Krishnamurti, R. Goodhue, J. Hutchison, V. Scardaci, A.C. Ferrari, J.N. Coleman, *Nat. Nanotechnol.* 3 (2008) 563–8.
[64] M.P. Lavin-Lopez, J.L. Valverde, L. Sanchez-Silva, A. Romero, *Ind. Eng. Chem. Res.* 55 (2016) 845–855.
[65] Y. Xu, H. Cao, Y. Xue, B. Li, W. Cai, *Nanomaterials* 8 (2018) 942.
[66] M. Lotya, P.J. King, U. Khan, S. De, J.N. Coleman, *ACS Nano* 4 (2010) 3155–3162.
[67] A.A. Green, M.C. Hersam, *Nano Lett.* 9 (2009) 4031–4036.
[68] X. Wang, P.F. Fulvio, G.A. Baker, G.M. Veith, R.R. Unocic, S.M. Mahurin, M. Chi, S. Dai, *Chem Commun* 46 (2010) 4487–4489.
[69] D. Nuvoli, L. Valentini, V. Alzari, S. Scognamillo, S.B. Bon, M. Piccinini, J. Illescas, A. Mariani, *J. Mater. Chem.* 21 (2011) 3428–3431.
[70] J. Fan, Z. Shi, Y. Ge, J. Wang, Y. Wang, J. Yin, *J. Mater. Chem.* 22 (2012) 13764–13772.
[71] A.B. Bourlinos, V. Georgakilas, R. Zboril, T.A. Steriotis, A.K. Stubos, C. Trapalis, *Solid State Commun.* 149 (2009) 2172–2176.
[72] S. Ahadian, M. Estili, V.J. Surya, J. Ramón-Azcón, X. Liang, H. Shiku, M. Ramalingam, T. Matsue, Y. Sakka, H. Bae, K. Nakajima, Y. Kawazoe, A. Khademhosseini, *Nanoscale* 7 (2015) 6436–6443.
[73] A. Pattammattel, C.V. Kumar, *Adv. Funct. Mater.* 25 (2015) 7088–7098.
[74] C.J. Shih, G.L.C. Paulus, Q.H. Wang, Z. Jin, D. Blankschtein, M.S. Strano, *Langmuir* 28 (2012) 8579–8586.
[75] M. Lotya, Y. Hernandez, P.J. King, R.J. Smith, V. Nicolosi, L.S. Karlsson, M. Blighe, S. De, Z. Wang, I.T. Mcgovern, G.S. Duesberg, J.N. Coleman, F.M. Blighe, *J. Am. Chem. Soc.* 131 (2009) 3611–3620.
[76] X. Wang, D. Tan, Z. Chu, L. Chen, X. Chen, J. Zhao, G. Chen, *RSC Adv.* 6 (2016) 112486–112492.
[77] Z. Sun, J. Vivekananthan, D.A. Guschin, X. Huang, V. Kuznetsov, P. Ebbinghaus, A. Sarfraz, M. Muhler, W. Schuhmann, *Chem. - A Eur. J.* 20 (2014) 5752–5761.
[78] Y. Ma, J. Han, M. Wang, X. Chen, S. Jia, *J. Mater.* 4 (2018) 108–120.
[79] Y. Su, I. Zhitomirsky, *Colloids Surfaces A Physicochem. Eng. Asp.* 436 (2013) 97–103.
[80] M. Yi, Z. Shen, X. Zhang, S. Ma, *J. Phys. D. Appl. Phys.* 46 (2013).
[81] J.S.Y. Chia, M.T.T. Tan, P.S. Khiew, J.K. Chin, H. Lee, D.C.S. Bien, C.W. Siong, *Chem. Eng. J.* 249 (2014) 270–278.
[82] M. Yi, Z. Shen, S. Ma, X. Zhang, *J. Nanoparticle Res.* 14 (2012) 1003.

[83] S. Wang, M. Yi, Z. Shen, X. Zhang, S. Ma, *RSC Adv.* 4 (2014) 25374–25378.
[84] C. Yeon, S.J. Yun, K.S. Lee, J.W. Lim, *Carbon* 83 (2015) 136–143.
[85] U. Khan, A. O'Neill, M. Lotya, S. De, J.N. Coleman, *Small* 6 (2010) 864–871.
[86] T. Lin, J. Chen, H. Bi, D. Wan, F. Huang, X. Xie, M. Jiang, *J. Mater. Chem. A* 1 (2012) 500–504.
[87] W. Zhao, F. Wu, H. Wu, G. Chen, *J. Nanomater.* 2010 (2010) 6.
[88] X. Chen, J.F. Dobson, C.L. Raston, *Chem. Commun.* 48 (2012) 3703.
[89] K.R. Paton, E. Varrla, C. Backes, R.J. Smith, U. Khan, A. O'Neill, C. Boland, M. Lotya, O.M. Istrate, P. King, T. Higgins, S. Barwich, P. May, P. Puczkarski, I. Ahmed, M. Moebius, H. Pettersson, E. Long, J. Coelho, S.E. O'Brien, E.K. McGuire, B.M. Sanchez, G.S. Duesberg, N. McEvoy, T.J. Pennycook, C. Downing, A. Crossley, V. Nicolosi, J.N. Coleman, *Nat. Mater.* 13 (2014) 624–630.
[90] M. Yi, Z. Shen, *Carbon* 78 (2014) 622–626.
[91] W. Ren, H.-M. Cheng, *Nat. Nanotech.* 9 (2014) 726–730.
[92] J. Zhu, *Nat. Nanotechnol.* 3 (2008) 528–529.
[93] W.S. Hummers, R.E. Offeman, *J. Am. Chem. Soc.* 80 (1958) 1339.
[94] J. Chen, B. Yao, C. Li, G. Shi, *Carbon* 64 (2013) 225–229.
[95] Y. Li, N. Chopra, *Jom* 67 (2015) 34–43.
[96] S. Pei, H.M. Cheng, *Carbon* 50 (2012) 3210–3228.
[97] I. Forbeaux, J. Themlin, J. Debever, 58 (1998) 396–406.
[98] Y. Li, N. Chopra, *Jom* 67 (2015) 44–52.
[99] W. Norimatsu, M. Kusunoki, *Chem. Phys. Lett.* 468 (2009) 52–56.
[100] S. Goler, C. Coletti, V. Piazza, P. Pingue, F. Colangelo, V. Pellegrini, K. V. Emtsev, S. Forti, U. Starke, F. Beltram, S. Heun, *Carbon* 51 (2013) 249–254.
[101] S. Sonde, F. Giannazzo, C. Vecchio, R. Yakimova, E. Rimini, V. Raineri, *Appl. Phys. Lett.* 97 (2010) 38–41.
[102] N. Ray, S. Shallcross, S. Hensel, O. Pankratov, *Phys. Rev. B - Condens. Matter Mater. Phys.* 86 (2012) 125426.
[103] W. Norimatsu, J. Takada, M. Kusunoki, *Phys. Rev. B - Condens. Matter Mater. Phys.* 84 (2011) 035424.
[104] K. V Emtsev, A. Bostwick, K. Horn, J. Jobst, G.L. Kellogg, L. Ley, J.L. McChesney, T. Ohta, S. a Reshanov, J. Röhrl, E. Rotenberg, A.K. Schmid, D. Waldmann, H.B. Weber, T. Seyller, *Nat. Mater.* 8 (2009) 203–207.
[105] T. Kobayashi, M. Bando, N. Kimura, K. Shimizu, K. Kadono, N. Umezu, K. Miyahara, S. Hayazaki, S. Nagai, Y. Mizuguchi, Y. Murakami, D. Hobara, *Appl. Phys. Lett.* 102 (2013) 1–5.
[106] P.W. Sutter, J.-I. Flege, E.A. Sutter, *Nat. Mater.* 7 (2008) 406–11.
[107] J. Coraux, A.T.N. Diaye, M. Engler, C. Busse, D. Wall, N. Buckanie, M. Heringdorf, R. Van Gastel, B. Poelsema, *New J. Phys.* 11 (2009) 023006.
[108] X. Wang, H. You, F. Liu, M. Li, L. Wan, S. Li, Q. Li, Y. Xu, R. Tian, Z. Yu, D. Xiang, J. Cheng, *Chem. Vap. Depos.* 15 (2009) 53–56.
[109] A. Reina, S. Thiele, X. Jia, S. Bhaviripudi, S. Mildred, M.S. Dresselhaus, J.A. Schaefer, J. Kong, S. Mildred, *Nano Res.* 2 (2009) 509–516.
[110] X. Li, W. Cai, J. An, S. Kim, J. Nah, D. Yang, R. Piner, A. Velamakanni, I. Jung, E. Tutuc, S.K. Banerjee, L. Colombo, R.S. Ruoff, *Science* 324 (2009) 1312–1314.
[111] E. Cazzanelli, T. Caruso, M. Castriota, A.R. Marino, A. Politano, G. Chiarello, M. Giarola, G. Mariotto, *J. Raman Spectrosc.* 44 (2013) 1393–1397.

[112] T. Oznuluer, E. Pince, E.O. Polat, O. Balci, O. Salihoglu, C. Kocabas, *Appl. Phys. Lett.* 98 (2011) 183101.
[113] X. An, F. Liu, Y.J. Jung, S. Kar, *J. Phys. Chem. C* 116 (2012) 16412–16420.
[114] Y. Xue, B. Wu, Y. Guo, L. Huang, L. Jiang, J. Chen, D. Geng, Y. Liu, W. Hu, G. Yu, *Nano Res.* 4 (2011) 1208–1214.
[115] E. Miniussi, M. Pozzo, T.O. Menteş, M.A. Niño, A. Locatelli, E. Vesselli, G. Comelli, S. Lizzit, D. Alfè, A. Baraldi, *Carbon* 73 (2014) 389–402.
[116] K. Gotterbarm, W. Zhao, O. Höfert, C. Gleichweit, C. Papp, H.-P. Steinrück, *Phys. Chem. Chem. Phys.* 15 (2013) 19625.
[117] G. Ruan, Z. Sun, Z. Peng, J.M. Tour, *ACS Nano* 5 (2011) 7601–7607.
[118] M. Choucair, P. Thordarson, J. a Stride, *Nat. Nanotechnol.* 4 (2009) 30–33.
[119] D.K. Singh, P.K. Iyer, P.K. Giri, *Int. J. Nanosci.* 10 (2011) 39–42.
[120] D. Deng, X. Pan, L. Yu, Y. Cui, Y. Jiang, J. Qi, W.X. Li, Q. Fu, X. Ma, Q. Xue, G. Sun, X. Bao, *Chem. Mater.* 23 (2011) 1188–1193.
[121] N.W. Pu, C.A. Wang, Y. Sung, Y.M. Liu, M. Der Ger, *Mater. Lett.* 63 (2009) 1987–1989.
[122] D. Rangappa, K. Sone, M. Wang, U.K. Gautam, D. Golberg, H. Itoh, M. Ichihara, I. Honma, *Chem. - A Eur. J.* 16 (2010) 6488–6494.
[123] C. Liu, G. Hu, H. Gao, *J. Supercrit. Fluids* 63 (2012) 99–104.
[124] L. Li, X. Zheng, J. Wang, Q. Sun, Q. Xu, *ACS Sustain. Chem. Eng.* 1 (2013) 144–151.
[125] M. Qian, Y.S. Zhou, Y. Gao, J.B. Park, T. Feng, M. Qian, Y.S. Zhou, Y. Gao, J.B. Park, T. Feng, S.M. Huang, 173108 (2013) 2011–2014.
[126] P. Russo, A. Hu, G. Compagnini, W.W. Duley, N.Y. Zhou, *Nanoscale* 6 (2014) 2381–2389.
[127] S.Z. Mortazavi, P. Parvin, A. Reyhani, *Laser Phys. Lett.* 547 (2012) 547–552.
[128] H.O. Jeschke, M.E. Garcia, K.H. Bennemann, *Phys. Rev. Lett.* 87 (2001) 015003.
[129] X. Jia, J. Campos-Delgado, M. Terrones, V. Meunier, M.S. Dresselhaus, *Nanoscale* 3 (2011) 86–95.
[130] H.O. Pierson, *Handbook of Chemical Vapor Deposition (CVD)*, Noyes Publications / William Andrew Publishing, LLC, New York, 1999.
[131] K.L. Choy, *Prog. Mater. Sci.* 48 (2003) 57–170.
[132] J.-H. Park, T.S. Sudarshan, eds., *Chemical Vapor Deposition (Vol. 2)*, ASM International, 2001.
[133] R.S. Weatherup, B. Dlubak, S. Hofmann, *ACS Nano* 6 (2012) 9996–10003.
[134] J. Wintterlin, M.L. Bocquet, *Surf. Sci.* 603 (2009) 1841–1852.
[135] M. Batzill, *Surf. Sci. Rep.* 67 (2012) 83–115.
[136] H.I. Rasool, E.B. Song, M.J. Allen, J.K. Wassei, R.B. Kaner, K.L. Wang, B.H. Weiller, J.K. Gimzewski, *Nano Lett.* 11 (2011) 251–256.
[137] M. Losurdo, M.M. Giangregorio, P. Capezzuto, G. Bruno, *Phys. Chem. Chem. Phys.* 13 (2011) 20836.
[138] J. Liu, P. Li, Y. Chen, Z. Wang, J. He, H. Tian, F. Qi, B. Zheng, J. Zhou, W. Lin, W. Zhang, *J. Alloys Compd.* 615 (2014) 415–418.
[139] T. Wu, G. Ding, H. Shen, H. Wang, L. Sun, D. Jiang, X. Xie, *Adv. Funct. Mater.* 23 (2013) 198–203.
[140] Z. Luo, Y. Lu, D.W. Singer, M.E. Berck, L.A. Somers, B.R. Goldsmith, A.T.C. Johnson, *Chem. Mater.* 23 (2011) 1441–1447.

[141] Z. Yan, J. Lin, Z. Peng, Z. Sun, Y. Zhu, L. Li, C. Xiang, E. Loı, C. Kittrell, J.M. Tour, *ACS Nano* 6 (2012) 9110–9117.
[142] W. Liu, H. Li, C. Xu, Y. Khatami, K. Banerjee, *Carbon* 49 (2011) 4122–4130.
[143] H. Wang, G. Wang, P. Bao, S. Yang, W. Zhu, X. Xie, W.J. Zhang, *J. Am. Chem. Soc.* 134 (2012) 3627–3630.
[144] R.S. Weatherup, B.C. Bayer, R. Blume, C. Baehtz, P.R. Kidambi, M. Fouquet, C.T. Wirth, R. Schlögl, S. Hofmann, *ChemPhysChem* 13 (2012) 2544–2549.
[145] L. Gan, Z. Luo, *ACS Nano* 7 (2013) 9480–9488.
[146] S. Bhaviripudi, X. Jia, M.S. Dresselhaus, J. Kong, *Nano Lett.* 10 (2010) 4128–4133.
[147] R.S. Edwards, K.S. Coleman, *Nanoscale* 5 (2013) 38–51.
[148] C.-M. Seah, S.-P. Chai, A.R. Mohamed, *Carbon* 70 (2014) 1–21.
[149] B. Hu, H. Ago, Y. Ito, K. Kawahara, M. Tsuji, E. Magome, K. Sumitani, N. Mizuta, K.I. Ikeda, S. Mizuno, *Carbon* 50 (2012) 57–65.
[150] B.S.J. Chae, F. Gu, K.K. Kim, E.S. Kim, H. Han, S.M. Kim, H. Shin, S. Yoon, J. Choi, M.H. Park, C.W. Yang, D. Pribat, Y.H. Lee, *Adv. Mater.* 21 (2009) 2328–2333.
[151] H. An, W. Lee, J. Jung, *Curr. Appl. Phys.* 11 (2011) S81–S85.
[152] X. Li, C.W. Magnuson, A. Venugopal, J. An, J.W. Suk, B. Han, M. Borysiak, W. Cai, A. Velamakanni, Y. Zhu, L. Fu, E.M. Vogel, E. Voelkl, L. Colombo, R.S. Ruoff, *Nano Lett.* 10 (2010) 4328–4334.
[153] H. Kim, C. Mattevi, M.R. Calvo, J.C. Oberg, L. Artiglia, S. Agnoli, C.F. Hirjibehedin, M. Chhowalla, E. Saiz, *ACS Nano* 6 (2012) 3614–3623.
[154] A. Cabrero-Vilatela, R.S. Weatherup, P. Braeuninger-Weimer, S. Caneva, S. Hofmann, *Nanoscale* 8 (2016) 2149–2158.
[155] D. Kondo, S. Sato, K. Yagi, N. Harada, M. Sato, M. Nihei, N. Yokoyama, *Appl. Phys. Express* 3 (2010) 025102.
[156] Lavin-Lopez, J.L. Valverde, L. Sanches-Silva, A. Romero, *J. Nanomater.* 2016 (2016) 1155.
[157] V. Skákalová, A.B. Kaiser, eds., *Graphene Properties, Preparation, Characterisation and Devices*, Woodhead Publishing, 2014.
[158] Y. Zhang, L. Gomez, F.N. Ishikawa, A. Madaria, K. Ryu, W. Chuan, B. Alexander, Z. Chongwu, *J. Phys. Chem. Lett.* 1 (2010) 3101–3107.
[159] I.I. Kondrashov, P.S. Rusakov, M.G. Rybin, A.S. Pozharov, E.D. Obraztsova, *J. Nanoelectron. Optoelectron.* 8 (2013) 79–82.
[160] I. Vlassiouk, M. Regmi, P. Fulvio, S. Dai, P. Datskos, G. Eres, S. Smirnov, *ACS Nano* 5 (2011) 6069–6076.
[161] S. Chaitoglou, E. Pascual, E. Bertran, J.L. Andujar, *J. Nanomater.* 2016 (2016) 1155.
[162] S. Choubak, M. Biron, P.L. Levesque, R. Martel, P. Desjardins, *J. Phys. Chem. Lett.* 4 (2013) 1100–1103.
[163] S. Choubak, P.L. Levesque, E. Gaufres, M. Biron, P. Desjardins, R. Martel, *J. Phys. Chem. C* 118 (2014) 21532–21540.
[164] N. Reckinger, A. Felten, C.N. Santos, B. Hackens, J.F. Colomer, *Carbon* 63 (2013) 84–91.
[165] K. Li, C. He, M. Jiao, Y. Wang, Z. Wu, *Carbon* 74 (2014) 255–265.
[166] X. Zhang, L. Wang, J. Xin, B.I. Yakobson, F. Ding, *J. Am. Chem. Soc.* 136 (2014) 3040–3047.
[167] J. Kang, D. Shin, S. Bae, B.H. Hong, *Nanoscale* 4 (2012) 5527–5537.

[168] X. Li, Y. Zhu, W. Cai, M. Borysiak, B. Han, D. Chen, R.D. Piner, L. Colombo, R.S. Ruoff, *Nano Lett.* 9 (2009) 4359–4363.
[169] K.S. Kim, Y. Zhao, H. Jang, S.Y. Lee, J.M. Kim, K.S. Kim, J.-H. Ahn, P. Kim, J.-Y. Choi, B.H. Hong, *Nature* 457 (2009) 706–10.
[170] S. Bae, H. Kim, Y. Lee, X. Xu, J.-S. Park, Y. Zheng, J. Balakrishnan, T. Lei, H. Ri Kim, Y. Il Song, Y.-J. Kim, K.S. Kim, B. Özyilmaz, J.-H. Ahn, B.H. Hong, S. Iijima, *Nat. Nanotechnol.* 5 (2010) 574–578.
[171] J. Chan, A. Venugopal, A. Pirkle, S. McDonnell, D. Hinojos, C.W. Magnuson, R.S. Ruoff, L. Colombo, R.M. Wallace, E.M. Vogel, *ACS Nano* 6 (2012) 3224–3229.
[172] C. Kim, J.Y. Woo, J. Choi, J. Park, C.S. Han, *Scr. Mater.* 66 (2012) 535–537.
[173] A. Ambrosi, M. Pumera, *Nanoscale* 6 (2014) 472–476.
[174] J. Kang, S. Hwang, J.H. Kim, M.H. Kim, J. Ryu, S.J. Seo, B.H. Hong, M.K. Kim, J.-B. Choi, *ACS Nano* (2012) 5360–5365.
[175] P.J. Goodhew, F.J. Humphreys, R. Beanland, *Electron Microscopy And Analysis*, 3rd ed., Taylor & Francis, London and New York, 2001.
[176] R. Egerton, *Physical Principles of Electron Microscopy: An Introduction to TEM, SEM and AEM*, Springer, Boston, MA, 2005.
[177] J.I. Goldstein, D.E. Newbury, P. Echlin, D.C. Joy, C.E. Lyman, E. Lifshin, L. Sawyer, J.R. Michael, *Scanning Electron Microscopy and X-Ray Microanalysis*, 3rd ed., Springer, New York, 2003.
[178] L. Reimer, *Scanning Electron Microscopy Physics of Image Formation and Microanalysis*, 2nd editio, Springer, 1998.
[179] T. Maitland, S. Sitzman, in:, W. Zhou, Z.L. Wang (Eds.), Scanning Microsc. Nanotechnol. Tech. Appl., Springer, New York, 2006, p. 536.
[180] F.J. Humphreys, *J. Mater. Sci.* 36 (2001) 3833–3854.
[181] V. Kochat, A.N. Pal, S. E.S., A. B.S., A. Gairola, S.A. Shivashankar, S. Raghavan, A. Ghosh, *J. Appl. Phys.* 110 (2012) 014315.
[182] H. Hiura, H. Miyazaki, K. Tsukagoshi, *Appl. Phys. Express* 3 (2010) 095101.
[183] H. Wang, C. Yamada, Y. Homma, *Jpn. J. Appl. Phys.* 54 (2015) 050301–4.
[184] K. Takahashi, K. Yamada, H. Kato, H. Hibino, Y. Homma, *Surf. Sci.* 606 (2012) 728–732.
[185] J. Xie, J. Spallas, *Imaging Graphene via Low Voltage Field Emission Scanning Electron Microscopy*, 2012.
[186] R.M. Jacobberger, M.S. Arnold, *Chem. Mater.* 25 (2013) 871–877.
[187] E. Meca, J. Lowengrub, H. Kim, C. Mattevi, V.B. Shenoy, *Nano Lett.* 13 (2013) 5692–5697.
[188] P. Zhao, A. Kumamoto, S. Kim, X. Chen, B. Hou, S. Chiashi, E. Einarsson, Y. Ikuhara, S. Maruyama, *J. Phys. Chem. C* 117 (2013) 10755–10763.
[189] F. Yang, Y. Liu, W. Wu, W. Chen, L. Gao, J. Sun, *Nanotechnology* 23 (2012) 475705.
[190] J. Lee, X. Zheng, R.C. Roberts, P.X.L. Feng, *Diam. Relat. Mater.* 54 (2015) 64–73.
[191] D. Brandon, D.W. Kaplan, *Microstructural Characterization of Materials*, 2nd ed., John Wiley & Sons Ltd, 2008.
[192] G. Leggett, in:, J. Vickerman, I. Gilmore (Eds.), Surf. Anal. – Princ. Tech., 2nd ed., John Wiley & Sons Ltd, 2009.
[193] U.D. Schwarz, in:, S. Amelinckx, D. Dyck, J. Landuyt, G. Tendeloo (Eds.), Handb. Microsc. Methods II, VCH Verlagsgesellschaft mbH, Weinheim, 1997.

[194] K.S. Novoselov, D. Jiang, F. Schedin, T.J. Booth, V.V. Khotkevich, S.V. Morozov, A.K. Geim, *PNAS* 102 (2005) 10451–10453.
[195] M. Ishigami, J. Chen, W. Cullen, M. Fuhrer, E.D. Williams, *Nano Lett.* 7 (2007) 1643–1648.
[196] E. Obraztsova, A. Osadchy, E.D. Obraztsova, S. Lefrant, I. V. Yaminsky, *Phys. Status Solidi* 245 (2008) 2055–2059.
[197] P. Nemes-Incze, Z. Osváth, K. Kamarás, L.P. Biró, *Carbon* 46 (2008) 1435–1442.
[198] Z. Sun, S. Hämäläinen, J. Sainio, J. Lahtinen, D. Vanmeakelbergh, P. Liljeroth, *Phys. Rev. B* 83 (2011) 081415.
[199] T. Filleter, R. Bennewitz, *Phys. Rev. B* 81 (2010) 1–7.
[200] A. Pirkle, J. Chan, A. Venugopal, D. Hinojos, C. Magnuson, S. McDonnell, L. Colombo, E.M. Vogel, R.S. Ruoff, R. Wallace, *Appl. Phys. Lett.* 99 (2011) 122108.
[201] J. Suk, W. Lee, J. Lee, H. Chou, R. Piner, Y. Hao, D. Akinwande, R.S. Ruoff, *Nano Lett.* 13 (2013) 1462–1467.
[202] H.S. Song, S.L. Li, H. Miyazaki, S. Sato, K. Hayashi, A. Yamada, N. Yokoyama, K. Tsukagoshi, *Sci. Rep.* 2 (2012) 0337.
[203] P. Nemes-Incze, K.J. Yoo, L. Tapasztó, G. Dobrik, J. Lábár, Z.E. Horváth, C. Hwang, L.P. Biró, *Appl. Phys. Lett.* 99 (2011) 023104.
[204] A. Sikora, M. Woszczyna, M. Friedemann, F.J. Ahlers, M. Kalbac, *Micron* 43 (2012) 479–486.
[205] Y. Xuan, Y. Wu, T. Shen, M. Qi, M.A. Capano, *Appl. Phys. Lett.* 92 (2008) 013101–3.
[206] J.M.P. Alaboson, Q.H. Wang, J.D. Emery, A.L. Lipson, M.J. Bedzyk, J.W. Elam, M.J. Pellin, M.C. Hersam, *ACS Nano* 5 (2011) 5223–5232.
[207] F. Speck, M. Ostler, J. Ŕohrl, K. V. Emtsev, M. Hundhausen, L. Ley, T. Seyller, *Phys. Status Solidi* 7 (2010) 398–401.
[208] L. Reimer, H. Kohl, *Transmission Electron Microscopy: Physics of Image Formation*, 5th ed., Springer, New York, 2008.
[209] D.B. Williams, C.B. Carter, *Transmission Electron Microscopy: A Textbook for Materials Science*, Springer, New York, 2009.
[210] M. Watanabe, M. Kanno, E. Okunishi, *JEOL News* 45 (2010) 8–15.
[211] A.C. Ferrari, J.C. Meyer, V. Scardaci, C. Casiraghi, M. Lazzeri, F. Mauri, S. Piscanec, D. Jiang, K.S. Novoselov, S. Roth, A.K. Geim, *Phys. Rev.* 97 (2006) 187401.
[212] G.-P. Dai, J.-M. Zhang, S. Deng, *Chem. Phys. Lett.* 516 (2011) 212–215.
[213] J. Lee, E.K. Lee, W. Joo, Y. Jang, B. Kim, J.Y. Lim, S. Choi, S.J. Ahn, J.R. Ahn, M. Park, C. Yang, B.L. Choi, S. Hwang, D. Whang, *Science* 334 (2014) 286–290.
[214] Z. Liu, K. Suenaga, P.J.F. Harris, S. Iijima, *Phys. Rev. Lett.* 102 (2009) 015501.
[215] M.H. Gass, U. Bangert, A.L. Bleloch, P. Wang, R.R. Nair, A.K. Geim, *Nat. Nanotechnol.* 3 (2008) 676–681.
[216] L.S. Panchakarla, K.S. Subrahmanyam, S.K. Saha, A. Govindaraj, H.R. Krishnamurthy, U. V. Waghmare, C.N.R. Rao, *Adv. Mater.* 21 (2009) 4726–30.
[217] W. Zhou, M.D. Kapetanakis, M.P. Prange, S.T. Pantelides, S.J. Pennycook, J.C. Idrobo, *Phys. Rev. Lett.* 109 (2012) 206803.

[218] P.Y. Huang, C.S. Ruiz-Vargas, A.M. van der Zande, W.S. Whitney, M.P. Levendorf, J.W. Kevek, S. Garg, J.S. Alden, C.J. Hustedt, Y. Zhu, J. Park, P.L. McEuen, D.A. Muller, *Nature* 469 (2011) 389–92.
[219] K. Suenaga, M. Koshino, *Nature* 468 (2010) 1088–1090.
[220] U. Bangert, W. Pierce, D.M. Kepaptsoglou, Q. Ramasse, R. Zan, M.H. Gass, J.A. Van den Berg, C.B. Boothroyd, J. Amani, H. Hofsäss, *Nano Lett.* 13 (2013) 4902–4907.
[221] T.J. Booth, P. Blake, R.R. Nair, D. Jiang, E.W. Hill, U. Bangert, A. Bleloch, M. Gass, K.S. Novoselov, M.I. Katsnelson, A.K. Geim, *Nano Lett.* 8 (2008) 2442–2446.
[222] J.C. Meyer, A.K. Geim, M.I. Katsnelson, K.S. Novoselov, D. Obergfell, S. Roth, C. Girit, A. Zettl, *Solid State Commun.* 143 (2007) 101–109.
[223] K. Kim, Z. Lee, W. Regan, C. Kisielowski, M.F. Crommie, A. Zettl, *ACS Nano* 5 (2011) 2142–2146.
[224] H. He, C. Nelson, *Ultramicroscopy* 107 (2007) 340–344.
[225] F. Banhart, J. Kotakoski, A. V. Krasheninnikov, *ACS Nano* 5 (2011) 26–41.
[226] J. Kotakoski, A. V. Krasheninnikov, U. Kaiser, J.C. Meyer, *Phys. Rev. Lett.* 106 (2011) 105505.
[227] J.C. Meyer, F. Eder, S. Kurasch, V. Skakalova, J. Kotakoski, H.J. Park, A. Chuvilin, S. Eyhusen, G. Benner, A. V. Krasheninnikov, U. Kaiser, *Phys. Rev. Lett.* 108 (2012) 196102.
[228] J.C. Meyer, C. Kisielowski, R. Erni, M.D. Rossell, M.F. Crommie, A. Zettl, *Nano Lett.* 8 (2008) 3582–3586.
[229] A.C. Ferrari, D.M. Basko, *Nat. Nanotechnol.* 8 (2013) 235–246.
[230] J.R. Ferraro, K. Nakamoto, C.W. Brown, *Introductory Raman Spectroscopy*, 2nd ed., Elsevier, 2003.
[231] https://www.renishaw.com/en/raman-spectroscopy-in-more-detail--25806, (n.d.).
[232] E. Smith, G. Dent, *Modern Raman Sectroscopy - A Practical Approach*, John Wiley & Sons, Ltd., Chichester, 2005.
[233] M.S. Dresselhaus, A. Jorio, M. Hofmann, G. Dresselhaus, R. Saito, *Nano Lett.* 10 (2010) 751–758.
[234] R. Nemanich, J. Glass, G. Lucovsky, R. Shroder, *J. Vac. Sci. Technol. A* 6 (1988) 1783–7.
[235] M.A. Pimenta, G. Dresselhaus, M.S. Dresselhaus, L.G. Cançado, A. Jorio, R. Saito, *Phys. Chem. Chem. Phys.* 9 (2007) 1276–1291.
[236] T.M.G. Mohiuddin, A. Lombardo, R.R. Nair, A. Bonetti, G. Savini, R. Jalil, N. Bonini, D.M. Basko, C. Galiotis, N. Marzari, K.S. Novoselov, A.K. Geim, A.C. Ferrari, *Phys. Rev. B* 79 (2009) 205433.
[237] C. Casiraghi, S. Pisana, K.S. Novoselov, A.K. Geim, A.C. Ferrari, *Appl. Phys. Lett.* 91 (2007) 1–3.
[238] C. Cong, T. Yu, R. Saito, G.F. Dresselhaus, M.S. Dresselhaus, *ACS Nano* 5 (2011) 1600–1605.
[239] C.H. Lui, T.F. Heinz, *Phys. Rev. B* 87 (2013) 121404.
[240] C. Cong, T. Yu, K. Sato, J. Shang, R. Saito, G.F. Dresselhaus, M.S. Dresselhaus, *ACS Nano* 5 (2011) 8760–8768.
[241] J. Campos-Delgado, L.G. Cançado, C.A. Achete, A. Jorio, J.P. Raskin, *Nano Res.* 6 (2013) 269–274.

[242] L.M. Malard, M.A. Pimenta, G. Dresselhaus, M.S. Dresselhaus, *Phys. Rep.* 473 (2009) 51–87.
[243] A.C. Ferrari, *Solid State Commun.* 143 (2007) 47–57.
[244] D. Graf, F. Molitor, K. Ensslin, C. Stampfer, A. Jungen, C. Hierold, L. Wirtz, *Nano Lett.* 7 (2006) 238–242.
[245] A. Das, S. Pisana, B. Chakraborty, S. Piscanec, S. Saha, U. Waghmare, K. Novoselov, H. Krishnamurthy, A. Geim, A. Ferrari, A. Sood, *Nat. Nanotechnol.* 3 (2008) 210–5.
[246] Z.H. Ni, T. Yu, H.Y. Lu, Y.Y. Wang, Y.P. Feng, Z.X. Shen, *ACS Nano* 2 (2008) 2301–5.
[247] J.E. Proctor, E. Gregoryanz, K.S. Novoselov, M. Lotya, J.N. Coleman, M.P. Halsall, *Phys. Rev. B* 80 (2009) 073408.
[248] M. Mohr, J. Maultzsch, C. Thomsen, *Phys. Rev. B* 82 (2010) 201409.
[249] M. Huang, H. Yan, C. Chen, D. Song, T.F. Heinz, J. Hone, *PNAS* 106 (2009) 7304–7308.
[250] M. Huang, H. Yan, T.F. Heinz, J. Hone, *Nano Lett.* 10 (2010) 4074–4079.
[251] C. Casiraghi, A. Hartschuh, H. Qian, S. Pliscanec, C. Georgia, A. Fasoli, K.S. Novoselov, D.M. Basko, A.C. Ferrari, *Nano Lett.* 9 (2009) 1433–1441.
[252] B. Krauss, P. Nemes-Incze, V. Skakalova, L.P. Biró, K. von Klitzing, J.H. Smet, *Nano Lett.* 10 (2010) 4544–4548.
[253] E.H.M. Ferreira, M.V.O. Moutinho, F.F. Stavale, M.M. Lucchese, R.B. Capaz, C.A. Achete, A. Jorio, *Phys. Rev. B* 82 (2010) 125429.
[254] P. Tan, W. Han, W. Zhao, Z. Wu, K. Chang, H. Wang, Y. Wang, N. Bonini, N. Marzari, G. Savini, A. Lombardo, A. Ferrari, *Nat. Mater.* 11 (2012) 294–300.
[255] C.H. Lui, L.M. Malard, S. Kim, G. Lantz, F.E. Laverge, R. Saito, T.F. Heinz, *Nano Lett.* 12 (2012) 5539–5544.
[256] K. Kim, S. Coh, L.Z. Tan, W. Regan, J.M. Yuk, E. Chatterjee, M.F. Crommie, M.L. Cohen, S.G. Louie, A. Zettl, *Phys. Rev. Lett.* 108 (2012) 246103.
[257] R. He, T.F. Chung, C. Delaney, C. Keiser, L.A. Jauregui, P.M. Shand, C.C. Chancey, Y. Wang, J. Bao, Y.P. Chen, *Nano Lett.* 13 (2013) 3594–3601.
[258] V. Carozo, C.M. Almeida, E.H.M. Ferreira, L.G. Cançado, C.A. Achete, A. Jorio, *Nano Lett.* 11 (2011) 4527–4534.
[259] J. Campos-Delgado, G. Algara-Siller, C.N. Santos, U. Kaiser, J.P. Raskin, *Small* 9 (2013) 3247–3251.
[260] C.C. Lu, Y.C. Lin, Z. Liu, C.H. Yeh, K. Suenaga, P.W. Chiu, *ACS Nano* 7 (2013) 2587–2594.
[261] M. Ritala, M. Leskelä, *Nanotechnology* 10 (1999) 19–24.
[262] P.M. Martin, ed., *Handbook of Deposition Technologies for Films and Coatings: Science, Applications and Technology*, 5th ed., Elsevier Inc., US, 2010.
[263] X. Wang, S. Tabakman, H. Dai, *J. Am. Chem. Soc.* 130 (2008) 8152–3.
[264] J.L. Bahr, J.M. Tour, *J. Mater. Chem.* 12 (2002) 1952–1958.
[265] D.B. Farmer, R.G. Gordon, *Electrochem. Solid-State Lett.* 8 (2005) 89–91.
[266] J.L. Bahr, J.M. Tour, *Chem. Mater.* 13 (2001) 3823–4.
[267] Y. Lu, S. Bangsaruntip, X. Wang, L. Zhang, Y. Nishi, H. Dai, *J. Am. Chem. Soc.* 128 (2006) 3518–19.
[268] G.-D. Zhan, X. Du, D.M. King, L.F. Hakim, X. Liang, J.A. McCormick, A.W. Weimer, *J. Am. Ceram. Soc.* 91 (2008) 831–835.
[269] D.B. Farmer, R.G. Gordon, *Nano Lett.* 6 (2006) 699–703.

[270] J.R. Williams, L. DiCarlo, C.M. Marcus, *Science* 317 (2007) 638–41.
[271] B. Lee, S.-Y. Park, H.-C. Kim, K.J. Cho, E.M. Vogel, M.J. Kim, R.M. Wallace, J. Kim, *Appl. Phys. Lett.* 92 (2008) 203102.
[272] L. Cai, J.L. Bahr, Y. Yao, J.M. Tour, *Chem. Mater.* 14 (2002) 4235–4241.
[273] J.M. Simmons, B.M. Nichols, S.E. Baker, M.S. Marcus, O.M. Castellini, C.-S. Lee, R.J. Hamers, M.A. Eriksson, *J. Phys. Chem. B* 110 (2006) 7113–8.
[274] M. Rooth, R.A. Quinlan, E. Widenkvist, J. Lu, H. Grennberg, B.C. Holloway, A. Hårsta, U. Jansson, *J. Cryst. Growth* 311 (2009) 373–377.
[275] V.A. Coleman, R. Knut, O. Karis, H. Grennberg, U. Jansson, R. Quinlan, B.C. Holloway, B. Sanyal, O. Eriksson, *J. Phys. D* 41 (2008) 062001.
[276] S. Kim, J. Nah, I. Jo, D. Shahrjerdi, L. Colombo, Z. Yao, E. Tutuc, S.K. Banerjee, *Appl. Phys. Lett.* 94 (2009) 062107.
[277] S. Vivekchand, C. Rout, K. Subrahmanyam, A. Govindaraj, C. Rao, *J. Chem. Sci.* 120 (2008) 9–13.
[278] M.D. Stoller, S. Park, Y. Zhu, J. An, R.S. Ruoff, *Nano Lett.* 8 (2008) 3498–3502.
[279] E.J. Yoo, J. Kim, E. Hosono, H. Zhou, T. Kudo, I. Honma, *Nano Lett.* 8 (2008) 2277–2282.
[280] C. Wang, D. Li, C.O. Too, G.G. Wallace, *Chem. Mater.* 21 (2009) 2604–2606.
[281] Y. Dong, Z.S. Wu, W. Ren, H.M. Cheng, X. Bao, *Sci. Bull.* 62 (2017) 724–740.
[282] R. Raccichini, A. Varzi, S. Passerini, B. Scrosati, *Nat. Mater.* 14 (2015) 271–279.
[283] J. Xia, F. Chen, J. Li, N. Tao, *Nat. Nanotechnol.* 4 (2009) 505–509.
[284] X. Cao, Y. Shi, W. Shi, G. Lu, X. Huang, Q. Yan, Q. Zhang, H. Zhang, *Small* 7 (2011) 3163–3168.
[285] Y. Zhu, S. Murali, M.D. Stoller, K. Ganesh, W. Cai, P.J. Ferreira, A. Pirkle, R.M. Wallace, K.A. Cychosz, M. Thommes, D. Su, E.A. Stach, R.S. Ruoff, *Science* 332 (2011) 1537–1541.
[286] N. Jung, S. Kwon, D. Lee, D.M. Yoon, Y.M. Park, A. Benayad, J.Y. Choi, J.S. Park, *Adv. Mater.* 25 (2013) 6854–6858.
[287] Z.D. Huang, B. Zhang, S.W. Oh, Q. Bin Zheng, X.Y. Lin, N. Yousefi, J.K. Kim, *J. Mater. Chem.* 22 (2012) 3591–3599.
[288] A. Yu, A. Sy, A. Davies, *Synth. Met.* 161 (2011) 2049–2054.
[289] Q. Ke, C. Tang, Y. Liu, H. Liu, J. Wang, *Mater. Res. Express* 1 (2014) 025015.
[290] X. Huang, Z. Zeng, Z. Fan, J. Liu, H. Zhang, *Adv. Mater.* 24 (2012) 5979–6004.
[291] D. Pan, S. Wang, B. Zhao, M. Wu, H. Zhang, Y. Wang, Z. Jiao, *Chem. Mater.* 21 (2009) 3136–3142.
[292] M. Liang, L. Zhi, *J. Mater. Chem.* 19 (2009) 5871–5878.
[293] P. Guo, H. Song, X. Chen, *Electrochem. Commun.* 11 (2009) 1320–1324.
[294] L.Z. Bai, D.L. Zhao, T.M. Zhang, W.G. Xie, J.M. Zhang, Z.M. Shen, *Electrochim. Acta* 107 (2013) 555–561.
[295] S.-M. Paek, E. Yoo, I. Honma, *Nano Lett.* 9 (2009) 72–75.
[296] S. Yang, X. Feng, S. Ivanovici, K. Müllen, *Angew. Chemie - Int. Ed.* 49 (2010) 8408–8411.
[297] J. Zhu, K. Sun, D. Sim, C. Xu, H. Zhang, H.H. Hng, Q. Yan, *Chem. Commun.* 47 (2011) 10383–10385.
[298] G. Kucinskis, G. Bajars, J. Kleperis, *J. Power Sources* 240 (2013) 66–79.
[299] R. Tang, Q. Yun, W. Lv, Y.B. He, C. You, F. Su, L. Ke, B. Li, F. Kang, Q.H. Yang, *Carbon* 103 (2016) 356–362.

[300] J. Luo, J. Liu, Z. Zeng, C.F. Ng, L. Ma, H. Zhang, J. Lin, Z. Shen, H.J. Fan, *Nano Lett.* 13 (2013) 6136–6143.
[301] I.H. Son, J.H. Park, S. Park, K. Park, S. Han, J. Shin, S.G. Doo, Y. Hwang, H. Chang, J.W. Choi, *Nat. Commun.* 8 (2017) 1561.
[302] N. Li, Z. Chen, W. Ren, F. Li, H.-M. Cheng, *Proc. Natl. Acad. Sci.* 109 (2012) 17360–17365.
[303] D.A.C. Brownson, D.K. Kampouris, C.E. Banks, *J. Power Sources* 196 (2011) 4873–4885.
[304] S. Sharma, B.G. Pollet, *J. Power Sources* 208 (2012) 96–119.
[305] M. Yaldagard, M. Jahanshahi, N. Seghatoleslami, *World J. Nano Sci. Eng.* 3 (2013) 121–153.
[306] D.A. Stevens, M.T. Hicks, G.M. Haugen, J.R. Dahn, *J. Electrochem. Soc.* 152 (2005) 2309–15.
[307] R. Kou, Y. Shao, D. Wang, M.H. Engelhard, J.H. Kwak, J. Wang, V. V. Viswanathan, C. Wang, Y. Lin, Y. Wang, I.A. Aksay, J. Liu, *Electrochem. Commun.* 11 (2009) 954–957.
[308] H.-W. Ha, I.Y. Kim, S.-J. Hwang, R.S. Ruoff, *Electrochem. Solid-State Lett.* 14 (2011) B70-73.
[309] Y. Xin, J. Liu, Y. Zhou, W. Liu, J. Gao, Y. Xie, *J. Power Sources* 196 (2011) 1012–1018.
[310] L. Dong, R. Reddy, S. Gari, Z. Li, M.M. Craig, S. Hou, *Carbon* 48 (2009) 781–787.
[311] E. Yoo, T. Okata, T. Akita, M. Kohyama, J. Nakamura, I. Homna, *Nano Lett.* 9 (2009) 2255–2259.
[312] Y. Lu, Y. Jiang, H. Wu, W. Chen, *J. Phys. Chem. C* 117 (2013) 2926–2938.
[313] L. Qu, Y. Liu, J.-B. Baek, L. Dai, *ACS Nano* 4 (2010) 1321–1326.
[314] Y. Shao, S. Zhang, M.H. Engelhard, G. Li, G. Shao, Y. Wang, J. Liu, I.A. Aksay, Y. Lin, *J. Mater. Chem.* 20 (2010) 7491–6.
[315] M.S. Ahmed, S. Jeon, *J. Power Sources* 218 (2012) 168–173.
[316] S. Wang, D. Yu, L. Dai, D.W. Chang, J.-B. Baek, *ACS Nano* 5 (2011) 6202–6209.
[317] Y. Shao, J. Wang, H. Wu, J. Liu, I.A. Aksay, Y. Lin, *Electroanalysis* 22 (2010) 1027–1036.
[318] J. Aarik, A. Aidla, A.-A. Kiisler, T. Uustare, V. Sammelselg, *Thin Solid Films* 340 (1999) 110–116.
[319] J. Aarik, A. Aidla, H. Mändar, T. Uustare, V. Sammelselg, *Thin Solid Films* 408 (2002) 97–103.
[320] C.A. Putman, K.O. van der Werf, B.G. de Grooth, N.F. van Hulst, J. Greve, P.K. Hansma, in:, S. Manne (Ed.), International Society for Optics and Photonics, 1992, pp. 198–204.
[321] M. Delamar, R. Hitmi, J. Pinson, J. Savéant, *J. Am. Chem. Soc.* 114 (1992) 5883–5884.
[322] D. Cheng, M. Hou, M. Moors, T.V. de Bocarmé, N. Kruse, *Chem. Phys. Lett.* 492 (2010) 63–67.
[323] F. Sette, T. Hashizume, F. Comin, A.A. MacDowell, P.H. Citrin, *Phys. Rev. Lett.* 61 (1988) 1384–1387.
[324] R. Rao, R. Podila, R. Tsuchikawa, J. Katoch, D. Tishler, A.M. Rao, M. Ishigami, *ACS Nano* 5 (2011) 1594–1599.

[325] P.T. Araujo, D.L. Mafra, K. Sato, R. Saito, J. Kong, M.S. Dresselhaus, *Sci. Rep.* 2 (2012) 1017.
[326] A. Niilisk, T. Kahro, V. Kiisk, M. Rähn, H. Alles, J. Aarik, V. Sammelselg, *Open Phys.* 13 (2015) 34–40.
[327] Y. Wang, Z. Su, W. Wu, S. Nie, X. Lu, H. Wang, K. McCarty, S. Pei, F. Robles-Hernandez, V.G. Hadjiev, J. Bao, *Nanotechnology* 25 (2014) 335201.
[328] A. Tiberj, N. Camara, P. Godignon, J. Camassel, *Nanoscale Res. Lett.* 6 (2011) 478.
[329] V. Carozo, C.M. Almeida, B. Fragneaud, P.M. Bedê, M.V.O. Moutinho, J. Ribeiro-Soares, N.F. Andrade, A.G. Souza Filho, M.J.S. Matos, B. Wang, M. Terrones, R.B. Capaz, A. Jorio, C.A. Achete, L.G. Cançado, *Phys. Rev. B* 88 (2013) 085401.
[330] J. Wu, H. Xu, W. Mu, L. Xie, X. Ling, J. Kong, M.S. Dresselhaus, J. Zhang, *J. Phys. Chem. C* 118 (2014) 3636–3643.
[331] C. Cong, T. Yu, *Nat. Commun.* 5 (2014) 4709.
[332] K. Sato, J.S. Park, R. Saito, C. Cong, T. Yu, C.H. Lui, T.F. Heinz, G. Dresselhaus, M.S. Dresselhaus, *Phys. Rev. B* 84 (2011) 035419.
[333] Y.R. Hernandez, S. Schweitzer, J.-S. Kim, A.K. Patra, J. Englert, I. Lieberwirth, A. Liscio, V. Palermo, X. Feng, A. Hirsch, M. Kläui, K. Müllen, *ACS Nano* 13 (2013) 6087.
[334] A. Allard, L. Wirtz, *Nano Lett.* 10 (2010) 4335–4340.
[335] C. Cong, K. Li, X.X. Zhang, T. Yu, *Sci. Rep.* 3 (2013) 1195.
[336] K. Kumar, Y.S. Kim, E.H. Yang, *Carbon* 65 (2013) 35–45.
[337] H. Wang, Y. Wang, X. Cao, M. Feng, G. Lan, *J. Raman Spectrosc.* 40 (2009) 1791–1796.
[338] A. Gupta, G. Chen, P. Joshi, S. Tadigadapa, P.C. Eklund, U. V Park, V. Pennsyl, (2006) 1–7.
[339] Y. Duhee, M. Hyerim, C. Hyeonsik, C. JinSik, C. JungAe, P. BaeHo, *J. Korean Phys. Soc.* 55 (2009) 1299.
[340] D. Tomnek, S.G. Louie, *Phys. Rev. B* 37 (1988) 8327–8336.
[341] Y. Murata, V. Petrova, B.B. Kappes, A. Ebnonnasir, I. Petrov, Y. Xie, C. V Ciobanu, S. Kodambaka, *ASC Nano* 4 (2010) 6509–6514.
[342] Z. Zou, V. Carnevali, M. Jugovac, L.L. Patera, A. Sala, M. Panighel, C. Cepek, G. Soldano, M.M. Mariscal, M. Peressi, G. Comelli, C. Africh, *Carbon* 130 (2018) 441–447.
[343] N.A. Vinogradov, A.A. Zakharov, V. Kocevski, J. Rusz, K.A. Simonov, O. Eriksson, A. Mikkelsen, *Phys. Rev. Lett.* 109 (2012) 026101.
[344] A. Ambrosi, A. Bonanni, Z. Sofer, M. Pumera, *Nanoscale* 5 (2013) 2379–2387.
[345] R.G. Compton, C.E. Banks, *Understanding Voltammetry*, 2nd ed., Imperial College Press, London, 2011.
[346] A. Ambrosi, M. Pumera, *J. Phys. Chem. C* 117 (2013) 2053–2058.
[347] J. Xu, W. Huang, R.L. Mccreery, *J. Electroanal. Chem.* 410 (1996) 235–242.
[348] K.R. Kneten, R.L. McCreery, *Anal. Chem.* 64 (1992) 2518–2524.
[349] T. Menanteau, E. Levillain, T. Breton, *Chem. Mater.* 25 (2013) 2905–2909.
[350] P. Mendes, M. Belloni, M. Ashworth, C. Hardy, K. Nikitin, D. Fitzmaurice, K. Critchley, S. Evans, J. Preece, *ChemPhysChem* 4 (2003) 884–889.
[351] A.K. Farquhar, C.M. Fitchett, H.M. Dykstra, M.R. Waterland, P.A. Brooksby, A.J. Downard, *ACS Appl. Mater. Interfaces* 8 (2016) 23389–23395.

[352] M. Ceccato, L.T. Nielsen, J. Iruthayaraj, M. Hinge, S.U. Pedersen, K. Daasbjerg, *Langmuir* 26 (2010) 10812–10821.
[353] J.G. Lin-Vien, D., Colthup, N.B., Fateley, W.G. and Grasselli, *The Handbook of Infrared and Raman Characteristic Frequencies of Organic Molecules*, Academic Press, San Diego, 1991.
[354] X. Dong, Q. Long, A. Wei, W. Zhang, L.J. Li, P. Chen, W. Huang, *Carbon* 50 (2012) 1517–1522.
[355] M.A. Bissett, S. Konabe, S. Okada, M. Tsuji, H. Ago, *ACS Nano* 7 (2013) 10335–10343.
[356] G.L.C. Paulus, Q.H. Wang, M.S. Strano, *Acc. Chem. Res.* 46 (2013) 160–170.
[357] P.M. Kirkman, A.G. Güell, A.S. Cuharuc, P.R. Unwin, *J. Am. Chem. Soc.* 136 (2014) 36–39.
[358] H. Ma, L. Lee, P.A. Brooksby, S.A. Brown, S.J. Fraser, K.C. Gordon, Y.R. Leroux, P. Hapiot, A.J. Downard, S. Chimiques, E. Macse, U. De Rennes, C. De Beaulieu, (2014).
[359] J. Greenwood, T.H. Phan, Y. Fujita, Z. Li, O. Ivasenko, W. Vanderlinden, H. Van Gorp, W. Frederickx, G. Lu, K. Tahara, Y. Tobe, H. Uji-I, S.F.L. Mertens, S. De Feyter, *ACS Nano* 9 (2015) 5520–5535.
[360] D.E. Jiang, B.G. Sumpter, S. Dai, *J. Phys. Chem. B* 110 (2006) 23628–23632.
[361] K. Kukli, J. Aarik, M. Ritala, T. Uustare, T. Sajavaara, J. Lu, J. Sundqvist, A. Aidla, L. Pung, A. Hårsta, M. Leskelä, *J. Appl. Phys.* 96 (2004) 5298–5307.
[362] R. He, L. Zhao, N. Petrone, K.S. Kim, M. Roth, J. Hone, P. Kim, A. Pasupathy, A. Pinczuk, *Nano Lett.* 12 (2012) 2408–2413.
[363] C. Neumann, S. Reichardt, P. Venezuela, M. Drögeler, L. Banszerus, M. Schmitz, K. Watanabe, T. Taniguchi, F. Mauri, B. Beschoten, S. V. Rotkin, C. Stampfer, *Nat. Commun.* 6 (2015) 8429.
[364] Z.T. Wu, W. Zhao, Y. Chen, J. Jiang, Y. Nan, *J. Raman Spectrosc.* 46 (2015) 21–24.

PUBLICATIONS

CURRICULUM VITAE

Name: Jekaterina Kozlova (Kapšai)
Date of birth: 23.06.1985
Citizenship: Estonian
Address: Institute of Physics, University of Tartu, W. Ostwaldi 1, 50411, Tartu, Estonia
Telephone: +372 5805 3316
E-mail address: jekaterina.kozlova@ut.ee

Education:

2009–2019	University of Tartu, PhD student, material science
2007–2009	University of Tartu, Master degree in inorganic chemistry
2004–2007	University of Tartu, Bachelor degree in chemistry
2001–2004	Tallinna Lasnamäe Gymnasium

Professional employment:

01.06.2009– University of Tartu, Institute of Physics, University of Tartu, Laboratory of Thin-Film Technology, engineer

01.01.2008–28.02.2009
University of Tartu, Institute of Physics, laboratory assistant

Language skills:
Russian, native; Estonian, good; English, good

List of publications:

1. V. Kiisk, K. Akulitš, M. Kodu, T. Avarmaa, H. Mändar, **J. Kozlova**, M. Eltermann, L. Puust, R. Jaaniso, Oxygen-Sensitive Photoluminescence of Rare Earth Ions in TiO_2 Thin Films. *The Journal of Physical Chemistry C* 123 (2019) 17908–17914.
2. M. Kirm, M. Oja, **J. Kozlova**, H. Mändar, S. Vielhauer, T. Jansen, T. Jüstel, N. M. Khaidukov, V. N. Makhov, Spectral Properties and Thermal Quenching of Mn^{4+} Luminescence in Silicate Garnet Hosts $CaY_2MgMAlSi_2O_{12}$ (M= Al, Ga, Sc), *Physics of the Solid State* 61 (2019) 853–859.
3. L. Aarik, **J. Kozlova**, H. Mändar, J. Aarik, V. Sammelselg, Chemical resistance of TiO_2 and Al_2O_3 single-layer and multilayer coatings atomic layer deposited from hydrogen-free precursors on silicon and stainless steel, *Materials Chemistry and Physics* 228 (2019) 285–292.
4. M. Käärik, M. Arulepp, M. Kook, **J. Kozlova**, P. Ritslaid, J. Aruväli, U. Mäeorg, V. Sammelselg, J. Leis, High-performance microporous carbon from deciduous wood-origin metal carbide, *Microporous and Mesoporous Materials*, 278 (2019) 14–22.

5. A. Vanetsev, P. Põdder, S. Vielhauer, E. Feldbach, **J. Kozlova**, V. Nagirnyi, H. Mändar, I. Romet, V. Sammelselg, V. Makhov, M. Kirm, Soft chemical synthesis and luminescent properties of $Na_3Al_2Li_3F_{12}:Mn^{4+}$ garnet-type nanophosphor, *Optical Materials* 89 (2019) 340–343.
6. T. Jansen, T. Jüstel, M. Kirm, **J. Kozlova**, H. Mändar, S. Vielhauer, N. M. Khaidukov, Makhov, Thermal quenching of Mn^{4+} luminescence in Sn^{4+}–containing garnet hosts, *Optical Materials* 84 (2018) 600–605.
7. J. M. Linge, H. Erikson, **J. Kozlova**, J. Aruväli, V. Sammelselg, K. Tammeveski, Oxygen reduction on electrodeposited silver catalysts in alkaline solution, *Journal of Solid State Electrochemistry* 22 (2018) 81–89.
8. J. M. Linge, H. Erikson, **J. Kozlova**, V. Sammelselg, K. Tammeveski, Oxygen reduction reaction on electrochemically deposited silver nanoparticles from non-aqueous solution, *Journal of Electroanalytical Chemistry*, 810 (2018) 129–134.
9. M. Käärik, M. Arulepp, M. Kook, U. Mäeorg, **J. Kozlova**, V. Sammelselg, A. Perkson, J. Leis, Characterisation of steam-treated nanoporous carbide-derived carbon of TiC origin: structure and enhanced electrochemical performance, *Journal of Porous Materials* 25 (2018) 1057–1070.
10. M. Laan, A. Hakola, P. Paris, K. Piip, M. Aints, I. Jõgi, **J. Kozlova**, H. Mändar, C. Lungu, C. Porosnicu, E. Grigore, C. Ruset, J. Kolehmainen, S. Tervakangas, Dependence of LIBS spectra on the surface composition and morphology of W/Al coating, *Fusion Engineering and Design* 121 (2017) 296–300.
11. S. Hussain, N. Kongi, L. Matisen, **J. Kozlova**, V. Sammelselg, K. Tammeveski, Platinum nanoparticles supported on nitrobenzene-functionalised graphene nanosheets as electrocatalysts for oxygen reduction reaction in alkaline media, *Electrochemistry Communications* 81 (2017) 79–83.
12. K. Piip, H. Meiden, L. Hämarik, J. Karhunen, A. Hakola, M. Laan, P. Paris, M. Aints, L. Likonen, K. Bystrov, **J. Kozlova**, A. Zaloznik, M. Kelemen, S. Markelj, LIBS detection of erosion/deposition and deuterium retention resulting from exposure to Pilot-PSI plasmas, *Journal of Nuclear Material*, 489 (2017) 129–136.
13. P. Uudeküll, **J. Kozlova**, H. Mändar, J. Link, M. Sihtmäe, S. Käosaar, I. Blinova, K. Kasemets, A. Kahru, R. Stern, T. Tätte, K. Kukli, A. Tamm, Atomic layer deposition of titanium oxide films on as-synthesized magnetic Ni particles: Magnetic and safety properties, *Journal of Magnetism and Magnetic Materials* 429 (2017) 299–304.
14. A. Tamm, L. Seinberg, **J. Kozlova**, J. Link, P. Pikma, R. Stern, K. Kukli, Quasicubic α-Fe_2O_3 nanoparticles embedded in TiO_2 thin films grown by atomic layer deposition, *Thin Solid Films* 612 (2016) 445–449.
15. J. Mondal, A. Marques, L. Aarik, **J. Kozlova**, A. Simões, V. Sammelselg, Development of thin ceramic-graphene nanolaminated coating for corrosion protection of stainless steel, *Corrosion Science* 105 (2016) 161–169.

16. A. Niilisk, **J. Kozlova**, H. Alles, J. Aarik, V. Sammelselg, Raman characterization of stacking in multi-layer graphene grown on Ni, *Carbon* 98 (2016) 658–665.
17. K.-K. Türk, I. Kruusenberg, J. Mondal, P. Rauwel, **J. Kozlova**, L. Matisen, V. Sammelselg, K. Tammeveski, Oxygen electroreduction on MN_4-macrocycle modified graphene/multi-walled carbon nanotube composites, *Journal of Electroanalytical Chemistry* 756 (2015) 69–76.
18. H. Castán, S. Dueñas, H. García, B. Bailón, K. Kukli, A. Tamm, **J. Kozlova**, J. Aarik, K. Mizohata, Charge and current hysteresis in dysprosium-doped zirconium oxide thin films, *Microelectronic Engineering* 147 (2015) 55–58.
19. **J. Kozlova**, A. Niilisk, H. Alles, V. Sammelselg, Discontinuity and misorientation of graphene grown on nickel foil: Effect of the substrate crystallographic orientation, *Carbon* 94 (2015) 160–173.
20. J.Mondal, L. Aarik, **J. Kozlova**, A. Niilisk, H. Mändar, U. Mäeorg, A. Simões, V. Sammelselg, Functionalization of Titanium Alloy Surface by Graphene Nanoplatelets and Metal Oxides: Corrosion Inhibition, *J. Nanosci. Nanotechnol*. 15 (2015) 6533–6540.
21. J. Mondal, **J. Kozlova**, V. Sammelselg, Graphene Nanoplatelets Based Protective and Functionalizing Coatings for Stainless Steel, *J. Nanosci. Nanotechnol*. 15 (2015) 6747–6750.
22. A. Tamm, **J. Kozlova**, T. Arroval, J. Aarik, P. Ritslaid, H. Garcıa, H. Castan, S. Duenas, K. Kukli, J. Aarik, Atomic Layer Deposition and Characterization of Dysprosium-Doped Zirconium Oxide Thin Films, *Chemical Vapor Deposition* 21 (2015) 181–187.
23. I. Shypunov, N. Kongi, **J. Kozlova**, L. Matisen, P. Ritslaid, V. Sammelselg, K. Tammeveski, Enhanced oxygen reduction reaction activity with electrodeposited Ag on manganese oxide–graphene supported electrocatalyst, *Electrocatalysis* 6 (2015) 465–471.
24. K. Piip, G. De Temmerman, H. J. van der Meiden, A. Lissovski, J. Karhunen, M. Aints, A. Hakola, P. Paris, M. Laan, J. Likonen, I. Jõgi, **J. Kozlova**, H. Mändar, LIBS analysis of tungsten coatings exposed to Magnum PSI ELM-like plasma, *Journal of Nuclear Materials* 463 (2015) 919–922.
25. A. Kuznetsov, A. Frorip, **J. Kozlova**, V. Nagirnyi, M. Ots-Rosenberg, I. Romet, A. Sünter, Visible fluorescence of biological fluids as a renal failure marker: New integrative approach, *Journal of Innovative Optical Health Sciences* 8 (2015) 1550030.
26. T. Jõgiaas, L. Kollo, **J. Kozlova**, A. Tamm, I. Hussainova, K. Kukli, Effect of Atomic Layer Deposited Aluminium Oxide on Mechanical Properties of Porous Silicon Carbide, *Ceramics International* 41 (2015) 7519–7528.
27. V. Kiisk, A. Tamm, K. Utt, **J. Kozlova**, H. Mändar, L. Puust, J. Aarik, I. Sildos, Photoluminescence of atomic layer deposited ZrO_2:Dy^{3+} thin films, *Thin Solid Films* 583 (2015) 70–75.
28. M. Mooste, E. Kibena, **J. Kozlova**, M. Marandi, L. Matisen, A. Niilisk, V. Sammelselg, K. Tammeveski, Electrografting and morphological studies

of chemical vapour deposition grown graphene sheets modified by electroreduction of aryldiazonium salts, *Electrochimica Acta* 161 (2015) 195–204.
29. U. Paaver, J. Heinämäki, L. Laidmäe, A. Lust, **J. Kozlova**, E. Sillaste, K. Kirsimäe, P. Veski, K. Kogermann, Electrospun nanofibers as a potential controlled-release solid dispersion system for poorly water-soluble drugs, *International Journal of Pharmaceutics* 479 (2015) 252–260.
30. M. Merisalu, T. Kahro, **J. Kozlova**, A. Niilisk, A. Nikolajev, M. Marandi, A. Floren, H. Alles, V. Sammelselg, Graphene-polypyrrole thin hybrid corrosion resistant coatings for copper, *Synthetic Metals* 200 (2015) 16–23.
31. A. Tamm, **J. Kozlova**, L. Aarik, J. Aarik, K. Kukli, J. Link, R. Stern, Dysprosium oxide and dysprosium-oxide-doped titanium oxide thin films grown by atomic layer deposition, *Journal of Vacuum Science & Technology A-Vacuum Surfaces and Films* 33 (2015) 01A127.
32. H. Erikson, A. Sarapuu, **J. Kozlova**, L. Matisen, V. Sammelselg, K. Tammeveski, Oxygen electroreduction on electrodeposited PdAu nanoalloys, *Electrocatalysis* 6 (2015) 77–85.
33. K. Jukk, N. Kongi, A. Tarre, A. Rosental, A.B. Treshchalov, **J. Kozlova**, P. Ritslaid, L. Matisen, V. Sammelselg, K. Tammeveski, Electrochemical oxygen reduction behavior of platinum nanoparticles supported on carbon nanotube/titanium dioxide composites, *Journal of Electroanalytical Chemistry* 735 (2014) 68–76.
34. K. Piip, P. Paris, A. Hakola, K. Bystrov, G. De Temmerman, M. Aints, I. Jõgi, **J. Kozlova**, M. Laan, J. Likonen, A. Lissovski, H. Mändar, Influence of He/D_2 plasma fluxes on the morphology and crystallinity of tungsten coatings, *Physica Scripta* 89 (2014) 044009.
35. U. Paaver, J. Heinämäki, I. Kassamakov, E. Hæggström, T. Ylitalo, A. Nolvi, **J. Kozlova**, I. Laidmäe, K. Kogermann, P. Veski, Nanometer depth resolution in 3D topographic analysis of drug-loaded nanofibrous mats without sample preparation, *International Journal of Pharmaceutics* 462 (2014) 29–37.
36. M. Part, A. Tamm, **J. Kozlova**, H. Mändar, T. Tätte, K. Kukli, Atomic layer deposition of MgO films on yttria-stabilized zirconia microtubes, *Thin Solid Films* 553 (2014) 30–32.
37. A. Tamm, **J. Kozlova**, L. Aarik, A. Aidla, J. Lu, A.-A. Kiisler, A. Kasikov, P. Ritslaid, H. Mändar, L. Hultman, V. Sammelselg, K. Kukli, J. Aarik, Atomic layer deposition of ZrO_2 for graphene-based multilayer structures: In situ and ex situ characterization of growth process, *Physica Status Solidi A – Applications and Materials Science* 211 (2014) 397–402.
38. T. Jõgiaas, T. Arroval, L. Kollo, **J. Kozlova**, T. Käämbre, H. Mändar, A. Tamm, I. Hussainova, K. Kukli, Atomic layer deposition of alumina on γ-Al_2O_3 nanofibers, *Physica Status Solidi A – Applications and Materials Science* 211 (2014) 403–408.
39. R. Jaaniso, T. Kahro, **J. Kozlova**, J. Aarik, L. Aarik, H. Alles, A. Floren, A. Gerst, A. Kasikov, A. Niilisk, V. Sammelselg, Temperature induced

inversion of oxygen response in CVD graphene on SiO_2, *Sensors and Actuators B-Chemical* 190 (2014) 1006–1013.
40. A. Lust, S. Lakio, J. Vintsevits, **J. Kozlova**, P. Veski, J. Heinämäki, K. Kogermann, Water-mediated solid-state transformation of a polymorphic drug during aqueous-based drug-layer coating of pellets, *International Journal of Pharmaceutics* 456 (2013) 41–48.
41. K. Jukk, N. Alexeyeva, P. Ritslaid, **J. Kozlova**, V. Sammelselg, K. Tammeveski, Sputter-deposited Pt nanoparticle/multi-walled carbon nanotube composite catalyst for oxygen reduction reaction, *Journal of Electroanalytical Chemistry* 708 (2013) 31–38.
42. E. Kibena, M. Mooste, **J. Kozlova**, M. Marandi, V. Sammelselg, K. Tammeveski, Surface and electrochemical characterisation of CVD grown graphene sheets, *Electrochemistry Communications* 35 (2013) 26–29.
43. A. Hallik, A. Alumaa, **J. Kozlova**, J. Tamm, V. Sammelselg, The dopant concentration profiles in PPy/DDS/Cl and PPy/Cl/DDS bilayers, *Synthetic Metals* 181 (2013) 123–128.
44. P. Paris, A. Hakola, K. Bystrov, G. Temmerman, M. Aints, I. Jõgi, M. Kiisk, **J. Kozlova**, M. Laan, J. Likonen, A. Lissovski, Erosion of marker coatings exposed to Pilot-PSI plasma, *Journal of Nuclear Materials* 438 (2013) S754–S757.
45. V. Kiisk, T. Kahro, **J. Kozlova**, L. Matisen, H. Alles, Nanosecond laser treatment of graphene, *Applied Surface Science* 276 (2013) 133–137.
46. A. Tamm, A.L. Peikolainen, **J. Kozlova**, H. Mändar, A. Aidla, R. Rammula, L. Aarik, K. Roosalu, J. Lu, L. Hultman, M. Koel, K. Kukli, J. Aarik, Atomic layer deposition of high-k dielectrics on carbon nanoparticles, *Thin Solid Films* 538 (2013) 16–20.
47. K. Jukk, N. Alexeyeva, A. Sarapuu, P. Ritslaid, **J. Kozlova**, V. Sammelselg, K. Tammeveski, Electroreduction of oxygen on sputter-deposited Pd nanolayers on multi-walled carbon nanotubes, *International Journal of Hydrogen Energy* 38 (2013) 3614–3620.
48. K. Jukk, N. Alexeyeva, P. Ritslaid, **J. Kozlova**, V. Sammelselg, K. Tammeveski, Electrochemical Reduction of Oxygen on Heat-Treated Pd Nanoparticle/Multi-Walled Carbon Nanotube Composites in Alkaline Solution, *Electrocatalysis* 4 (2013) 42–48.
49. H. Erikson, M. Liik, A. Sarapuu, **J. Kozlova**, V. Sammelselg, K. Tammeveski, Oxygen reduction on electrodeposited Pd coatings on glassy carbon, *Electrochimica Acta* 88 (2013) 513–518.
50. L. Tammeveski, H. Erikson, A. Sarapuu, **J. Kozlova**, P. Ritslaid, V. Sammelselg, K. Tammeveski, Electrocatalytic oxygen reduction on silver nanoparticle/multi-walled carbon nanotube modified glassy carbon electrodes in alkaline solution, *Electrochemistry Communications* 20 (2012) 15–18.
51. A. Tamm, M. Dimri, **J. Kozlova**, A. Aidla, T. Tätte, T. Arroval, U. Mäeorg, H. Mändar, R. Stern, K. Kukli, Atomic layer deposition of ferromagnetic iron oxide films on three-dimensional substrates with tin oxide nanoparticles, *Journal of Crystal Growth* 343 (2012) 21–27.

52. I. Kruusenberg, N. Alexeyeva, K. Tammeveski, **J. Kozlova**, L. Matisen, V. Sammelselg, J. Solla-Gullo, J. Feliu, Effect of purification of carbon nanotubes on their 3 electrocatalytic properties for oxygen reduction 4 in acid solution, *Carbon* 11 (2011) 4031–4039.
53. H. Alles, J. Aarik, A. Aidla, A. Fay, **J. Kozlova**, A. Niilisk, M. Pärs, M. Rähn, M. Wiesner, P. Hakonen, V. Sammelselg, Atomic layer deposition of HfO_2 on graphene from $HfCl_4$ and H_2O, *Central European Journal of Physics* 9 (2011) 319–324.
54. A. Tamm, M. Heikkilä, M. Kemell, **J. Kozlova**, K. Kukli, V. Sammelselg, M. Ritala, M. Leskelä, Atomic layer deposition and characterization of zirconium oxide–erbium oxide nanolaminates, *Thin Solid Films* 519 (2010) 666–673.
55. M. Kullapere, **J. Kozlova**, L. Matisen, V. Sammelselg, H.A. Menezes, G. Maia, D.J. Schiffrin, K. Tammeveski, Electrochemical properties of aryl-modified gold electrodes, *Journal of Electroanalytical Chemistry* 641 (2010) 90–98.
56. N. Alexeyeva, **J. Kozlova**, V. Sammelselg, P. Ritslaid, H. Mändar, K. Tammeveski, Electrochemical and surface characterisation of gold nanoparticle decorated multi-walled carbon nanotubes, *Applied Surface Science* 256 (2010) 3040–3046.
57. A. Tamm, M. Kemell, **J. Kozlova**, T. Sajavaara, M. Tallarida, K. Kukli, V. Sammelselg, M. Ritala, M. Leskelä, Atomic layer deposition and characterization of erbium oxide-doped zirconium oxide thin films, *Journal of the Electrochemical Society* 157 (2010) G193–G201.

Presentations at conferences:

1. J. Kozlova, A. Niilisk, H. Alles, V. Sammelselg, Inhomogeneity of graphene growth on nickel foils by chemical vapor deposition, poster presentation at FMTDK conference, 04.03.14, Tartu.
2. J. Kozlova, A. Niilisk, A. Kasikov, T. Kahro, H. Alles, V. Sammelselg, Graphene synthesis on polycrystalline and epitaxial nickel films, poster presentation at FMTDK conference, 07.05.13, Tallinn.
3. J. Kozlova, A. Niilisk, A. Kasikov, A. Gerst, T. Kahro, H. Alles, V. Sammelselg "Quality of graphene prepared by CVD method on nickel", poster presentation at NT13 Fourteenth International Conference on the Science and Application of Nanotubes, 28.06.13, Tallinn.
4. J. Kozlova, A. Niilisk, A. Kasikov, A. Gerst, T. Kahro, A. Tõnisoo, H. Alles, V. Sammelselg, Graphene synthesis on nickel, poster presentation at E-MRS, 30.05.13, Strasbourg, France.
5. J. Kozlova, A. Niilisk, A. Kasikov, A. Gerst, T. Kahro, A. Tõnisoo, H. Alles, V. Sammelselg, Characterization of graphene prepared by chemical vapor deposition on nickel, poster presentation at FM&NT, 22.04.13, Tartu.

6. V. Sammelselg, M. Merisalu, J. Mondal, L. Aarik, A. Tamm, A.-L. Peikolainen, J. Kozlova, M. Marandi, M. Pala, J. Aarik, Study of atomic layer deposited oxide thin coatings on carbon based materials/metal substrates, poster presentation at 12th International Conference on Atomic Layer Deposition, 17.06.12 – 20.06.12, Dresden
7. J. Kozlova, T. Kahro, A. Niilisk, H. Alles, V. Sammelselg "Using large-area graphene prepared by chemical vapor deposition for gas sensorics", oral presentation at FMTDK conference, 29.02.12, Tartu
8. J. Kozlova, H. Alles, J. Aarik, A. Niilisk, V. Sammelselg, Elektronkiirega kiiritatud grafeeni struktuuri uurimine, XXXI Days of Chemistry, 2011, Tartu.
9. J. Kozlova, H. Alles, J. Aarik, A. Niilisk, V. Sammelselg, Microscopy studies of HfO_2 on graphene, poster presentation at FM&NT Conference, 16.03.10, Riga.
10. J. Kozlova, H. Alles, J. Aarik, A. Niilisk, V. Sammelselg, HfO_2/grafeen struktuuride mikroskoopiline uurimine", oral presentation at FMTDK conference 25.02.10–26.02.10, Tartu
11. J. Kapšai, T. Rinken, V. Sammelselg, Atomic force microscopy study of enzyme glucose oxidase deposited onto solid, poster presentation at XI.Annual Linz Winter Workshop, 6–9.02.09, Linz, Austria. Johannes Kepler University of Linz.

ELULOOKIRJELDUS

Nimi: Jekaterina Kozlova (Kapšai)
Sünniaeg: 23.06.1985
Kodakondsus: Eesti
Kontaktandmed: Tartu Ülikool, Füüsika Instituut, W. Ostwaldi 1, 50411, Tartu, Eesti
Telefon: +372 5805 3316
E-post: jekaterina.kozlova@ut.ee

Haridus:

2009–2019	Tartu Ülikool, Doktoriõpe, Materjaliteadus
2007–2009	Tartu Ülikool, Anorgaaniline keemia M.Sc.
2004–2007	Tartu Ülikool, Keemia, B.Sc.
2001–2004	Tallinna Lasnamäe Gümnaasium

Töökogemus:

01.06.2009–	Tartu Ülikool, Füüsika Instituut, Kiletehnoloogia labor, insener
01.01.2008–28.02.2009	Tartu Ülikool, Füüsika Instituut, Kiletehnoloogia labor, laborant

Keelteoskus:
vene keel, emakeel; eesti keel, hea; inglise keel, hea

Publikatsioonid:

1. V. Kiisk, K. Akulitš, M. Kodu, T. Avarmaa, H. Mändar, **J. Kozlova,** M. Eltermann, L. Puust, R. Jaaniso, Oxygen-Sensitive Photoluminescence of Rare Earth Ions in TiO_2 Thin Films. *The Journal of Physical Chemistry C* 123 (2019) 17908–17914.
2. M. Kirm, M. Oja, **J. Kozlova**, H. Mändar, S. Vielhauer, T. Jansen, T. Jüstel, N.M. Khaidukov, V.N. Makhov, Spectral Properties and Thermal Quenching of Mn^{4+} Luminescence in Silicate Garnet Hosts $CaY_2MgMAlSi_2O_{12}$ (M= Al, Ga, Sc), *Physics of the Solid State* 61 (2019) 853–859.
3. L. Aarik, **J. Kozlova**, H. Mändar, J. Aarik, V. Sammelselg, Chemical resistance of TiO_2 and Al_2O_3 single-layer and multilayer coatings atomic layer deposited from hydrogen-free precursors on silicon and stainless steel, *Materials Chemistry and Physics* 228 (2019) 285–292.
4. M. Käärik, M. Arulepp, M. Kook, **J. Kozlova**, P. Ritslaid, J. Aruväli, U. Mäeorg, V. Sammelselg, J. Leis, High-performance microporous carbon from deciduous wood-origin metal carbide, *Microporous and Mesoporous Materials*, 278 (2019) 14–22.

5. A. Vanetsev, P. Põdder, S. Vielhauer, E. Feldbach, **J. Kozlova**, V. Nagirnyi, H. Mändar, I. Romet, V. Sammelselg, V. Makhov, M. Kirm, Soft chemical synthesis and luminescent properties of $Na_3Al_2Li_3F_{12}:Mn^{4+}$ garnet-type nanophosphor, *Optical Materials* 89 (2019) 340–343.
6. T. Jansen, T. Jüstel, M. Kirm, **J. Kozlova**, H. Mändar, S. Vielhauer, N.M. Khaidukov, Makhov, Thermal quenching of Mn^{4+} luminescence in Sn^{4+}–containing garnet hosts, *Optical Materials* 84 (2018) 600–605.
7. J.M. Linge, H. Erikson, **J. Kozlova**, J. Aruväli, V. Sammelselg, K. Tammeveski, Oxygen reduction on electrodeposited silver catalysts in alkaline solution, *Journal of Solid State Electrochemistry* 22 (2018) 81–89.
8. J.M. Linge, H. Erikson, **J. Kozlova**, V. Sammelselg, K. Tammeveski, Oxygen reduction reaction on electrochemically deposited silver nanoparticles from non-aqueous solution, *Journal of Electroanalytical Chemistry*, 810 (2018) 129–134.
9. M. Käärik, M. Arulepp, M. Kook, U. Mäeorg, **J. Kozlova**, V. Sammelselg, A. Perkson, J. Leis, Characterisation of steam-treated nanoporous carbide-derived carbon of TiC origin: structure and enhanced electrochemical performance, *Journal of Porous Materials* 25 (2018) 1057–1070.
10. M. Laan, A. Hakola, P. Paris, K. Piip, M. Aints, I. Jõgi, **J. Kozlova**, H. Mändar, C. Lungu, C. Porosnicu, E. Grigore, C. Ruset, J. Kolehmainen, S. Tervakangas, Dependence of LIBS spectra on the surface composition and morphology of W/Al coating, *Fusion Engineering and Design* 121 (2017) 296–300.
11. S. Hussain, N. Kongi, L. Matisen, **J. Kozlova**, V. Sammelselg, K. Tammeveski, Platinum nanoparticles supported on nitrobenzene-functionalised graphene nanosheets as electrocatalysts for oxygen reduction reaction in alkaline media, *Electrochemistry Communications* 81 (2017) 79–83.
12. K. Piip, H. Meiden, L. Hämarik, J. Karhunen, A. Hakola, M. Laan, P. Paris, M. Aints, L. Likonen, K. Bystrov, **J. Kozlova**, A. Zaloznik, M. Kelemen, S. Markelj, LIBS detection of erosion/deposition and deuterium retention resulting from exposure to Pilot-PSI plasmas, *Journal of Nuclear Material*, 489 (2017) 129–136.
13. P. Uudeküll, **J. Kozlova**, H. Mändar, J. Link, M. Sihtmäe, S. Käosaar, I. Blinova, K. Kasemets, A. Kahru, R. Stern, T. Tätte, K. Kukli, A. Tamm, Atomic layer deposition of titanium oxide films on as-synthesized magnetic Ni particles: Magnetic and safety properties, *Journal of Magnetism and Magnetic Materials* 429 (2017) 299–304.
14. A. Tamm, L. Seinberg, **J. Kozlova**, J. Link, P. Pikma, R. Stern, K. Kukli, Quasicubic α-Fe_2O_3 nanoparticles embedded in TiO_2 thin films grown by atomic layer deposition, *Thin Solid Films* 612 (2016) 445–449.
15. J. Mondal, A. Marques, L. Aarik, **J. Kozlova**, A. Simões, V. Sammelselg, Development of thin ceramic-graphene nanolaminated coating for corrosion protection of stainless steel, *Corrosion Science* 105 (2016) 161–169.

16. A. Niilisk, **J. Kozlova**, H. Alles, J. Aarik, V. Sammelselg, Raman characterization of stacking in multi-layer graphene grown on Ni, *Carbon* 98 (2016) 658–665.
17. K.-K. Türk, I. Kruusenberg, J. Mondal, P. Rauwel, **J. Kozlova**, L. Matisen, V. Sammelselg, K. Tammeveski, Oxygen electroreduction on MN_4-macrocycle modified graphene/multi-walled carbon nanotube composites, *Journal of Electroanalytical Chemistry* 756 (2015) 69–76.
18. H. Castán, S. Dueñas, H. García, B. Bailón, K. Kukli, A. Tamm, **J. Kozlova**, J. Aarik, K. Mizohata, Charge and current hysteresis in dysprosium-doped zirconium oxide thin films, *Microelectronic Engineering* 147 (2015) 55–58.
19. **J. Kozlova**, A. Niilisk, H. Alles, V. Sammelselg, Discontinuity and misorientation of graphene grown on nickel foil: Effect of the substrate crystallographic orientation, *Carbon* 94 (2015) 160–173.
20. J. Mondal, L. Aarik, **J. Kozlova**, A. Niilisk, H. Mändar, U. Mäeorg, A. Simões, V. Sammelselg, Functionalization of Titanium Alloy Surface by Graphene Nanoplatelets and Metal Oxides: Corrosion Inhibition, *J. Nanosci. Nanotechnol*. 15 (2015) 6533–6540.
21. J. Mondal, **J. Kozlova**, V. Sammelselg, Graphene Nanoplatelets Based Protective and Functionalizing Coatings for Stainless Steel, *J. Nanosci. Nanotechnol*. 15 (2015) 6747–6750.
22. A. Tamm, **J. Kozlova**, T. Arroval, J. Aarik, P. Ritslaid, H. Garcıa, H. Castan, S. Duenas, K. Kukli, J. Aarik, Atomic Layer Deposition and Characterization of Dysprosium-Doped Zirconium Oxide Thin Films, *Chemical Vapor Deposition* 21 (2015) 181–187.
23. I. Shypunov, N. Kongi, **J. Kozlova**, L. Matisen, P. Ritslaid, V. Sammelselg, K. Tammeveski, Enhanced oxygen reduction reaction activity with electrodeposited Ag on manganese oxide–graphene supported electrocatalyst, *Electrocatalysis* 6 (2015) 465–471.
24. K. Piip, G. De Temmerman, H. J. van der Meiden, A. Lissovski, J. Karhunen, M. Aints, A. Hakola, P. Paris, M. Laan, J. Likonen, I. Jõgi, **J. Kozlova**, H. Mändar, LIBS analysis of tungsten coatings exposed to Magnum PSI ELM-like plasma, *Journal of Nuclear Materials* 463 (2015) 919–922.
25. A. Kuznetsov, A. Frorip, **J. Kozlova**, V. Nagirnyi, M. Ots-Rosenberg, I. Romet, A. Sünter, Visible fluorescence of biological fluids as a renal failure marker: New integrative approach, *Journal of Innovative Optical Health Sciences* 8 (2015) 1550030.
26. T. Jõgiaas, L. Kollo, **J. Kozlova**, A. Tamm, I. Hussainova, K. Kukli, Effect of Atomic Layer Deposited Aluminium Oxide on Mechanical Properties of Porous Silicon Carbide, *Ceramics International* 41 (2015) 7519–7528.
27. V. Kiisk, A. Tamm, K. Utt, **J. Kozlova**, H. Mändar, L. Puust, J. Aarik, I. Sildos, Photoluminescence of atomic layer deposited ZrO_2:Dy^{3+} thin films, *Thin Solid Films* 583 (2015) 70–75.
28. M. Mooste, E. Kibena, **J. Kozlova**, M. Marandi, L. Matisen, A. Niilisk, V. Sammelselg, K. Tammeveski, Electrografting and morphological studies

of chemical vapour deposition grown graphene sheets modified by electro-reduction of aryldiazonium salts, *Electrochimica Acta* 161 (2015) 195–204.
29. U. Paaver, J. Heinämäki, L. Laidmäe, A. Lust, **J. Kozlova**, E. Sillaste, K. Kirsimäe, P. Veski, K. Kogermann, Electrospun nanofibers as a potential controlled-release solid dispersion system for poorly water-soluble drugs, *International Journal of Pharmaceutics* 479 (2015) 252–260.
30. M. Merisalu, T. Kahro, **J. Kozlova**, A. Niilisk, A. Nikolajev, M. Marandi, A. Floren, H. Alles, V. Sammelselg, Graphene-polypyrrole thin hybrid corrosion resistant coatings for copper, *Synthetic Metals* 200 (2015) 16–23.
31. A. Tamm, **J. Kozlova**, L. Aarik, J. Aarik, K. Kukli, J. Link, R. Stern, Dysprosium oxide and dysprosium-oxide-doped titanium oxide thin films grown by atomic layer deposition, *Journal of Vacuum Science & Technology A-Vacuum Surfaces and Films* 33 (2015) 01A127.
32. H. Erikson, A. Sarapuu, **J. Kozlova**, L. Matisen, V. Sammelselg, K. Tammeveski, Oxygen electroreduction on electrodeposited PdAu nanoalloys, *Electrocatalysis* 6 (2015) 77–85.
33. K. Jukk, N. Kongi, A. Tarre, A. Rosental, A.B. Treshchalov, **J. Kozlova**, P. Ritslaid, L. Matisen, V. Sammelselg, K. Tammeveski, Electrochemical oxygen reduction behavior of platinum nanoparticles supported on carbon nanotube/titanium dioxide composites, *Journal of Electroanalytical Chemistry* 735 (2014) 68–76.
34. K. Piip, P. Paris, A. Hakola, K. Bystrov, G. De Temmerman, M. Aints, I. Jõgi, **J. Kozlova**, M. Laan, J. Likonen, A. Lissovski, H. Mändar, Influence of He/D_2 plasma fluxes on the morphology and crystallinity of tungsten coatings, *Physica Scripta* 89 (2014) 044009.
35. U. Paaver, J. Heinämäki, I. Kassamakov, E. Hæggström, T. Ylitalo, A. Nolvi, **J. Kozlova**, I. Laidmäe, K. Kogermann, P. Veski, Nanometer depth resolution in 3D topographic analysis of drug-loaded nanofibrous mats without sample preparation, *International Journal of Pharmaceutics* 462 (2014) 29–37.
36. M. Part, A. Tamm, **J. Kozlova**, H. Mändar, T. Tätte, K. Kukli, Atomic layer deposition of MgO films on yttria-stabilized zirconia microtubes, *Thin Solid Films* 553 (2014) 30–32.
37. A. Tamm, **J. Kozlova**, L. Aarik, A. Aidla, J. Lu, A.-A. Kiisler, A. Kasikov, P. Ritslaid, H. Mändar, L. Hultman, V. Sammelselg, K. Kukli, J. Aarik, Atomic layer deposition of ZrO_2 for graphene-based multilayer structures: In situ and ex situ characterization of growth process, *Physica Status Solidi A – Applications and Materials Science* 211 (2014) 397–402.
38. T. Jõgiaas, T. Arroval, L. Kollo, **J. Kozlova**, T. Käämbre, H. Mändar, A. Tamm, I. Hussainova, K. Kukli, Atomic layer deposition of alumina on γ-Al_2O_3 nanofibers, *Physica Status Solidi A – Applications and Materials Science* 211 (2014) 403–408.
39. R. Jaaniso, T. Kahro, **J. Kozlova**, J. Aarik, L. Aarik, H. Alles, A. Floren, A. Gerst, A. Kasikov, A. Niilisk, V. Sammelselg, Temperature induced

inversion of oxygen response in CVD graphene on SiO_2, *Sensors and Actuators B-Chemical* 190 (2014) 1006–1013.
40. A. Lust, S. Lakio, J. Vintsevits, **J. Kozlova**, P. Veski, J. Heinämäki, K. Kogermann, Water-mediated solid-state transformation of a polymorphic drug during aqueous-based drug-layer coating of pellets, *International Journal of Pharmaceutics* 456 (2013) 41–48.
41. K. Jukk, N. Alexeyeva, P. Ritslaid, **J. Kozlova**, V. Sammelselg, K. Tammeveski, Sputter-deposited Pt nanoparticle/multi-walled carbon nanotube composite catalyst for oxygen reduction reaction, *Journal of Electroanalytical Chemistry* 708 (2013) 31–38.
42. E. Kibena, M. Mooste, **J. Kozlova**, M. Marandi, V. Sammelselg, K. Tammeveski, Surface and electrochemical characterisation of CVD grown graphene sheets, *Electrochemistry Communications* 35 (2013) 26–29.
43. A. Hallik, A. Alumaa, **J. Kozlova**, J. Tamm, V. Sammelselg, The dopant concentration profiles in PPy/DDS/Cl and PPy/Cl/DDS bilayers, *Synthetic Metals* 181 (2013) 123–128.
44. P. Paris, A. Hakola, K. Bystrov, G. Temmerman, M. Aints, I. Jõgi, M. Kiisk, **J. Kozlova**, M. Laan, J. Likonen, A. Lissovski, Erosion of marker coatings exposed to Pilot-PSI plasma, *Journal of Nuclear Materials* 438 (2013) S754–S757.
45. V. Kiisk, T. Kahro, **J. Kozlova**, L. Matisen, H. Alles, Nanosecond laser treatment of graphene, *Applied Surface Science* 276 (2013) 133–137.
46. A. Tamm, A.L. Peikolainen, **J. Kozlova**, H. Mändar, A. Aidla, R. Rammula, L. Aarik, K. Roosalu, J. Lu, L. Hultman, M. Koel, K. Kukli, J. Aarik, Atomic layer deposition of high-k dielectrics on carbon nanoparticles, *Thin Solid Films* 538 (2013) 16–20.
47. K. Jukk, N. Alexeyeva, A. Sarapuu, P. Ritslaid, **J. Kozlova**, V. Sammelselg, K. Tammeveski, Electroreduction of oxygen on sputter-deposited Pd nanolayers on multi-walled carbon nanotubes, *International Journal of Hydrogen Energy* 38 (2013) 3614–3620.
48. K. Jukk, N. Alexeyeva, P. Ritslaid, **J. Kozlova**, V. Sammelselg, K. Tammeveski, Electrochemical Reduction of Oxygen on Heat-Treated Pd Nanoparticle/Multi-Walled Carbon Nanotube Composites in Alkaline Solution, *Electrocatalysis* 4 (2013) 42–48.
49. H. Erikson, M. Liik, A. Sarapuu, **J. Kozlova**, V. Sammelselg, K. Tammeveski, Oxygen reduction on electrodeposited Pd coatings on glassy carbon, *Electrochimica Acta* 88 (2013) 513–518.
50. L. Tammeveski, H. Erikson, A. Sarapuu, **J. Kozlova**, P. Ritslaid, V. Sammelselg, K. Tammeveski, Electrocatalytic oxygen reduction on silver nanoparticle/multi-walled carbon nanotube modified glassy carbon electrodes in alkaline solution, *Electrochemistry Communications* 20 (2012) 15–18.
51. A. Tamm, M. Dimri, **J. Kozlova**, A. Aidla, T. Tätte, T. Arroval, U. Mäeorg, H. Mändar, R. Stern, K. Kukli, Atomic layer deposition of ferromagnetic iron oxide films on three-dimensional substrates with tin oxide nanoparticles, *Journal of Crystal Growth* 343 (2012) 21–27.

52. I. Kruusenberg, N. Alexeyeva, K. Tammeveski, **J. Kozlova**, L. Matisen, V. Sammelselg, J. Solla-Gullo, J. Feliu, Effect of purification of carbon nanotubes on their 3 electrocatalytic properties for oxygen reduction 4 in acid solution, *Carbon* 11 (2011) 4031–4039.
53. H. Alles, J. Aarik, A. Aidla, A. Fay, **J. Kozlova**, A. Niilisk, M. Pärs, M. Rähn, M. Wiesner, P. Hakonen, V. Sammelselg, Atomic layer deposition of HfO_2 on graphene from $HfCl_4$ and H_2O, *Central European Journal of Physics* 9 (2011) 319–324.
54. A. Tamm, M. Heikkilä, M. Kemell, **J. Kozlova**, K. Kukli, V. Sammelselg, M. Ritala, M. Leskelä, Atomic layer deposition and characterization of zirconium oxide–erbium oxide nanolaminates, *Thin Solid Films* 519 (2010) 666–673.
55. M. Kullapere, **J. Kozlova**, L. Matisen, V. Sammelselg, H.A. Menezes, G.Maia, D.J. Schiffrin, K. Tammeveski, Electrochemical properties of aryl-modified gold electrodes, *Journal of Electroanalytical Chemistry* 641 (2010) 90–98.
56. N. Alexeyeva, **J. Kozlova**, V. Sammelselg, P. Ritslaid, H. Mändar, K. Tammeveski, Electrochemical and surface characterisation of gold nanoparticle decorated multi-walled carbon nanotubes, *Applied Surface Science* 256 (2010) 3040–3046.
57. A. Tamm, M. Kemell, **J. Kozlova**, T. Sajavaara, M. Tallarida, K. Kukli, V. Sammelselg, M. Ritala, M. Leskelä, Atomic layer deposition and characterization of erbium oxide-doped zirconium oxide thin films, *Journal of the Electrochemical Society* 157 (2010) G193–G201.

Konverentsiettekanded:

1. Posterettekanne: J. Kozlova, A. Niilisk, H. Alles, V. Sammelselg. "Inhomogeneity of graphene growth on nickel foils by chemical vapor deposition", FMTDK konverents, 04.03.14, Tartu.
2. Posterettekanne: J. Kozlova, A. Niilisk, A. Kasikov, T. Kahro, H. Alles, V. Sammelselg. "Graphene synthesis on polycrystalline and epitaxial nickel films", FMTDK konverents, 07.05.13, Tallinn.
3. Posterettekanne: J. Kozlova, A. Niilisk, A. Kasikov, A. Gerst, T. Kahro, H. Alles, V. Sammelselg "Quality of graphene prepared by CVD method on nickel", NT13 Fourteenth International Conference on the Science and Application of Nanotubes, 28.06.13, Tallinn.
4. Posterettekanne: J. Kozlova, A. Niilisk, A. Kasikov, A. Gerst, T. Kahro, A.Tõnisoo, H. Alles, V. Sammelselg. "Graphene synthesis on thin nickel films", E-MRS, 30.05.13, Strasbourg, France.
5. Posterettekanne: J. Kozlova, A. Niilisk, A. Kasikov, A. Gerst, T. Kahro, A. Tõnisoo, H. Alles, V. Sammelselg. "Characterization of graphene prepared by chemical vapor deposition on nickel", FM&NT Konverents, 22.04.13, Tartu.

6. Posterettekanne: V. Sammelselg, M. Merisalu, J. Mondal, L. Aarik, A. Tamm, A.-L. Peikolainen, J. Kozlova, M. Marandi, M. Pala, J. Aarik, "Study of atomic layer deposited oxide thin coatings on carbon based materials/metal substrates", 12th International Conference on Atomic Layer Deposition, 17.06.12 – 20.06.12, Dresden
7. Suuline ettekanne: J. Kozlova, T. Kahro, A. Niilisk, H. Alles, V. Sammelselg "Using large-area graphene prepared by chemical vapor deposition for gas sensorics". FMTDK konverents, 29.02.12, Tartu
8. Posterettekanne: J. Kozlova, H. Alles, J. Aarik, A. Niilisk, V. Sammelselg, "Elektronkiirega kiiritatud grafeeni struktuuri uurimine", XXXI Eesti Keemiapäevad, 2011, Tartu.
9. Posterettekanne: J. Kozlova, H. Alles, J. Aarik, A. Niilisk, V. Sammelselg, "Microscopy studies of HfO_2 on graphene", FM&NT Konverents, 16.03.10, Riga, Latvia, 2010.
10. Suuline ettekanne: J. Kozlova, H. Alles, J. Aarik, A. Niilisk, V. Sammelselg "HfO_2/grafeen struktuuride mikroskoopiline uurimine", FMTDK konverents 25.02.10–26.02.10, Tartu
11. Posterettekanne: J. Kapšai, T. Rinken, V. Sammelselg. "Atomic force microscopy study of enzyme glucose oxidase deposited onto solid." XI.Annual Linz Winter Workshop, 6–9.02.2009, Linz, Austria. Johannes Kepler University of Linz.

DISSERTATIONES SCIENTIAE MATERIALIS UNIVERSITATIS TARTUENSIS

1. **Martin Järvekülg.** Tubular microstructures by Hf-, Zr- and Ti-butoxide gel sheet rolling. Tartu, 2011, 112 p.
2. **Sergei Vlassov.** Investigation of nanoscale interactions and mechanical properties of nanostructures using quartz tuning fork based real-time measurements. Tartu, 2011, 171 p.
3. **Margus Kodu.** Pulsed Laser Deposition of Magnesium Oxide and Barium Ternary Oxides for Plasma Display Protective Layers. Tartu, 2011, 89 p.
4. **Rainer Pärna.** Surface studies of some oxide films. Tartu, 2011, 129 p.
5. **Jevgeni Šulga**. Self-assembly and interaction of nanostructures. Tartu, 2011, 114 p.
6. **Wojciech Kuznik.** Quantum-chemical computer simulations of the linear and non-linear optical properties of pyrazoloquinoline and dicyanopyrazine derivatives. Tartu, 2012, 89 p.
7. **Leonid Dorogin.** Structural and tribological properties of zero- and one-dimensional nanocrystals. Tartu, 2012, 193 p.
8. **Viljar Palmre.** Fabrication and characterization of microporous carbon-based electroactive polymer actuators. Tartu, 2012, 99 p.
9. **Madis Paalo**. Synthesis of CNT-metal oxide nanocomposites: sol-gel process, rheology, structural and functional properties. Tartu, 2014, 175 p.
10. **Raul Välbe.** Developement of ionic liquid composites by sol-gel method for elaboration of industrial nano- and microstructures. Tartu, 2014, 97 p.
11. **Urmas Joost.** Impurity and preparation dependent properties of titania thin films. Tartu, 2014, 155 p.
12. **Madis Umalas**. Application of sol-gel technology for production of ceramic nanocomposites and functional coatings. Tartu, 2015, 136 p.
13. **Elena Samsonova.** Energy transfer probe as a tool to study morphological and structural origins of fluorescence quenching in rare-earth doped nanophosphors. Tartu, 2015, 114 p.
14. **Jay Mondal.** Novel Corrosion Protective Nanostructured Composite Coatings. Tartu, 2016, 104 p.
15. **Kathriin Utt.** Metal oxide mesostructures for optical applications. Tartu, 2016, 88 p.
16. **Kaido Siimon.** Electrospun gelatin cross-linked by glucose. Tartu, 2016, 84 p.
17. **Marko Part.** Combined three-dimensional sol-gel structures and atomic layer deposited thin films. Tartu, 2017, 162 p.
18. **Pejman Rasti.** Analysis of Remote Sensing Image Super Resolution using Fluid Lenses. Tartu, 2017, 188 p.
19. **Ivo Romet.** Recombination luminescence of doped borates: origin and application prospects in dosimetry. Tartu, 2017, 111 p.

20. **Vladimir I. Kondratiev.** Processing and characterization of transparent electrode materials. Tartu, 2017, 111 p.
21. **Taivo Jõgiaas**. Mechanical properties of atomic layer deposited thin films and nanocomposites. Tartu, 2017, 125 p.
22. **Lauri Aarik**. Atomic layer deposition and characterization of thin oxide films for application in protective coatings. Tartu, 2017, 180 p.
23. **Triin Kangur.** Preparation and functional properties of stochastic micro-structured sol-gel silica materials. Tartu, 2018, 96 p.
24. **Marta Berholts.** Fragmentation of ionic and hydrogen-bonded molecules induced by synchrotron radiation. Tartu, 2018, 126 p.
25. **Priit Priimägi.** Development and optimization of 3D-microbatteries. Tartu, 2018, 118 p.
26. **Siim Hödemann.** Residual stress determination in chemically strengthened and thermally tempered glass plates using scattered light method. Tartu, 2019, 146 p.